Vibrational spectroscopic analysis of control and altered biological targets from mm to nm length scale

BY

GORKEM BAKIR

A thesis submitted to the Faculty of Graduate Studies of The University of Manitoba in partial fulfillment of the requirements for the degree of

DOCTOR OF PHILOSOPHY

Department of Chemistry
University of Manitoba
Winnipeg, Manitoba, Canada

Abstract

The aim of this thesis was to develop correlative applications using far-field FTIR (FFIR), Attenuated Total Reflectance FTIR, nano-FTIR, and Optical Photothermal IR spectroscopy (O-PTIR) to obtain the spectral signatures of control and altered biological samples and investigate their responses to modifications at different length scales (mm to nm). The spatial resolution of FTIR microscopy is restricted by the diffraction limit, approximately the wavelength of the imaging light. The diffraction limit to spatial resolution can be broken using nano-FTIR at 20 nm spatial resolution, with either a synchrotron light source or broadband nano-FT-IR quantum cascade laser source. O- PTIR also overcomes the IR wavelength-dependent resolution; its spatial resolution is determined by the wavelength of the visible probe laser, typically about ½ μm, and independent of the IR wavelength. In the first part of this thesis, the structure of intact bovine tendons and fibrils were examined, exploiting the effects of polarized IR light with FFIR and near-field IR techniques. FFIR with FPA data yield spectral information only from intact tendons, while O-PTIR data yield information from both tendons and fibrils (~500 nm). Only nano-FTIR delivers spectra from sub-fibrils with diameters ~100 nm. Subsequently, mechanically-damaged fibrils from load-bearing and positional bovine forelimb tendons are studied, revealing positional tendons' higher susceptibility to molecular-level structural changes. In the second part of the thesis, nano-FTIR spectroscopy was used to characterize the fungi cell wall of *Aspergillus nidulans* and *Saccharomyces cerevisiae*. Nano-FTIR emerges as the best non-destructive technique for nanoscale samples, exemplified by the study of cell walls with a thickness of ~100 nm. Each spectrum from different mutants displays characteristic changes, offering insights into gene deletions' impact on biochemical composition. Overall, in this thesis it has been possible to use the

broad applicability of IR spectroscopy for studying different biological targets using standard and novel techniques. The findings have implications for multidisciplinary research, including bioengineering, agriculture, and pharmaceuticals, aiding in the development of new biological materials and antifungal drugs.

.

Acknowledgments

I would like to take this opportunity to express my sincere gratitude to all those who have supported me throughout my journey towards obtaining my PhD degree.

First and foremost, I owe a debt of gratitude to my PhD advisor, Dr. Kathleen M. Gough for her unwavering support, invaluable guidance, and endless encouragement. Her expertise, insights, and constructive feedback have been instrumental in shaping my research, enabling me to achieve my goals and helping me grow as a researcher.

I am also grateful to my committee members, Professors John Sorensen, Jitendra Paliwal, Sabine Mai, whose expert advice, and constructive criticism have greatly enriched my work. Their rigorous questioning and insightful suggestions have helped me to refine my research questions and sharpen my analytical skills.

I would like to acknowledge the contributions of my collaborators in this research journey. I am grateful to Hans Bechtel and Stephanie Gilbert for their assistance with the Nano FTIR instrument in Lawrence Berkeley National Lab. Additionally, thanks to Dr. Tanya Dahms from the University of Regina, Dr. Helen Martin-Yken from Toulouse University, Laurent Kreplak from Dalhousie University, and Sam Veres from St. Mary University for their contributions to my research. I would also like to extend my appreciation to Mustafa Kansiz from Photothermal Spectroscopy Corp. for his support.

I would also like to thank members of the Gough group, especially Zahra Abyat, Godwin Ajaezi, Rinuk Limurn, for their helpful discussions, collaboration, and support.

Special thanks to Horace Luong for providing technical support and use of instrumentation for FTIR-ATR analysis. I am grateful for his expertise, and willingness to help solve any issues that arose during my research. I would like to extend my thanks to the staff of the Department of Chemistry, especially Tannis Wills, Tricia Lewis, for their administrative support and assistance throughout my program. Special thanks go to Chemistry Lab instructor and colleague, Dr. Olesya Fedoryak, for her guidance, support, and encouragement.

My PhD journey has been significantly enhanced by my friends, both inside and outside of academia. I would like to acknowledge the support and love of my best friends, Weslley Silva, Jorge Dourado, Tamanna Poonia, Ewan McRae, Simarpreet Singh. Their friendship and positive attitude have been invaluable in keeping me motivated and focused throughout the challenges of the PhD program.

I also want to express my gratitude to my host family and parents in Winnipeg, Kimberley Unrau and Ben Unrau, for their hospitality, kindness, and support throughout my PhD program. Their generosity and warmth have made me feel at home away from home.

I would also like to express my heartfelt gratitude to my special friends and neighbors, Ann, Margie, Martha, Erna, Kay, Judy, Fran, Doris, Helen and Agnes. Their encouragement, kind words, and presence provided me with the strength and motivation to overcome challenges and reach this milestone. I will always remember our bingo and games nights.

I would like to extend my sincere thanks to the University of Manitoba Enhancement of the Tri-council (GETS) for providing me with the financial support that allowed me to pursue my PhD degree. I would also like to express my gratitude to the Chemistry Department at the University of Manitoba for selecting me for several Graduate Awards throughout my program.

Last but not least, I would like to express my deep appreciation to my parents, Müge and Ismet, brother, Mert, and grandparents, Emine and Orhan, for their unwavering support, encouragement, and love. Their support has been indispensable in helping me to pursue my dreams. Without their guidance, sacrifices, pursuing a PhD would have been an insurmountable challenge. Their unwavering belief in me has been a tremendous source of strength. I cannot express enough how much I owe to them.

Thank you all for your support, guidance, and encouragement. I am forever grateful for your contributions to my academic success.

Table of Contents

List of Tables

List of Figures

List of Supplemental Figures

List of Abbreviations

AFM	Atomic Force Microscopy
ALS	Advanced Light Source
ATR	Attenuated Total Reflection
BL	Beamline
BS	Beamsplitter
CDE	Common Digital Extensor
CON	Control
CWI	Cell Wall Integrity
DNA	Deoxyribonucleic Acid
ELISA	Enzyme-Linked Immunoassay
FF	Far-Field
FOV	Field of View
FPA	Focal Plane Array
FS	Force Spectroscopy
FSD	Fourier Self-Deconvolution
FT	Fourier-Transform
FTIR	Fourier-Transform Infrared
FWHM	Full Width at Half Maximum
HIV	Human Immunodeficiency Virus
IR	Infrared

IRE	Internal Reflection Element
IRENI	Infrared Environmental Imaging Beamline
LBNL	Lawrence Berkeley National Laboratory
MCT	Mercury Cadmium Telluride
MIR	Mid-Infrared
NA	Numerical Aperture
NFIR	Near-Field Infrared
NMR	Nuclear Magnetic Resonance
NP	Nanoparticle
O-PTIR	Optical Photothermal Infrared
OCT	Optimal Cutting Temperature
OPO	Optical Parametric Oscillator
PBS	Phosphate Buffer Solution
PDA	Potato Dextrose Agar
PDMS	Polydimethylsiloxane
PET	Polyethylene Terephthalate
PSF	Point Spread Function
QCL	Quantum Cascade Laser
RMieS	Resonant Mie Scattering
RNA	Ribonucleic Acid
SDF	Superficial Digital Flexor
SEM	Scanning Electron Microscopy
SERS	Surface Enhanced Raman Scattering

SINS	Synchrotron Infrared Nanospectroscopy
sSNOM	scattering-type Scanning Near-Field Optical Microscopy
s-SNOM	scattering-type Scanning Near-Field Optical Microscopy
SNR	Signal To Noise Ratio
TEM	Transmission Electron Microscopy
YKO	Yeast Knock Out
YPD	Yeast Extract Peptone Dextrose
μXRF	X-Ray Microfluorescence
2ndD	Second Derivatization

Chapter 1. Introduction

Vibrational spectroscopy with Infrared (IR) is a technique that provides information on the vibrational modes of a molecule after the absorption of IR light. The frequency of these modes is characteristic of the specific functional groups, the combination of atomic motions called normal modes. Each molecule is considered a unique collection and arrangement of functional groups resulting in a unique spectrum or fingerprint.

Over the past few decades, vibrational spectroscopic techniques have been advanced by coupling an IR interferometer with IR microscope optics, permitting spectrochemical imaging that gives detailed information about the biomolecular composition of a sample. This combination optimizes the data collection time and processing, making them reliable tools for biomedical and biological applications. Optical microscopy can offer structural detail, while multi-point spectral measurement provides chemical information from the entire field of view of the optical picture. The primary purpose of acquiring spatially resolved spectroscopic data is to pinpoint each voxel within a sample so that spectra can be captured and evaluated, and information can be derived from the targeted region (Baker et al., 2014; Bhargava, 2012).

The spatial resolution of Fourier Transform Infrared (FTIR) microscopy is restricted by the diffraction limit, which is on the order of the wavelength of the imaging light. On the Agilent Cary 620 microscope in our lab, the greatest pixel resolution for far-field (FF) FTIR microscopy is 1.1μm in transmission with a 15× objective. FF-FTIR and FF-FTIR-ATR can be employed for complementary spectral data at nominal pixel sizes ranging from 1 to 5 μm. The IR wavelength-dependent resolution is also broken by optical photothermal IR (O-PTIR), a novel FF approach. The visible wavelength of a probe laser, on the submicron scale and independent of the IR light wavelength, determines the spatial resolution (Baden et al., 2020; Bakir et al., 2020). The spatial

resolution diffraction limit can be further overcome by utilizing nano FTIR at 20 nm spatial resolution with either a synchrotron light source or a broadband nano-FTIR quantum cascade laser (QCL) source (Wiens et al., 2016).

The aim of thesis is to investigate the responses of diverse biological samples to different alterations by learning how to interpret the spectral signatures at nm length scales and translate them into information about biochemical composition. This goal motivates the development of new ways to employ novel vibrational spectroscopy techniques. Multiple vibrational spectroscopic approaches must be used to develop biospectroscopic imaging procedures that may be applied to real-world issues. Such real-world issues include the diagnosis of various diseases, from cancer to Alzheimer's, the characterization of pathogenic microorganisms, and the development of bioengineered materials through investigating tissue and the cell composition and structure. Different IR spectroscopy techniques, such as nano-FTIR and Far-field IR that work at different length scales, can benefit the analysis of different biological targets. Far-field- FTIR is useful for oriented larger-scale imaging (Wiens et al., 2016). O-PTIR can be used to image fibrils (Bakir et al., 2020), whereas nano-FTIR is essential to look at cell walls of yeast strains. The targets in this thesis have been studied to get information about their biochemical composition and molecular conformation simultaneously with techniques from mm to nm length scales. Each target presents distinct challenges that must be addressed by the use of multiple spectroscopic tasks, as well as the development of appropriate methods on sample preparation for each type of spectroscopy. The importance of this thesis lies not only in providing direct chemical information from the targets using non-destructive vibrational spectroscopic techniques but also in serving as a solid foundation for future studies in this field, regardless of the target under investigation.

1.1 Problem statement

Fungi: This research focuses on detecting changes in cell wall components that may affect the cell wall integrity (CWI) by utilizing nano-FT-IR spectroscopy to acquire spectrochemical data on wild-type and knock-out strains of *Aspergillus nidulans* and *Saccharomyces cerevisiae* at 25 nm pixel resolution. Spectroscopic characterization of the cell walls is challenging for all approaches due to their small diameters (1-4 μm) and cell wall thicknesses (50-200 nm), which make it difficult to characterize and distinguish the cell wall components from the whole cell. This is the first study to combine far field-FTIR and nano FTIR approaches to better understand the impact of gene deletion on the cell wall structure. Notably, our approach leverages existing gene deletion strains to provide direct chemical information, making it the first of its kind in the field.

Collagen: It is critical to understand the relationship between mechanical characteristics and structure of tendon at a molecular level to comprehend remodelling activities in damaged tendons and to promote recovery. In this part of the thesis, both conventional and novel vibrational spectroscopic techniques are used to investigate the structure of collagen tendons and fibrils, under mechanical stress. The tendons are obtained from different sources including bovine tail tendon and bovine forelimb: (1) the superficial digital flexor (SDF), which is an energy-storing tendon and (2) the common digital extensor (CDE), which is a positional tendon. The far-field methods used on intact tendons are FF-FTIR, ATR and O-PTIR. Nano-FTIR and O-PTIR are used on fibrils from 50 to 500 nm. Polarized infrared light is also exploited to learn more about collagen organization in control and mechanically damaged tendons and fibrils at all scales.

1.2 Objectives

Different IR spectroscopy techniques function best at different length scales, permitting different insights and perspectives for varied biological targets and questions. The research in this thesis is focused on fungi and collagen tendons/fibrils, with the goal of obtaining their spectral signatures, interpreting them in terms of chemical composition and orientation, and examining their responses to various alterations at different length scales (from mm to nm). In order to gain insight into fundamental questions in these selected biological targets, it is necessary to use numerous vibrational spectroscopy methods. Thus, new correlative applications are developed with far-field IR (FFIR), Attenuated Total Reflectance IR (ATR-IR), O-PTIR and nano FT-IR. Working with novel methods such as nano FTIR and O-PTIR provides unique spectral data on previously unstudied systems using wavelength-independent nanoscale vibrational spectroscopic methods. The use of IR spectroscopy at the nano-scale level is expected to allow us to compare, contrast and characterize differences between control and altered samples. This new information on their compositional and their structural changes will contribute to a deeper understanding of their behaviors under specific conditions. Each target studied in this thesis is accompanied by specific objectives and hypotheses as described below:

Chapter 3*:* Image and examine the ordered collagen from bovine tail tendon with polarized FF-FTIR with FPA detector and FF optical photothermal IR (O-PTIR), and with nano-FTIR spectroscopy based on scattering-type scanning near-field optical microscopy (s-SNOM).

It is known that due to the hierarchical structure and radial symmetry of collagen, the changes in the relative intensity of the Amide I, II and III vibrational bands appear in their spectral profiles under polarized IR light and can be observed at the sub-micron scale.

Hypothesis 3-1: The integration of polarized FF-FTIR with FPA, O-PTIR, and nano-FTIR spectroscopy can provide detailed and correlated information enabling the characterization and examination of ordered collagen tendons at different length scales.

Hypothesis 3-2: Spectra from fibrils will show consistent outcomes regardless of their depth—whether they are 50 nm 500 nm or in diameter—due to the uniform nature of ordered fibril structures, aligning with the potential of O-PTIR and nano-FTIR spectra to offer dependable characterizations of typical collagen type I fibrils, spanning diameters of 450 nm to 35 nm, respectively.

Hypothesis 3-3: O-PTIR spectra obtained with laser light oriented perpendicular to the fibril direction will exhibit profiles similar to those obtained through nano-FTIR and through perpendicular FF-FTIR with FPA. O-PTIR spectra that are obtained with laser light parallel to the fibril direction will be similar to those from parallel FF-FTIR with FPA results. It is to important to highlight that both perpendicular and parallel O-PTIR results hold the potential to provide previously undiscovered information.

Chapter 4: Image and examine the damaged collagen from bovine forelimb (SDF &CDE) tendon with FTIR with FPA detector and FF optical photothermal IR (O-PTIR), and with nano-FTIR spectroscopy based on scattering-type scanning near-field optical microscopy (s-SNOM).

It is known that mechanical damage produces disorder, as can be seen with SEM and AFM that give topological information not molecular information. However, nano-FTIR spectroscopy can show direct chemical compositional and structural information, allowing us to investigate the known differences in fibrils between positional and energy-storing tendons. Specifically, we anticipate that nano-FTIR spectroscopy will reveal the heterogeneous nature of positional tendons, facilitating their structural adaptability for remodeling and repair, while highlighting the organized structure of energy-storing tendons, which enables them to bear higher stress levels.

Hypothesis 4-1: At the molecular level, differences between positioning and energy-storing tendons are expected to show only when the tendon is nearly damaged. Collagen fibrils in functionally unique tendons are susceptible to injury under tensile overload and cyclic fatigue loading in different ways.

Nano-FTIR provides spectra that are perpendicular to the fibril direction and these spectra illustrate changes in the position of band maxima, relative intensities and band shapes when the molecular structure is distorted.

> *Hypothesis 4-2:* When the fibril is mechanically damaged, the relative intensity of backbone mode bands such as Amide II and CH_2 deformation of the proline ring may increase compared to the Amide I band due to disorganized-helical structures.

Chapter 5: Image and examine *Aspergillus nidulans* cell wall with AFM and near-field IR spectroscopy and show correlated data using these two methods for multiplexed *in situ* research of fungal cell wall nanoscale architecture and chemical composition.

It is known that the *ugmAΔ* and *ugtAΔ,* gene deletion strains, which lack the mutase catalyst and transporter enzymes, respectively, demonstrate the involvement of Gal*f* in CWI and cause alterations in the fungal cell wall.

> *Hypothesis 5-1*: These alterations in the cell wall structure can be detected from nano-FTIR spectra of *ugmAΔ,* and *ugtAΔ* gene deleted strains compared to wild-type.

> *Hypothesis 5-2:* The nano-FTIR spectra can offer clear evidence that gene deletions, which limit the contribution of *Galf* to the cell wall structure, will lead to a response that primarily enhances the content of α-glucan.

> *Hyphothesis 5-3:* The spectra from both gene deletion strains may exhibit alterations in the carbohydrate region, compared to the wild-type, that can be attributed to various factors including the presence of carboxymethyl groups within the glucans.

Chapter 6: Image *Saccharomyces cerevisiae* yeast cells with FF-FTIR with FPA, FF-FTIR- ATR and nano-FTIR spectroscopy based on scattering-type scanning near-field optical microscopy (s-SNOM) and examine the alterations in carbohydrates (e.g., chitin, glucans) and protein structures in the cell wall.

Hypothesis 6-1: The nano-FTIR spectra can provide evidence that the absence of Kre6 causes reduce or eliminate β-1,6-glucan components in the cell wall of kre6Δ.

Hypothesis 6-2: The nano-FTIR spectra can provide evidence that the absence of Knr4 reduces glucan content while increasing chitin content in the cell wall.

Hypothesis 6-3: These changes in the chemical composition will be detectable directly from the NFIR spectra of the cell wall of these YKO strains of *S. cerevisiae* compared to wild-type.

1.3 Thesis layout

This thesis is presented in a sandwich style and is comprised of 7 chapters. The first chapter provides a brief introductory overview of the significance of the study, a statement of the problem, a list of objectives and accompanying hypotheses, and the thesis layout. Chapter 2 provides the theory of IR spectroscopy, the techniques used in the thesis, as well as the background of the studies. Chapters 3 to 6 are peer-reviewed journal publications already in print-or to be submitted. Chapter 3 and Chapter 4 present the studies on collagen tendons from the bovine tail and forelimb. Chapter 3 is a published peer-reviewed paper in *Molecules*: Bakir, G., Girouard, B. E., Wiens, R., Mastel, S., Dillon, E., Kansiz, M., & Gough, K. M. (2020) Orientation Matters: Polarization Dependent IR Spectroscopy of Collagen from Intact Tendon Down to the Single Fibril Level. *Molecules*, *25*(18), 4295. It shows the polarization effect on intact tendons and fibrils working with far-field and near-field IR techniques. Chapter 4 follows the bovine tail tendon study described in Chapter 3. In this chapter, we showed the alterations in fibril structure at the molecular level when they undergo mechanical stress by using nano-FTIR spectroscopy. Far-field techniques: FF-FTIR with FPA and O-PTIR are also used for complementary results.

Chapter 5 and Chapter 6 are the studies on the fungi cell wall. Chapter 6 is a peer-reviewed published paper in *Analyst*: Bakir, G., Girouard, B. E., Johns, R. W., Findlay, C. R.-J., Bechtel, H. A., Eisele, M., Kaminskyj, S. G. W., Dahms, T. E. S., & Gough, K. M. (2019) Ultrastructural and SINS analysis of the cell wall integrity response of Aspergillus nidulans to the absence of

galactofuranose. This study uses Nano-FTIR for the first time on a fungal cell wall. In Chapter 6, we presented the work on yeast cell walls with FF-FTIR, FF-FTIR+ATR and nano-FTIR spectroscopy. Despite the size and shape of the yeast cells, we showed the alterations in their cell wall with the nanoscale technique. It is submitted to a journal Applied spectroscopy (January 2023): Gorkem Bakir, Tanya E. S. Dahms, Helene Martin-Yken, Hans A. Bechtel, Kathleen M. Gough. *Saccharomyces cerevisiae* cell wall remodeling in the absence of Knr4 and Kre6 was revealed by nano-FTIR spectroscopy. The revised version is about to be submitted to Applied Spectroscopy.

In Chapter 7, I summarize the key conclusions of the thesis and the significance of the results. This chapter also provides recommendations for the future regarding how these techniques could be improved or expanded, not only specifically for the targets used in the thesis but also for other biological samples.

1.4 References

Baden, N., Kobayashi, H., & Urayama, N. (2020). Submicron-resolution polymer orientation mapping by optical photothermal infrared spectroscopy. *International Journal of Polymer Analysis and Characterization*, *25*(1), 1–7. https://doi.org/10.1080/1023666X.2020.1735851

Baker, M. J., Trevisan, J., Bassan, P., Bhargava, R., Butler, H. J., Dorling, K. M., Fielden, P. R., Fogarty, S. W., Fullwood, N. J., Heys, K. A., Hughes, C., Lasch, P., Martin-Hirsch, P. L., Obinaju, B., Sockalingum, G. D., Sulé-Suso, J., Strong, R. J., Walsh, M. J., Wood, B. R., … Martin, F. L. (2014). Using Fourier transform IR spectroscopy to analyze biological materials. *Nature Protocols*, *9*(8), 1771–1791. https://doi.org/10.1038/nprot.2014.110

Bakir, G., Girouard, B. E., Wiens, R., Mastel, S., Dillon, E., Kansiz, M., & Gough, K. M. (2020). Orientation Matters: Polarization Dependent IR Spectroscopy of Collagen from Intact Tendon Down to the Single Fibril Level. *Molecules*, *25*(18), 4295. https://doi.org/10.3390/molecules25184295

Bhargava, R. (2012). Infrared Spectroscopic Imaging: The Next Generation. *Applied Spectroscopy*, *66*(10), 1091–1120. https://doi.org/10.1366/12-06801

Wiens, R., Findlay, C. R., Baldwin, S. G., Kreplak, L., Lee, J. M., Veres, S. P., & Gough, K. M. (2016). High spatial resolution (1.1 μm and 20 nm) FTIR polarization contrast imaging reveals pre-rupture disorder in damaged tendon. *Faraday Discussions*, *187*, 555–573. https://doi.org/10.1039/c5fd00168d

Chapter 2. Infrared spectroscopy

Spectroscopy is concerned with the absorption, emission or scattering of electromagnetic radiation by atoms or molecules and measurement of intensity as a function of wavelength (Hollas, 2005). Specifically, in vibrational spectroscopy, light is used to obtain information about vibrations in molecules for direct detection of their specific functional groups, conformational behaviours and secondary structures. The frequencies of the vibrational modes are characteristic of specific functional groups, so individual molecules have their individual spectral fingerprints. Infrared absorbance spectroscopy is one of the subtypes of vibrational spectroscopy techniques that allows non-destructive measurements of the chemical composition of organic, inorganic and biological samples. The outcome of a vibrational spectroscopic measurement is the infrared (IR) spectrum, a graph in which the wavenumber ($1/\lambda$) is plotted against the amount of light absorbed (Griffiths & de Haseth, 2006).

2.1 Infrared light

The IR spectral range is subdivided into three regions: near-IR, mid-IR, and far-IR, with wavelengths of 0.78 - 2.5 μm, 2.5-25 μm and 50-1000 μm, respectively (Chalmers, and Griffiths, 2002; Herzberg, 1945; Skoog et al., 2007). Infrared spectroscopy usually uses the mid-IR region

of the electromagnetic spectrum from 25 µm to 2.5 µm or 4000 to 400 cm^{-1} (**Figure 2.1**).

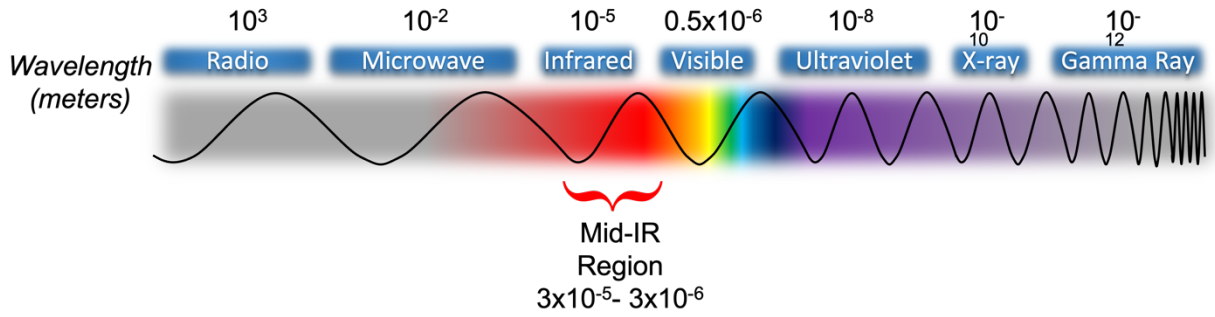

Figure 2.1. Electromagnetic Spectrum (G.Bakir)

The energy of a single photon of light, E, directly depends on the frequency and is defined by:

$$\mathrm{E} = hf = \frac{hc}{\lambda} = hc\bar{\nu} \qquad 2.1$$

where h is Planck's constant ($6.63 \times 10^{-34}\ \mathrm{J \cdot s}$), f is frequency, c is the speed of the light ($3.00 \times 10^{8} \mathrm{ms}^{-1}$), λ is wavelength, and $\bar{\nu}$ is wavenumber (Skoog et al., 2014).

2.1.1 Vibrational energy levels

Infrared spectroscopy measures the electric dipole-mediated transitions between vibrational energy levels. The IR process involves the absorption of energy by the molecule; if the vibrational energy matches the photon energy and the vibration causes a change in the molecular dipole moment, a change in the vibrational energy level can occur. Except for the homonuclear species (such as O_2, N_2, Cl_2), which do not have net changes in dipole moment for their only vibrational mode, all molecular species can absorb IR radiation and produce an infrared spectrum. From the spectrum, detailed information about the molecule's structure can be obtained.

The motion of a simple diatomic molecule can be modeled by considering that the two atoms with two different masses (m_1 and m_2) are connected by a massless spring-like bond (**Figure 2.2**).

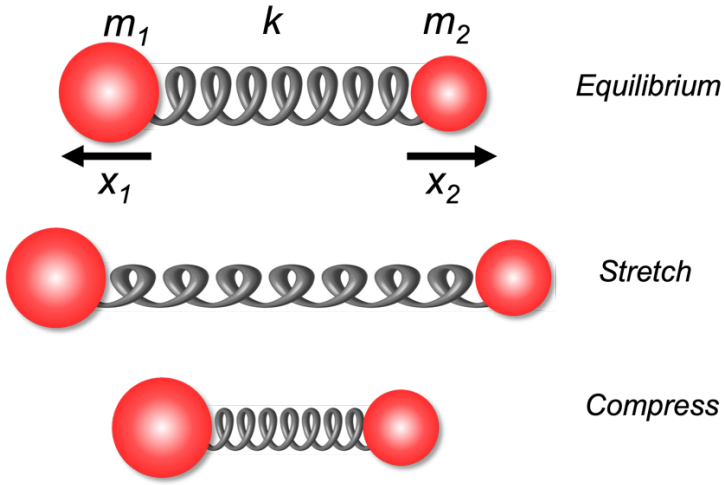

Figure 2.2. Motion of diatomic molecule. *k* is the spring constant, m_1 and m_2 are masses, x_1 and x_2 are the displacement vectors. (G. Bakir)

During the vibration, as the distance between the atoms changes the potential energy of the molecule changes (Figure 2.2). The classical vibrational frequency for a diatomic molecule is given by:

$$\nu = \frac{1}{2\pi}\sqrt{k/\mu} \qquad 2.2$$

where k is the force constant (a measure of the strength of the bond), μ is the reduced mass, described by Equation 2.3:

$$\frac{1}{\mu} = \frac{1}{m_1} + \frac{1}{m_2} \qquad 2.3$$

The diatomic potential energy of a harmonic oscillator can be plotted as a function of the distance between the atoms (**Figure 2.3**). In the case of the harmonic approximation, the energy of the vibrational levels is equally spaced, E_v, is given by:

$$E_v = \left(v + \frac{1}{2}\right) h\nu \qquad 2.4$$

where v is the vibrational quantum number (v = 1, 2, 3…), h is the Planck's constant, and ν is frequency. As the separation between the vibrational energy levels is constant in the harmonic approximation, this approximation is more suitable to describe the energy levels of molecules in the ground vibrational state (the lowest energy level). In the anharmonic oscillator model (Morse-type potential), the separation between the vibrational energy levels of a molecule becomes smaller as the quantum number increases until the dissociation limit is reached at the virtual energy levels (**Figure 2.3**). The Morse potential is considered a more realistic approach; energies of allowed vibrational states, defined by quantum number, v, are given by the expression:

$$E_v = \left(v + \frac{1}{2}\right) h\nu + \left(v + \frac{1}{2}\right)^2 h\nu x \qquad 2.5$$

where x is the dimensionless anharmonicity constant. The harmonic model does not allow the occurrence of any transitions involving changes in quantum number by more than ± 1 ($\Delta v = \pm 1$). On the other hand, the effect of anharmonicity is to relax this selection rule (i.e., to allow bands caused by $|\Delta v| > 1$ to become allowed). Thus, the anharmonic oscillator model often includes overtones ($\Delta v = \pm 2, \pm 3\ldots$) and combinations of other bands (Griffiths & de Haseth, 2006; Larkin, 2011).

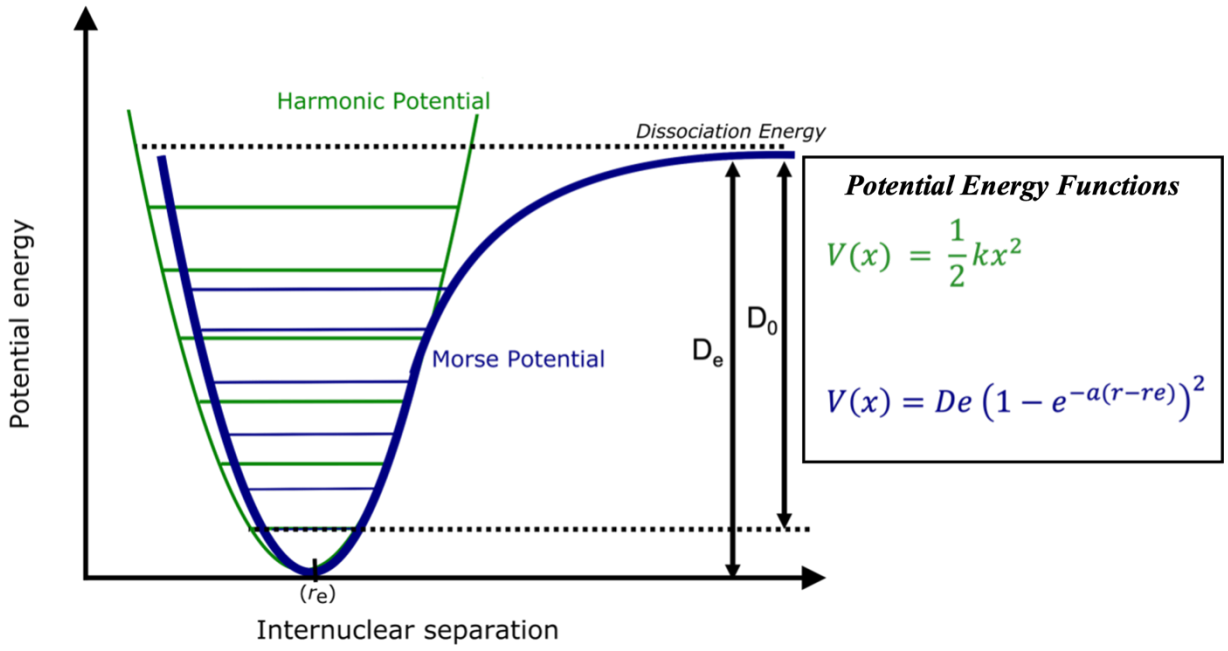

Figure 2.3. Potential energy curves of harmonic (green) and anharmonic (Morse, blue) oscillator with energy functions (Green: Harmonic potential energy function, Blue: Morse potential energy function). D_0 is dissociation energy, and D_e is the theoretical energy necessary to break the bond. X= r-re (displacement) k: force constant (G. Bakir)

2.1.2 Vibrational modes

The number of fundamental absorption modes depends on the molecule's internal degrees of freedom and molecular geometry. Each of the atoms in a molecule has three degrees of freedom as they can move along the three different axes (*x, y* and *z*) in three-dimensional (3D) space, resulting in 3*N* degrees of motional freedom. Three of these degrees represent the translation of the molecule along the *x, y* and *z* directions, while another three describe the rotations of the molecule about each of these axes. For a non-linear molecule, there are 3*N*-6 normal modes of vibration, where *N* is the number of atoms in the molecule. The remaining 3*N*-6 degrees of freedom represents atomic displacements, angles or distances between the atoms that can be changed with

this motion. A linear molecule has 3*N*-5 normal modes as they do not have the degree of freedom (no moment of inertia) along the internuclear axis resulting in the loss of one degree of rotational freedom. Many normal vibrational modes involve the stretching and bending motions of atoms. In a stretching mode involving a molecule with symmetry, a change in the bond lengths between the three atoms can be symmetric or antisymmetric. In the bending mode, the bond length does not change while the angle between the two bonds moves regularly. The terms rock, twist, scissors, wag, torsion, ring breathing, and inversion (or umbrella) are also widely used in addition to the descriptions of group vibrations as stretch and bend. Some of these vibrational modes are illustrated by using the simple organic molecule formaldehyde ($O{=}CH_2$) (**Figure 2.4**) (Griffiths & de Haseth, 2006; Hollas, 2005; Larkin, 2011). The most important vibrational modes for biological samples are discussed in *Section 2.7 IR spectra for biological samples*.

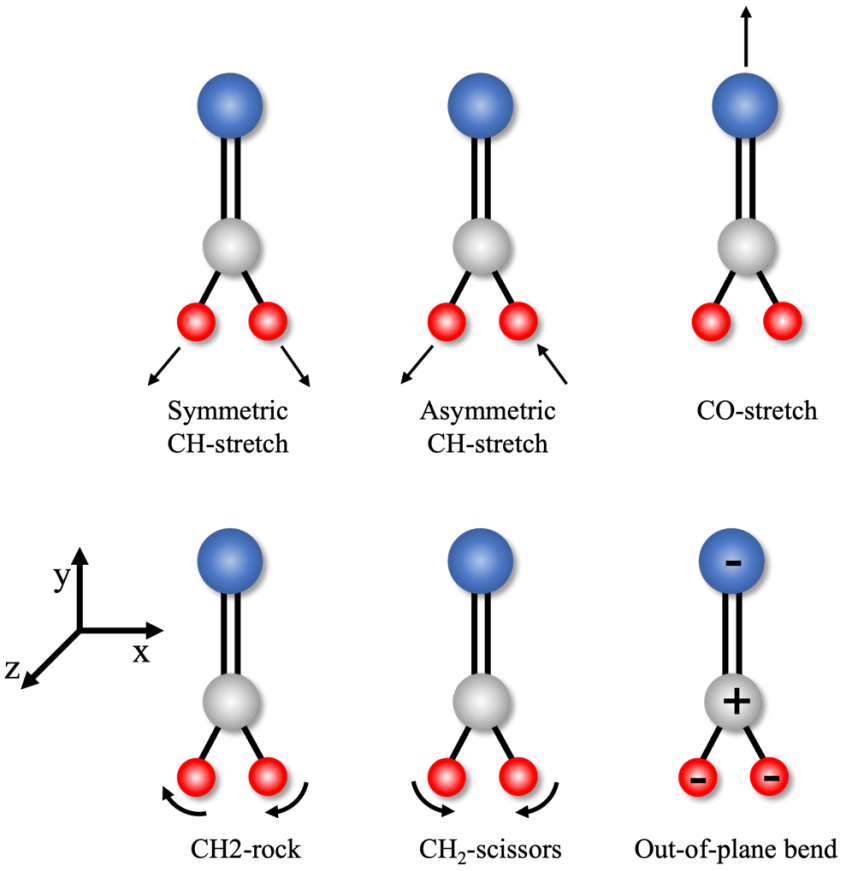

Figure 2.4. Representation of the vibrational modes in the simple organic molecule formaldehyde.

2.2 Dispersive vs FTIR spectrometers

As the name suggests, dispersive spectrometers create spectra by dispersing the incoming infrared light into its various wavelengths or frequencies. Prisms or holographic gratings are the most common dispersive elements. The grating separates the wavelengths to be detected, and a narrow band of wavelengths is allowed through a slit to reach the detector, which records the number of photons in that energy range from the sample and from the reference. The range sampled is adjusted by rotating the dispersive element sequentially; dispersive systems are significantly limited by slow scanning speed and low throughput.

Since the 1980s, Fourier transform spectrometers (FT) have replaced them for mid and far-IR measurements because of the many advantages: they are fast, reliable, and convenient. While other types of optical systems are encountered, FTIR instruments are interferometric systems. Scanning speed can be improved as the interferometer can measure all frequencies simultaneously. FTIR spectrometers provide high signal-to-noise ratio (SNR) and accurate spectral readings (Griffiths & de Haseth, 2006). These advantages are discussed in detail in section *2.4 Advantages of FTIR spectroscopy*.

2.3 Michelson interferometer

The FTIR spectrometer is based on the two-beam interferometer, named after Michelson, who designed the device in 1891. The fundamental hypothesis behind all sorts of interferometers can be understood by knowing the working principles of the Michelson interferometers (**Figure 2.5**).

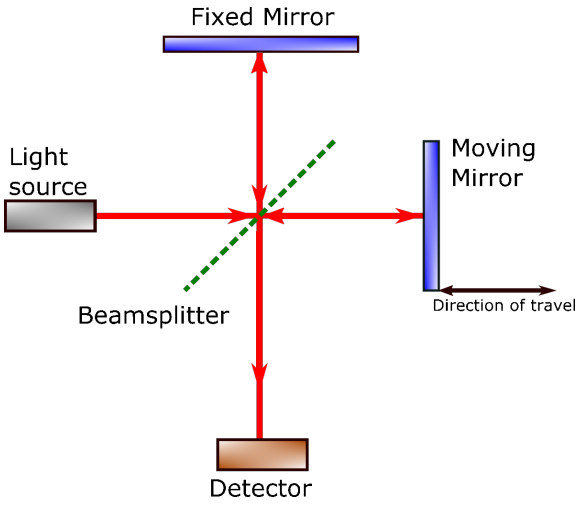

Figure 2.5. Michelson interferometer. (G. Bakir)

In the Michelson interferometer, a beam splitter (an infrared transparent crystal oriented at a 45° angle to the incoming light source) splits the incident beam into two beams at right angles to

one another. The ideal beamsplitter is made of non-absorbing material that reflects and transmits equally (50%). Half of the incident radiation is reflected to a fixed plane mirror while the other half is transmitted to another plane mirror whose distance to the beam splitter varies continuously over a user-selected range. The two beams are reflected back from these mirrors to the beam splitter, recombining and interfering constructively or destructively for each wavelength. The moving mirror produces a varying optical path difference, called retardation, between the two arms of the interferometer. Depending on the length of the path difference, a phase difference between the beams occurs, creating an interferogram at the detector (Skoog et al., 2014). The interferogram is a single cosine wave if a monochromatic light is used as the source, or the sum of many cosine waves of different wavelengths if the IR light source is broadband (**Figure 2.6**). As soon as the detector captures the interferogram, it is transferred to the computer, where a Fourier transform (FT) algorithm is applied, and the interferogram signal is converted to a spectrum (absorbance or transmittance) in units of energy.

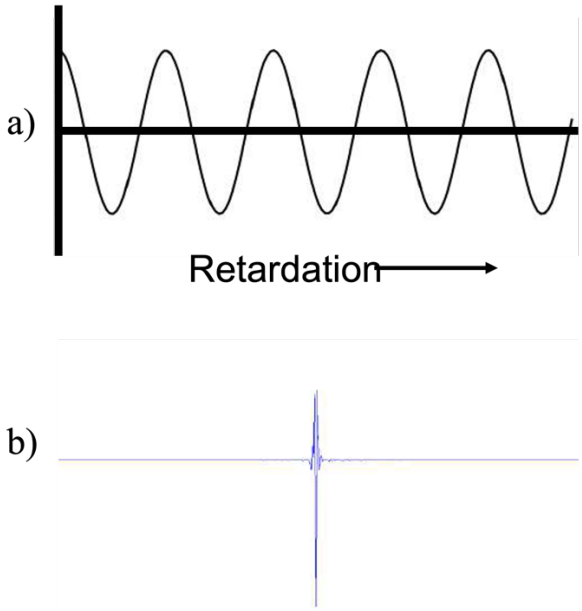

Figure 2.6. a) Plot of a single frequency interferogram cosine wave signal recorded by the detector as a function of retardation, b) Multiple frequency interferogram created by a FTIR spectrometer in a broadband range of wavenumbers (4000 - 400 cm^{-1})

2.4 Advantages of FTIR spectroscopy

FTIR spectrometers offer numerous advantages over dispersive spectrometers. Multiplex (Fellgett) and throughput (Jacquinot) are the two most important advantages. The Michelson interferometer provides a multiplex (Fellgett) advantage by utilizing broadband sources where an interferogram records the superimposed intensities from all wavelengths presented to the detector. The separate signals at each wavelength are then recovered from the combined interferogram by Fourier-transform mathematical analysis (Chalmers, Griffiths, 2002). Because of the multiplex advantage, an FTIR can complete and average several scans in less time than dispersive instruments. Another advantage of interferometers over dispersion spectrometers, emphasized by Jacquinot, is that more radiation can be passed between the source and the detector for each

resolution element. Unlike a dispersive spectrometer with a slit, FTIR instruments have no limitation that prevents the IR light from reaching the detector; however, a circular aperture or Jacquinot stop controls the amount of IR light reaching the detector. This circular aperture allows more light than a slit for the chosen resolution and wavelength. A brighter source leads to a higher signal-to-noise ratio (SNR) achieved in a much shorter time than with dispersion or with a lower-intensity source. As a result, with the higher signal-to-noise, the sensitivity of the instrument will be better, and details in a sample spectrum will be more explicit and more distinguishable even for the small absorptions (Griffiths & De Haseth, 2006).

2.5 Globar vs Synchrotron light sources

Most of the FTIR spectrometers are employed with an incandescent silicon carbide source, (aka Globar) which is capable of working at 1400 K for several years with no degradation. The Globar emits light that is comparable to blackbody radiation; thus, the emission parameters of the polychromatic light in the mid-IR region are typically similar to that of a blackbody. Therefore, the Globar light source is suitable for IR absorption spectroscopy as the spectral energy density can possibly be increased proportionally to the temperature increment. However, the rise in the temperature of a Globar may cause a degradation of electric contacts at the silicon carbide rod resulting in cracking (Chalmers & Griffiths, 2002; Salzer & Siesler, 2009).

The inexpensive Globar source has much lower brilliance compared to a synchrotron light source. The cyclic particle accelerator facilities generate synchrotron radiation. The particles, electrons, are accelerated almost at the speed of light along the cyclic path by using an electric field and bending magnets. When the bending magnets change the path of the electrons, their acceleration is changed due to these external fields, and energy is released as photons. These

photons are a broadband source suitable for different experiments across energy ranges from x-ray and UV to longer wavelengths in the electromagnetic spectrum, and are ideal for IR analysis (Yarris, 1993). Besides providing an extremely broad spectral range, synchrotron radiation is spatially coherent and has a large photon flux yield. Thus, it is two to three orders of magnitude higher brightness than a typical, incoherent Globar light source (Bechtel et al., 2020). As the width of the light beam is narrower in the synchrotron compared to the Globar source, light can be focused easily and be concentrated in a tiny area yielding extreme brightness at about 1000 times brighter than the Globar source. This advantage allows collection of individual spectra in seconds at diffraction limited spatial resolution, whereas the same acquisition would take several minutes with a Globar light source (Griffiths & de Haseth, 2006).

2.6 FTIR spectrochemical imaging

2.6.1 Far-field FTIR spectroscopy

A far-field FTIR microscope consists of a conventional FTIR spectrometer combined with a microscope optical system that is designed with IR reflective optics **Figure 2.7**. These reflective optics are Schwarzschild/ Cassegrain design condensing objectives, which focus the incoming IR light from the interferometer onto the sample. Based on the chosen method, either transmission or reflectance, the light focused on the sample is then carried to the detector. In transmission mode, the IR light is focused on the detector as soon as it passes directly through the sample, while in reflectance mode, light is reflected upward off the surface of a sample after passing through it. Most IR microscopes have the capability of using either a single-element detector for sequential collection of single pixels (mapping) or multi-element detectors (IR-Focal Plane Array (FPA)) that allow simultaneous collection of multiple spectra (imaging). In single-pixel mapping mode, the

translation stage raster scans the sample through the IR beam; the pixel size is chosen by adjusting the sliding glass apertures. The sample has to be moved in a grid pattern to obtain a two-dimensional image with a spectrum at each pixel. This mapping approach is time-consuming, and the FPA detector, a more efficient method, became more popular.

FPA detectors are available in an n × n format where n = 16, 32, 64, 128 or 256. The field of view (FOV) is imaged onto the detector, and an array of spectra are acquired simultaneously, which allows for recording more than 65,000 location-specific IR spectra for a 256 × 256 FPA in only a few minutes, with a thermal IR source. The instrument at the University of Manitoba has a 64 × 64 FPA that provides 4096 pixels, with a nominal spatial resolution of ~5.5 μm per pixel. This can be improved to ~1.1 μm with a higher magnification optic in front of the FPA. Although IR light source is a broadband thermal light source in typical commercial systems, it can also be incoherent or coherent Synchrotron Radiation or a broadband pulsed laser, which provides much higher spectral brightness and better SNRs in a shorter time. The first synchrotron IR microscope with FPA (128x128 pixel) was the infrared environmental imaging (IRENI) system at the Synchrotron Radiation Center in Madison, WI (Nasse et al., 2011), however, the Radiation Center was closed in 2014.

The spatial resolution of the microscope is determined by the wavelength of the radiation, λ and the numerical aperture (NA) of the Cassegrain optics. The NA is defined by the equation:

$$NA = (n) \sin \theta \qquad 2.6$$

where θ is the maximum angle of acceptance, n is the refractive index, which is usually air (n ~1). Diffraction-limited spatial resolution is close to the wavelength, λ, or equal if the NA is 0.62, which is the most common NA for IR microscope radiation (Griffiths & de Haseth, 2006). It is given by:

$$\text{Spatial resolution} = 0.61\,\lambda / \text{NA} \qquad 2.7$$

The response of an imaging system to a point source or point object is called the point spread function (PSF), which is affected by diffraction. After the light from a point source or point object passes through a tiny circular aperture, the diffraction-limited PSF known as the Airy Pattern is created on a focal plane. A brilliant centre area, known as the Airy disc, and concentric rings of varying intensities (decreasing from center to edge) for the Airy pattern (Findlay, 2018; Mattson et al., 2012). The capacity of a microscope to distinguish between two close Airy discs in a diffraction pattern is referred to as its resolution limit. Equation 2.7 originated from Rayleigh's criterion, which indicates that two points can be resolved if the centre of one Airy disc corresponds with the second Airy pattern's initial minimum (zero crossing). One drawback concluded from Equation 2.7 is that the nominal pixel resolution of IR-based microscopes will always be poorer than the microscope using visible light due to the long wavelength of mid-infrared light (λ=2.5–25 μm). This can be overcome using diffraction limited techniques detailed in the next sections (Lasch & Naumann, 2006).

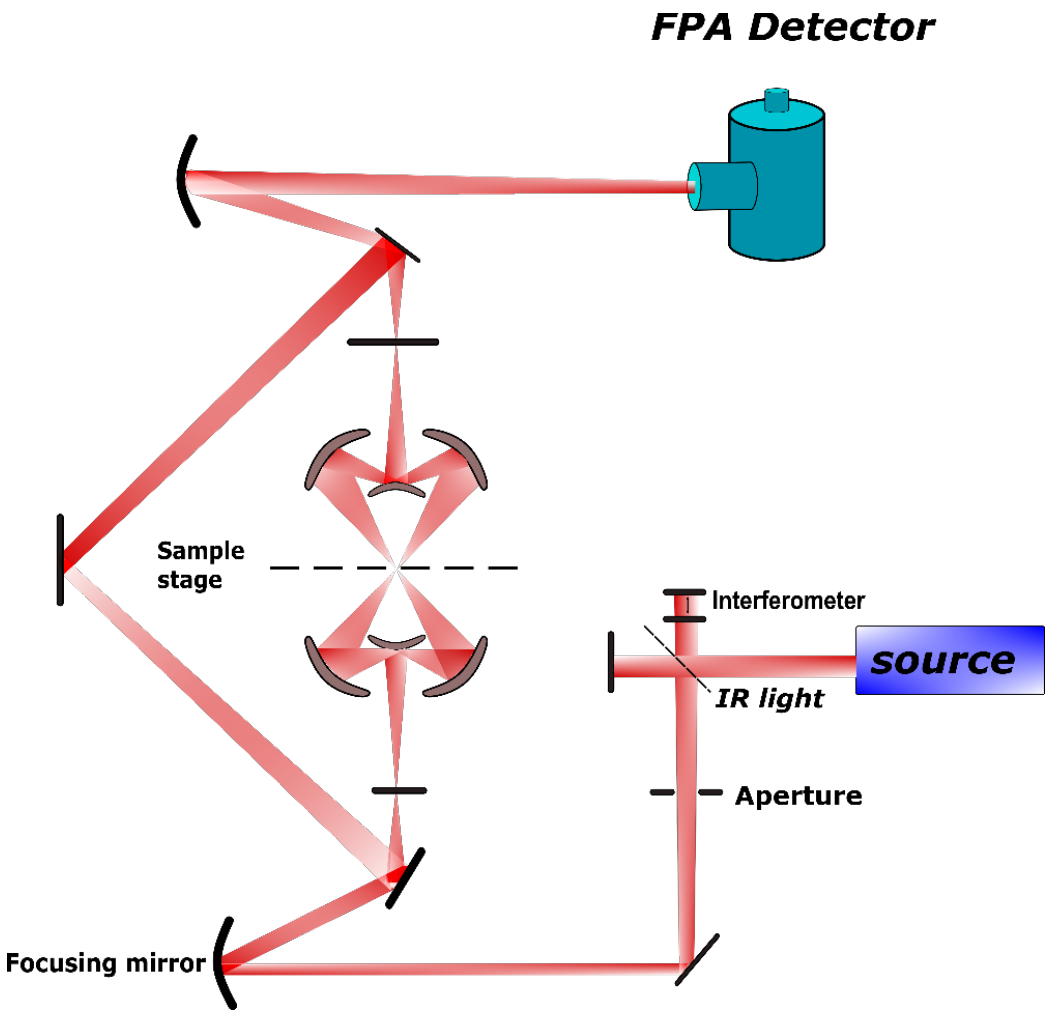

Figure 2.7. Schematic of FT-IR Microscope (G. Bakir, based on Agilent instrument manual). IR light from the source passes through the interferometer to the microscope. The Cassegrain mirror system focuses light on the sample and then carries the signal to be focused on the FPA. Each pixel in the array records an interferogram from the corresponding pixel area of the sample.

2.6.2 Far-field FTIR+ATR spectroscopy

Attenuated total reflection (ATR) has become one of the most commonly used techniques in IR spectrometry due to two major advantages, it requires minimal to no sample preparation and produces reliable results. ATR instruments are commercially designed much smaller and cheaper than regular transmission IR instruments. ATR is a technique that involves placing a sample in

contact with a Mid-IR internal reflection element (IRE) (**Figure 2.8**). The most common materials used as IRE are diamond, germanium, and zinc selenide. Because radiation is not passed through the entire sample, unlike many other sampling procedures used in IR spectrometry, the sample does not need to be thin enough to enable transmission of incoming radiation. Prior to-reaching a detector, the beam is internally reflected by a crystal one or more times (**Figure 2.8**).

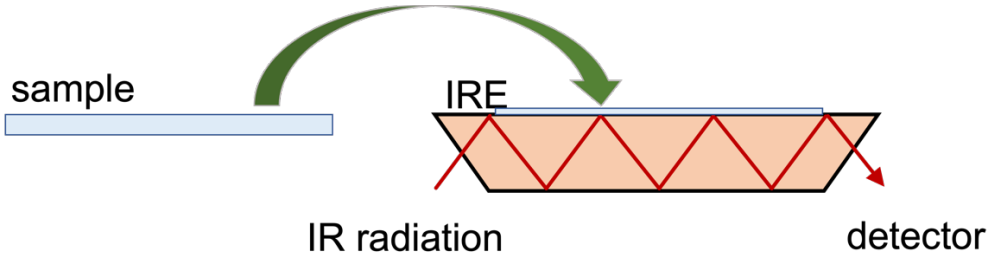

Figure 2.8. Total internal reflection in bulk ATR

The theory behind ATR is based on Snell's law: when light travels through two transparent media with different refractive indices, the angle at which the light is refracted changes. It is described by the Equation 2.8:

$$n_1 \sin \theta_1 = n_2 \sin \theta_2 \qquad 2.8$$

where n_1 and n_2 are the refractive indices of the two media, and θ_1 and θ_2 are, respectively, the angle of incoming and refracted light in relation to the normal to the interface. If the light comes from an optically dense medium to an optically rare medium, the angle of incidence is smaller than the angle of refraction (**Figure 2.9**).

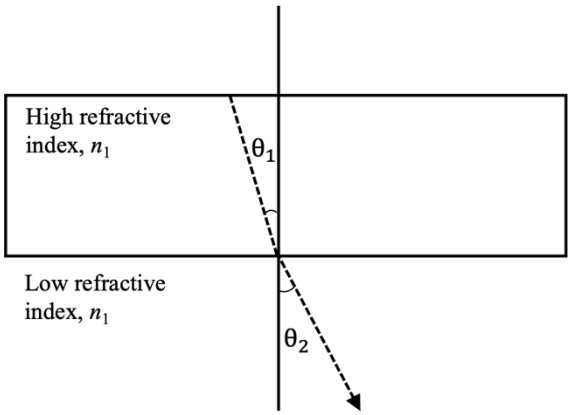

Figure 2.9. Illustration of Snell's Law. The beam travels from optically dense medium to the optically rare medium with an angle measured with respect to the normal to the surface.

According to Snell's law, the reflected angle becomes equal to 90° when θ_1 reaches to the critical angle (θ_c), that is, the smallest angle of incidence at which total internal reflection occurs, given by equation 2.9:

$$\theta_c = \sin^{-1}\frac{n_2}{n_1} \qquad 2.9$$

If the incident angle is greater than or equal to the critical angle, the beam then reflects internally in the optically dense medium (**Figure 2.10**).

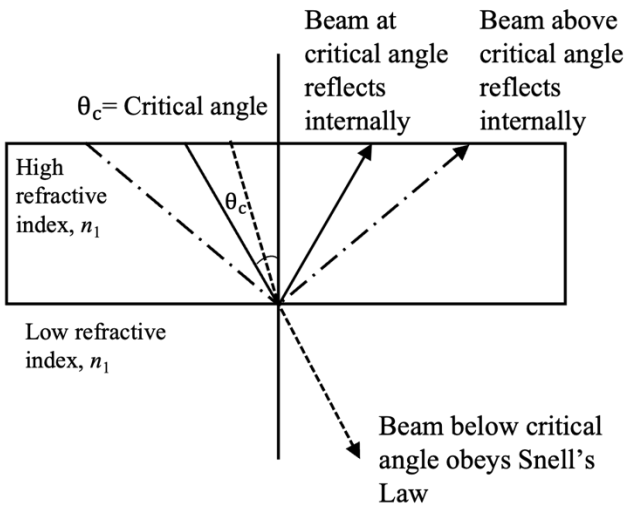

Figure 2.10. Paths of light according to Snell's law as the angle of incident light increases. (Adapted from Griffiths & de Haseth (2006)

A photon has an electromagnetic field that can penetrate into the sample. The field, which extends perpendicularly from the surface of the IRE into the optically rare medium, is called an evanescent wave (**Figure 2.11**). When the evanescent wave travels deeper into the sample, its strength, **E**, decays, and is thus a function of distance from the surface of the crystal, z:

$$\mathbf{E} = \mathbf{E}_0 e^{-\gamma z} \qquad 2.10$$

where $\mathbf{E}_0$ is the field strength at the surface and γ is a constant. The depth of the penetration, d_p, depends directly on the wavelength of the IR beam, according to:

$$d_p = \frac{\lambda}{2\pi n_1 \sqrt{\sin^2\theta - (n_2/n_1)^2}} \qquad 2.11$$

where λ is the wavelength of the IR light, n_1 is the refractive index of the IRE, n_2 is the refractive index of the sample and θ is the angle of incidence.

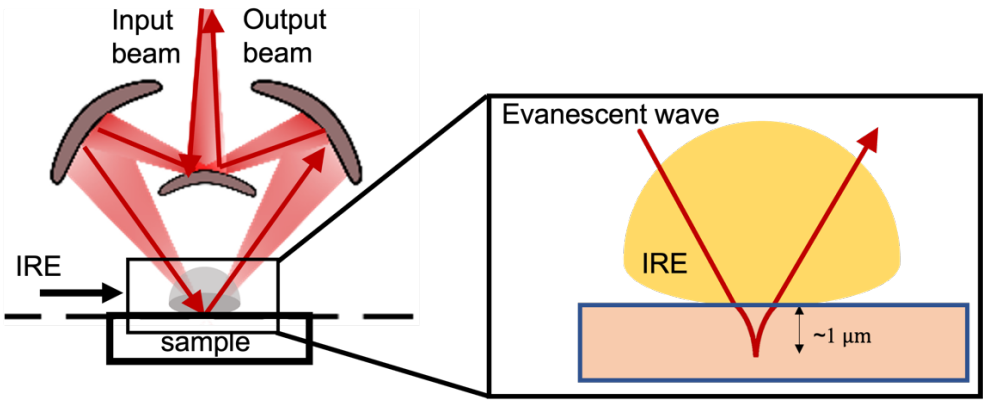

Figure 2.11 The evanescent wave penetration into the sample on the Agilent IR microscope (G.Bakir)

2.6.3 Near-field Nano-FTIR spectroscopy

The nano-FTIR technique employed in this thesis combines scattering-type Scanning Near-Field Optical Microscopy (s-SNOM) with Fourier-Transform Infrared (FT-IR) spectroscopy. It is based on a metalized atomic force microscope (AFM) tip; the sample is approached and scanned by the tip. Repulsive and attractive forces exist between the probe and the sample and are used to produce a high resolution three-dimensional topographical image of surfaces at the nm scale. In AFM, a tip positioned beneath a cantilever is raster scanned over the material's surface to determine the topographic image of the sample (**Figure 2.12**). The full data collection process at Advanced Light Source, Berkeley, USA and an example of sample preparation are explained in detail in Appendix I Section 2.10 and Appendix II Section 2.11.

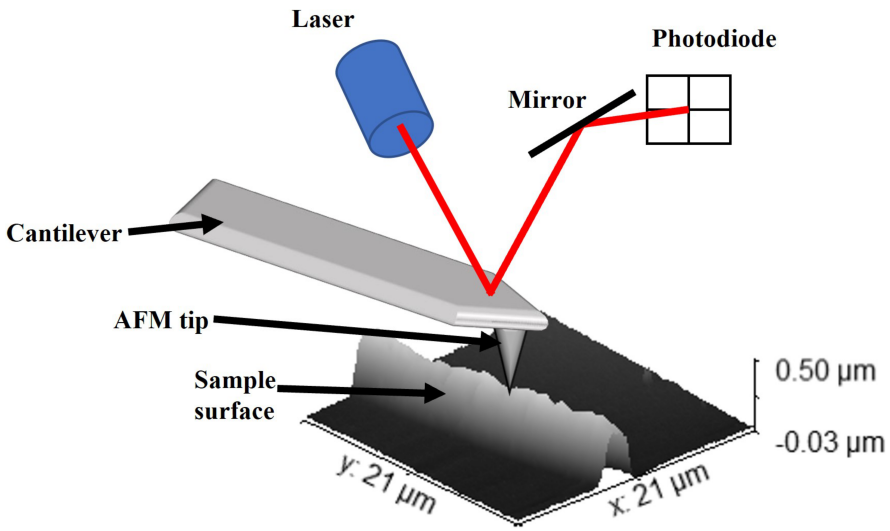

Figure 2.12 Basic AFM setup. Based on cover image of Chapter 5

The reverse (uppermost) side of the cantilever reflects the incident beam onto a position-sensitive photodetector, allowing changes to the deflection to be monitored. Variations in the material surface will result in minor changes in the position of the reflected light. Tapping (semi-contact), contact, or non-contact modes can all be used to operate an AFM (Johnson et al., 2009). The AFM tip is illuminated by intense IR light, which could be either monochromatic or broadband infrared radiation, to produce an infrared image together with topography (Huth et al., 2012).To produce a near-field image, the scattered IR light is recorded while scanning the sample surface (Hillenbrand et al., 2001; Keilmann & Hillenbrand, 2004). The conductive tip acts as an optical antenna by localizing and scattering the IR optical field in the near-field region of its nanoscopic apex. The radius of the tip apex is typically between 10-30 nm. The spatial resolution of the technique is wavelength independent and is limited only by the tip radius (Amenabar et al., 2017; Bechtel et

al., 2020). Consequently, the spatial resolution of s-SNOM is independent of the incident IR wavelength. When brought into proximity to a sample, the near field interacts with the sample and modifies the tip-scattered field, detected by a Michelson interferometer as a function of tip position, yielding two-dimensional (2D) monochromatic infrared amplitude and phase images (Amenabar et al., 2013; Mastel et al., 2018).

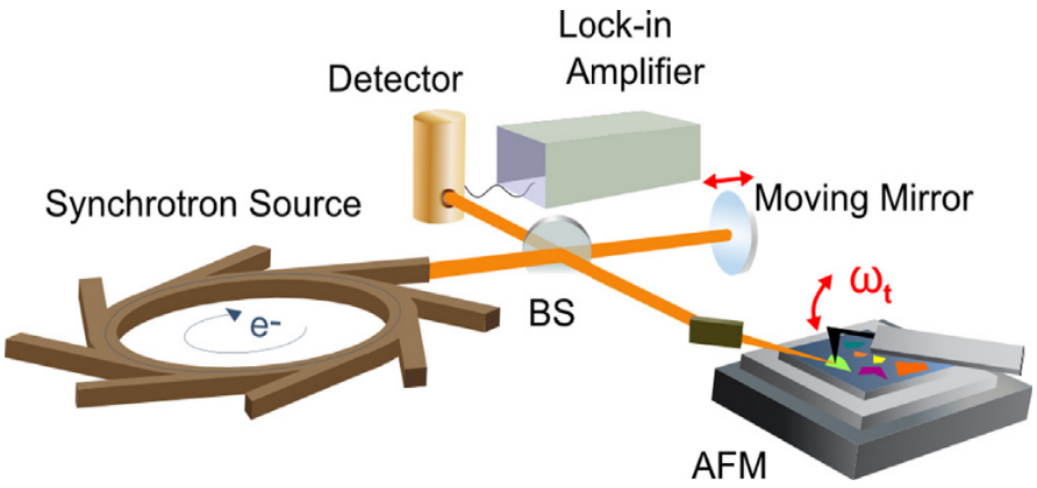

Figure 2.13. SINS schematic. Synchrotron infrared light enters an asymmetric Michelson interferometer, in which a beam splitter (BS) directs half the light to an atomic force microscope (AFM) tip and the other half to a moving mirror. The backscattered light from the tip and the reference beam are recombined on the beam splitter and detected by an IR detector and demodulated at the n-th harmonic of the tip tapping frequency ωt of AFM tip. (Bechtel 2020, with permission from Elsevier: License number: 5594890326254)

When the IR light is scattered from the tip, it is detected by the interferometer. The Fourier Transform of the interferogram results in the complex-valued near-field spectrum. The IR phase and amplitude spectra are obtained by demodulating the detector signal at a higher harmonic (nΩ) of the tip oscillation frequency. The real Re (ω) and imaginary Im (ω) spectra are calculated from spectral amplitude (s) and phase (φ) of the scattered light, which are related to the complex

dielectric function of the material. Fourier transform of the interferogram results in the complex-valued near field spectrum calculated from second-order scattering coefficient $\sigma_2(\omega)$. The equation is given by:

$$\mathrm{E_{sca}}(\omega) = \sigma_2(\omega)\,\mathrm{E_{inc}}(\omega) \tag{2.12}$$

where E_{sca} is the scattered field and E_{inc} is the incident field. The second-order scattering coefficient depends on s_2 and φ,

$$\sigma_2(\omega) = s_2(\omega)e^{i\varphi(\omega)} \tag{2.13}$$

The near-field nano FT-IR absorbance spectrum is obtained by normalizing the signal on the sample against a signal on a non-resonant flat surface (reference) and it is given by the equations:

$$\frac{\sigma_2(sample,\omega)}{\sigma_2(ref,\omega)} = \frac{s_2(sample,\omega)e^{i\varphi_2(sample,\omega)}}{s_2(ref,\omega)e^{i\varphi_2(ref,\omega)}} \tag{2.14}$$

$$= \frac{s_2(sample,\omega)}{s_2(ref,\omega)}e^{i[\varphi_2(sample,\omega)-\varphi_2(ref,\omega)]} \tag{2.15}$$

The near-field IR spectrum is found from the imaginary part of the equation 2.15 and is described by:

$$\mathrm{Im}[\sigma_2(\omega)] = \frac{s_2(sample,\omega)}{s_2(ref,\omega)}\sin[\varphi_2(sample,\omega)-\varphi_2(ref,\omega)] \tag{2.16}$$

2.6.4 Optical photothermal IR spectroscopy (O-PTIR)

O-PTIR imaging and spectroscopy methods are relatively new far-field IR techniques based on the photothermal effect. In this method, photothermal IR responses of the sample are detected, rather than from the direct absorbance of IR light as in traditional IR systems (FTIR). The spatial resolution is on the submicron scale (theoretically ~416 nm) and is wavelength independent, as far as the IR range is concerned. The resolution is determined by a probe laser (532 nm), which operates in the visible region. The general layout and an example from our experiments are shown in **Figure 2.14**, modified from (Bakir et al., 2020; Kansiz et al., 2020).

First, an IR beam from a pulsed tunable IR laser source, such as a Quantum Cascade Laser (QCL) or an optical parametric oscillator (OPO) laser, is used to illuminate the sample. For imaging, the IR laser may be set to a specific wavelength corresponding to an IR absorption band in the sample. Some of the IR light is absorbed and converted to heat, resulting in a temperature rise in the IR-absorbing regions of the sample. Local heating and thermal expansion cause alterations in the refractive index. Those changes in refractive index are detected using a shorter-wavelength visible laser, such as green at 532 nm, which focuses and overlaps onto the sample surface illuminated by IR light. A visible light detector is then used to track changes in the intensity of reflected green light. The wavelength of the visible probe beam, not the wavelength of the IR beam, determines the spatial resolution reached by O-PTIR (Equation 2.7). The spatial resolution is improved by the wavelength ratio between the IR and the probe (Kansiz et al., 2020). For the samples used for this thesis, the IR images were ratioed since the single wavelength images just show the intensity across the sample, which is affected by thickness at each point. For the case where the sample thickness is uniform, this step is not necessary.

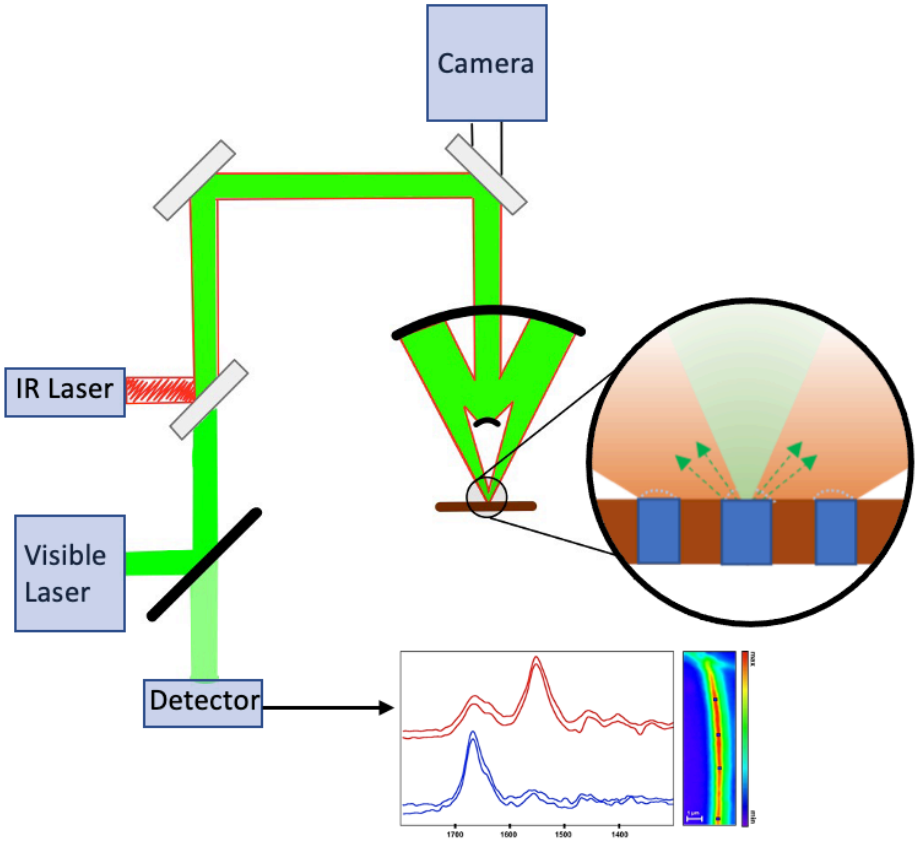

Figure 2.14. O-PTIR schematic (G.Bakir). Two laser beams (green, 532 nm, and a pulsed QCL IR suite of 4 chips) are combined collinearly through a dichroic mirror and focussed with a Schwarzchild objective. The QCL is either swept across the tunable range or used at a fixed frequency. If the frequency of the IR laser matches the vibrational energy of a transition in the sample, the IR light is absorbed, resulting in photothermal expansion. The thermal expansion changes the scattered or reflected visible light, which is measured by a visible detector, processed and reported as an IR absorption spectrum. The example shown here is from (Bakir et al. 2020).

2.7 Infrared spectra of biological samples

The typical IR spectra for biological molecules are well studied and the most important vibrational frequencies are well known. The mid-infrared range (MIR, 4000-400cm^{-1}) can be divided into two major regions: the higher- wavenumber region (2550-3500 cm^{-1}) and the lower-

wavenumber region (900-1800 cm^{-1}) also called the fingerprint region. Light atom-heavy atom stretching vibrations such as S-H, C-H, N-H, and O-H are found in higher energy-wavenumber regions. Some of the most important vibrational modes for biomolecules in the fingerprint region are described here. Proteins: Amide modes, characteristic for proteins, Amide I ~1650 cm^{-1} is mainly C=O bond stretch, Amide II ~1555 cm^{-1} is a mixture of the C-N stretch and H-N-C bend, and Amide III ~1350-1200 cm^{-1} is a combination of backbone modes that are not easily defined. Carbohydrates include C-O-C, C-C and C-O of the carbohydrate rings, 1200-800 cm^{-1} (Baker et al., 2014). Lipids include C-H stretching (3010-2800 cm^{-1}) C=O stretching (1750-1725 cm^{-1}), C-H bending (1465-1360 cm^{-1}), C-H rocking and wagging (1260-1250 cm^{-1}), C-O stretching (1180-1165 cm^{-1}), PO_2^- stretching (1230 and 1085 cm^{-1}). The spectra of nucleic acids can be split, according to the base, sugar, and phosphate functional groups. Some major modes are: 1800-1500 cm^{-1} (bases give purinic and pyrimidinic vibrations), 1500-1250 cm^{-1} (vibrations couple between a base and a sugar), 1250-1000 cm^{-1} (sugar-phosphate chain vibrations), 1000-800 cm^{-1} (sugar/sugar-phosphate vibrations) (Wood, 2016). The tables relevant to the each project are provided in each Chapter.

2.8 Polarization

When an unpolarized electromagnetic radiation beam is delivered in the z direction, the amplitudes of the sinusoidally changing electric field components in the x and y planes are equal. However, if the the light passes through a polarizer, only the component of the electric field in one plane can be transmitted. All gases and liquids, as well as isotropic solids, are unoriented samples and the polarizer has no effect on the IR absorbance of any of the bands in the spectrum. However, the molecules in a given sample might be oriented in a certain direction. In that case, there will be

a change in their dipole moment for the vibrational modes aligned with the direction of the light as defined by the rotation angle of the polarizer. In other words, only some specific modes can be excited in a molecule. As a result, the intensity of the bands in the spectrum changes.

For instance, considering our focus on the collagen molecule, in the Amide functional group (**Figure 2.15**), the C=O bonds are oriented at ~90° to the backbone. When it is excited by the polarized light perpendicular to the backbone, the Amide I band intensity increase relative to the Amide II band intensity. If the light is polarized parallel to the backbone, then Amide II band is preferentially excited by the light. As the intensities of Amide I and II bands are sensitive to the orientation of the incoming light, in this thesis polarized light is used to investigate the orientation of collagen in a variety of tendons and fibrils.

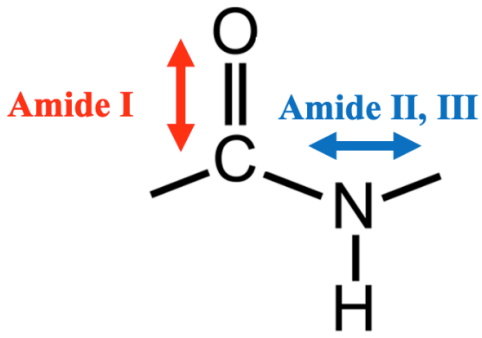

Figure 2.15 Amide functional group. Amide I, II &III modes

2.9 References

Amenabar, I., Poly, S., Goikoetxea, M., Nuansing, W., Lasch, P., & Hillenbrand, R. (2017). Hyperspectral infrared nanoimaging of organic samples based on Fourier transform infrared nanospectroscopy. *Nature Communications*, *8*(1), 14402. https://doi.org/10.1038/ncomms14402

Amenabar, I., Poly, S., Nuansing, W., Hubrich, E. H., Govyadinov, A. A., Huth, F., Krutokhvostov, R., Zhang, L., Knez, M., Heberle, J., Bittner, A. M., & Hillenbrand, R. (2013). Structural analysis and mapping of individual protein complexes by infrared nanospectroscopy. *Nature Communications*, *4*, 1–9. https://doi.org/10.1038/ncomms3890

Baker, M. J., Trevisan, J., Bassan, P., Bhargava, R., Butler, H. J., Dorling, K. M., Fielden, P. R., Fogarty, S. W., Fullwood, N. J., Heys, K. A., Hughes, C., Lasch, P., Martin-Hirsch, P. L., Obinaju, B., Sockalingum, G. D., Sulé-Suso, J., Strong, R. J., Walsh, M. J., Wood, B. R., … Martin, F. L. (2014). Using Fourier transform IR spectroscopy to analyze biological materials. *Nature Protocols*, *9*(8), 1771–1791. https://doi.org/10.1038/nprot.2014.110

Bakir, G., Girouard, B. E., Wiens, R., Mastel, S., Dillon, E., Kansiz, M., & Gough, K. M. (2020). Orientation Matters: Polarization Dependent IR Spectroscopy of Collagen from Intact Tendon Down to the Single Fibril Level. *Molecules*, *25*(18), 4295. https://doi.org/10.3390/molecules25184295

Bechtel, H. A., Johnson, S. C., Khatib, O., Muller, E. A., & Raschke, M. B. (2020). Synchrotron infrared nano-spectroscopy and -imaging. *Surface Science Reports*, *75*(3), 100493. https://doi.org/10.1016/j.surfrep.2020.100493

Chalmers, J. M., & Griffiths, P. R. (2002). Handbook of vibrational spectroscopy . In *Vibrational spectroscopy.* John Wiley & Sons.

Findlay, C. R. J. (2018). *Development of FTIR tomography for thermal-source imaging of 3D biochemical distributions in micro-samples of cells and fibers*. https://doi.org/0.5203/THESIS_FINDLAY_1

Griffiths, P. R., & de Haseth, J. A. (2006). Fourier Transform Infrared Spectrometry: Second Edition. In *Fourier Transform Infrared Spectrometry: Second Edition*. https://doi.org/10.1002/047010631X

Hillenbrand, R., Knoll, B., & Keilmann, F. (2001). Pure optical contrast in scattering-type scanning near-field microscopy. *Journal of Microscopy*, *202*(1), 77–83. https://doi.org/10.1046/j.1365-2818.2001.00794.x

Hollas, J. M. (2005). Modern Spectroscopy, 4th Edition. *Journal of Chemical Education*. https://doi.org/10.1021/ed082p43.1

Huth, F., Govyadinov, A., Amarie, S., Nuansing, W., Keilmann, F., & Hillenbrand, R. (2012). Nano-FTIR absorption spectroscopy of molecular fingerprints at 20 nm spatial resolution. *Nano Letters*, *12*(8), 3973–3978. https://doi.org/10.1021/nl301159v

Johnson, D., Hilal, N., & Bowen, W. R. (2009). Basic Principles of Atomic Force Microscopy. In *Atomic Force Microscopy in Process Engineering* (pp. 1–30). Elsevier. https://doi.org/10.1016/B978-1-85617-517-3.00001-8

Kansiz, M., Prater, C., Dillon, E., Lo, M., Anderson, J., Marcott, C., Demissie, A., Chen, Y., & Kunkel, G. (2020). Optical Photothermal Infrared Microspectroscopy with Simultaneous Raman – A New Non-Contact Failure Analysis Technique for Identification of <10 μm Organic Contamination in the Hard Drive and other Electronics Industries. *Microscopy Today*, *28*(3), 26–36. https://doi.org/10.1017/S1551929520000917

Keilmann, F., & Hillenbrand, R. (2004). Near-field microscopy by elastic light scattering from a tip. *Philosophical Transactions of the Royal Society A: Mathematical, Physical and Engineering Sciences*, *362*(1817), 787–805. https://doi.org/10.1098/rsta.2003.1347

Larkin, P. (Peter J.). (2011). *Infrared and Raman spectroscopy : principles and spectral interpretation* . Elsevier.

Lasch, P., & Naumann, D. (2006). Spatial resolution in infrared microspectroscopic imaging of tissues. *Biochimica et Biophysica Acta - Biomembranes*, *1758*(7), 814–829. https://doi.org/10.1016/j.bbamem.2006.06.008

Mastel, S., Govyadinov, A. A., Maissen, C., Chuvilin, A., Berger, A., & Hillenbrand, R. (2018). Understanding the Image Contrast of Material Boundaries in IR Nanoscopy Reaching 5 nm Spatial Resolution. *ACS Photonics*, *5*(8), 3372–3378. https://doi.org/10.1021/acsphotonics.8b00636

Mattson, E. C., Nasse, M. J., Rak, M., Gough, K. M., & Hirschmugl, C. J. (2012). Restoration and Spectral Recovery of Mid-Infrared Chemical Images. *Analytical Chemistry*, *84*(14), 6173–6180. https://doi.org/10.1021/ac301080h

Nasse, M. J., Walsh, M. J., Mattson, E. C., Reininger, R., Kajdacsy-Balla, A., Macias, V., Bhargava, R., & Hirschmugl, C. J. (2011). High-resolution Fourier-transform infrared chemical imaging with multiple synchrotron beams. *Nature Methods*, *8*(5), 413–416. https://doi.org/10.1038/nmeth.1585

Salzer, R., & Siesler, H. W. (2009). *Infrared and Raman spectroscopic imaging* . Wiley-VCH.

Skoog, D. A., West, D. M., Holler, F. J., & Crouch, S. R. (2014). Fundamentals of analytical chemistry. In D. A. Skoog, D. M. West, F. J. Holler, & S. R. Crouch (Eds.), *Analytical chemistry* (Ninth edit). Brooks/Cole, Cengage Learning.

Wood, B. R. (2016). The importance of hydration and DNA conformation in interpreting infrared spectra of cells and tissues. *Chemical Society Reviews*, *45*(7), 1980–1998. https://doi.org/10.1039/C5CS00511F

Yarris, L. (1993). Lighting the Way. *Lawrence Berkeley Laboratory Research Review.*, *18*(1), 1–11.

2.10 Appendix I

This appendix shows images to illustrate the steps for sample preparation and data acquisition. The purpose of these Appendices is to provide a concise illustration of the step-by-step process that I developed, based on methods originally described by our collaborators and modified in the Gough Lab, for the correct preparation of samples for nano-FTIR analysis. This practical guide is intended to assist individuals interested in using this approach to study collagen fibrils, regardless of source. Whether conducting in-person or remote analyses, criteria for the selection of good targets remain essential to obtain meaningful data. Section 2.10.2 offers a visual guide highlighting the crucial requirements for choosing suitable targets. This guidance is of utmost importance for remote data collection, particularly when access to beamtime is limited, and the beamline scientists lack familiarity with the sample. Failure to adhere to these criteria can result in spending a significant amount of time simply locating useful targets.

2.10.1 Sample preparation:

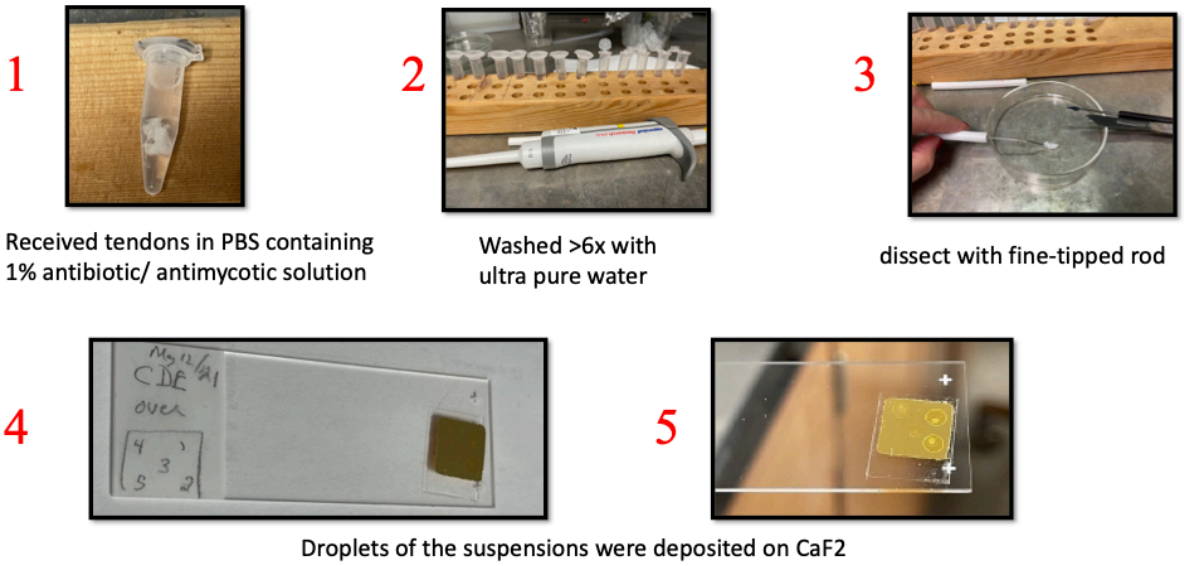

Image 1. Tendon sections dissected from the forelimb are sent from collaborators at Dalhousie University after undergoing mechanical stress, along with control, unstressed tendon sections. A segment approximately 10 mm long by 4 mm in diameter is in PBS, containing 1% antibiotic/antimycotic solution and 1% of protease inhibitor and shipped overnight to the University of Manitoba, where they were immediately washed and rinsed in ultra-pure water.

Image 2. The washed tendon segments are transferred to a 1.5 mL Eppendorf with ultra-pure water, soaked for 20 minutes and centrifuged for 5 min at 5300 ×g. This is repeated 6 times to remove all impurities coming from the PBS medium.

Image 3. The rinsed segment is dissected using tweezers and a finely-tipped metal rod within 1 mL of ultra-pure water. This process continues until the mixture takes on a cloudy appearance, signifying the releasing of individual collagen fibrils into the pure water. This

approach, as employed by Quigley (2016), is undertaken with the assumption that no additional harm is inflicted upon the collagen fibrils.

Image 4. Droplets of the suspensions are deposited on 1 cm^2 stripped gold squares (Platypus Technologies LLC) for nano-FTIR analysis.

2.10.2 Target Selection

The samples are shipped to ALS to work remotely (after Covid), or we go on-site as a beamline user (before Covid). The following is a typical PowerPoint document, including all information from selected targets whether for in person or remote data collection. They were critical for remote data collection to enable to ALS beam line scientists to locate our targets. This example document has been similarly prepared for all ALS trips since 2019.

- First page: Cover page identifying all samples as prepared on microscope slides
- Next 12 pages: Images for each selected target from May 2022 ALS beamtime. Each page provides the following information:

1. Each droplet is examined under a dark and bright field microscope to select the best target for near-field IR data acquisition. Example slides show photos taken under the microscope with different magnifications (5x to 100x) for each droplet.
2. Each droplet might include kinked (damaged) or straight (control) fibrils. Finding and selecting the kinked fibrils for mechanically damaged fibril samples is essential. Based on our experience, we know how a proper target should appear under each specific magnification. For example, under 50x magnification, a possible target should be small and a faint blue and as shown inside the red circle. If it is damaged, the target should include bright spots indicating bulges or kinks. Each possible target is named (fibril A, B, C etc.).

SDF& CDE OVER

May-June 2022, ALS

PowerPoint summary

SDF CON
- Slide #2, drop 4 fibril A
- Slide #3 drop 4 fibrils B & C

SDF OVER
- Slide #4, drop 5 fibril A
- Slide #5, drop 3, fibrils B,C
- Slide #6, drop 3, fibril D

CDE CON
- Slide #7, drop 4, fibril A
- Slide #8, drop 3, fibril B
- Slide #9, drop 3, fibril C

CDE OVER
- Slide #10, drop 5, fibrils A,B,C
- Slide #11, drop 5, fibril D,E
- Slide #12, drop 5, fibril F

NOTES:

1. Black ink dot in upper left corner of each Au square, for orientation. All photos on subsequent pages are rotated 180 degrees relative to the microscope slide layout. Rotated Au squares are shown on each page, to help visualize locations.

2. All samples are on stripped Au Platypus squares, prepared fresh just before mounting.

Selecting targets

Light microscope – Dark Field Photos

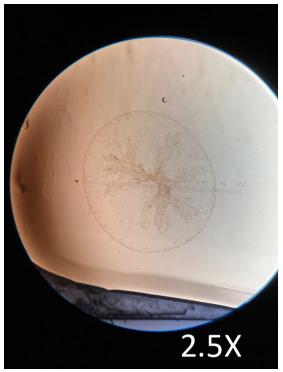

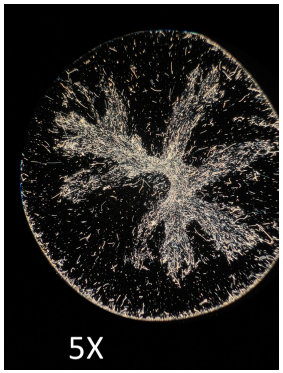

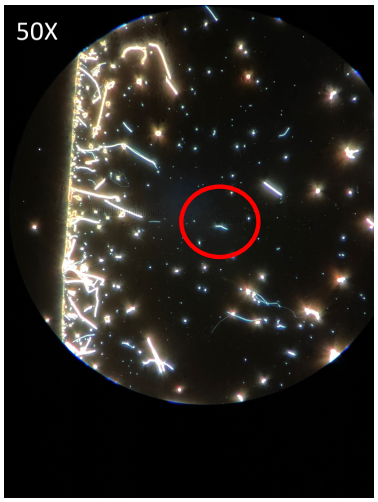

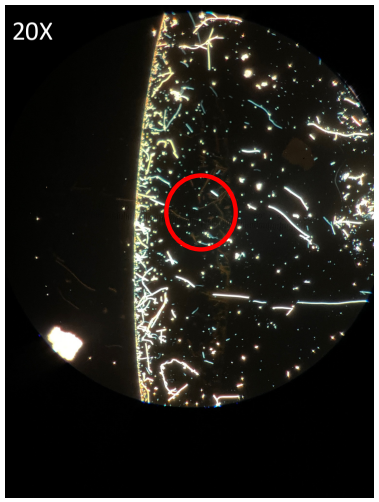

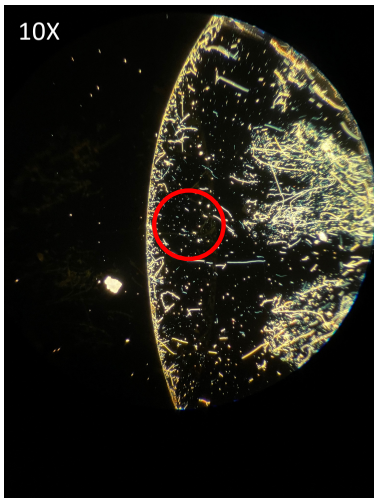

SDF CON DROP 4
Fibril A

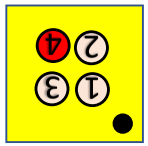

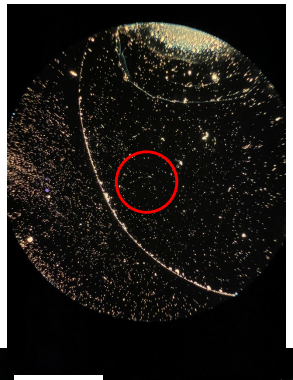

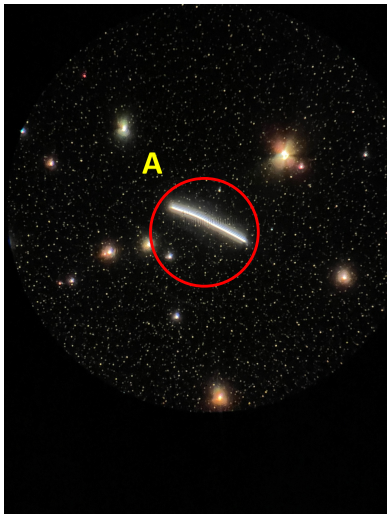

100x

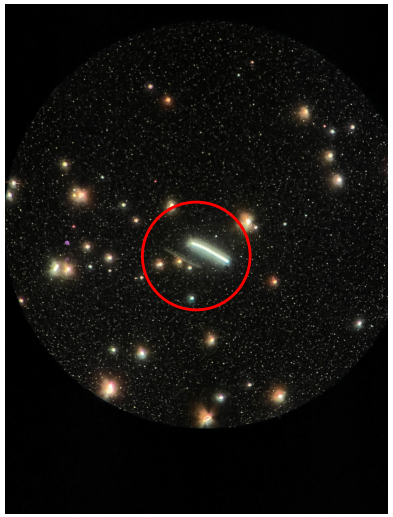

20x

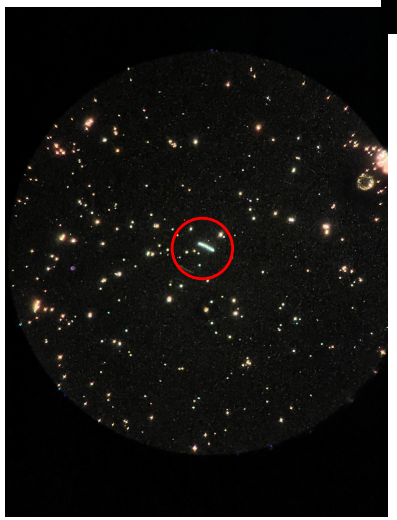

10x

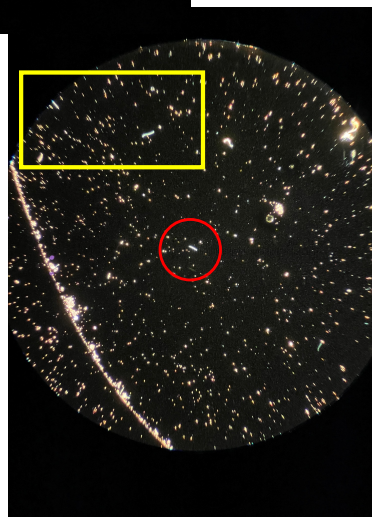

5x

SDF CON DROP4

Fibrils B & C

Inside yellow rectangle
close to fibril A in previous slide

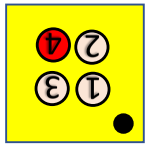

B looks cleaner than C

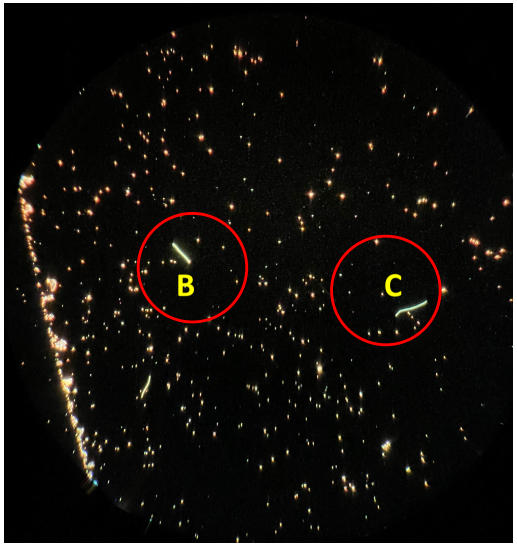

20x

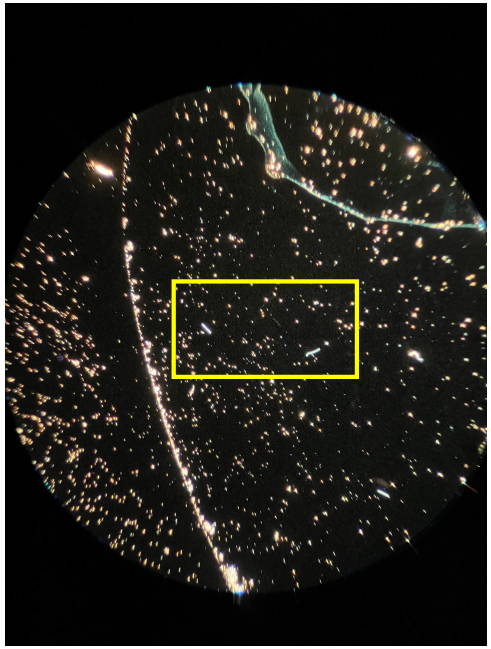

10x

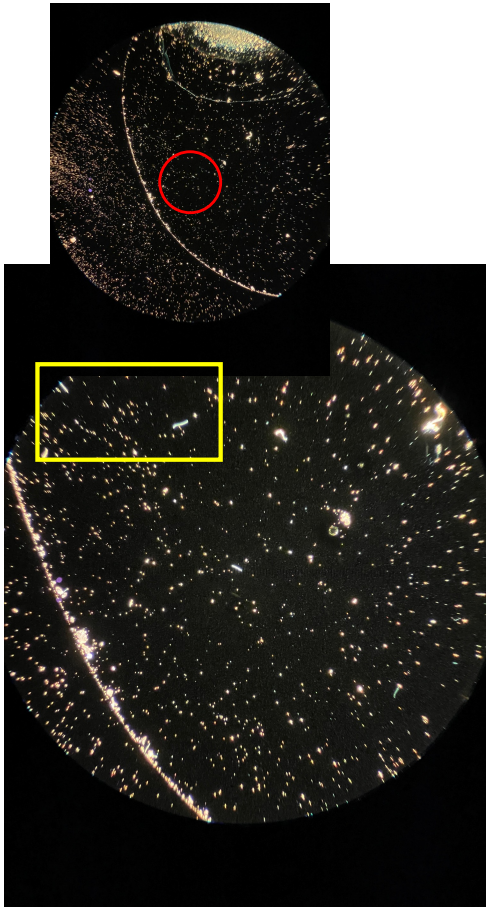

5x

SDF OVER, DROP 5
fibril A

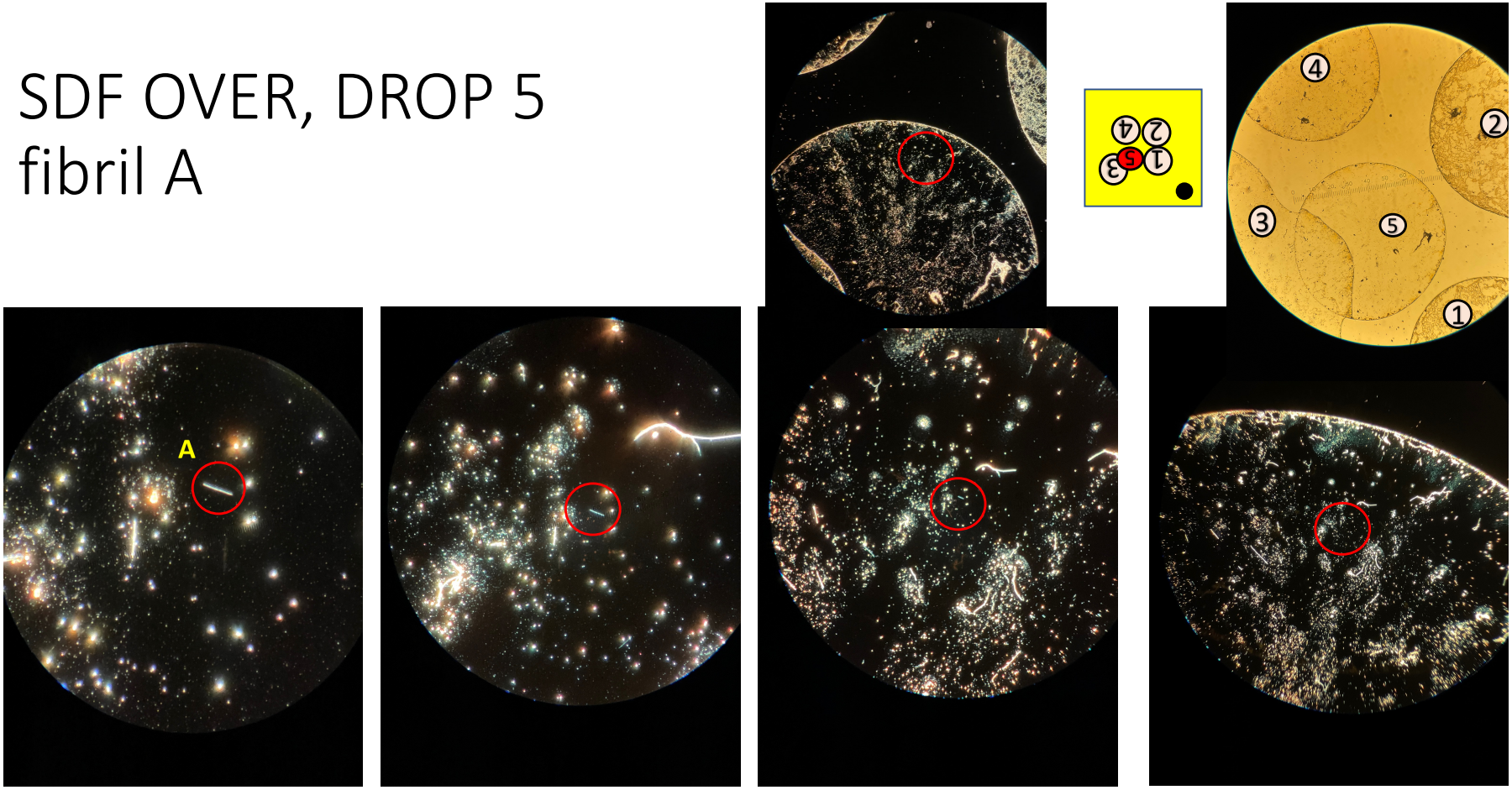

SDF OVER, DROP 3
Fibrils B and C

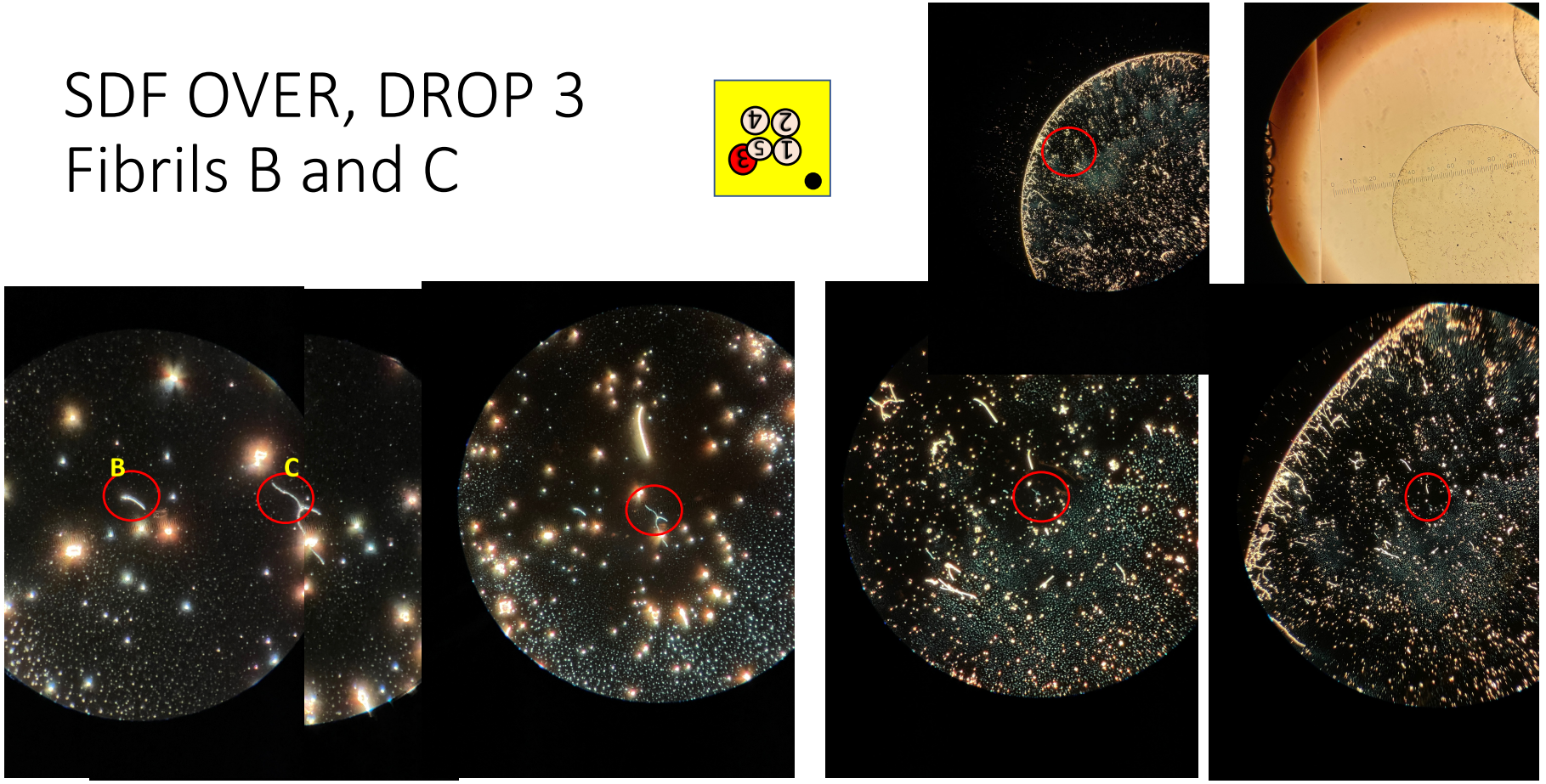

100x 50X 20x 10x

SDF OVER, DROP 3
Fibril D

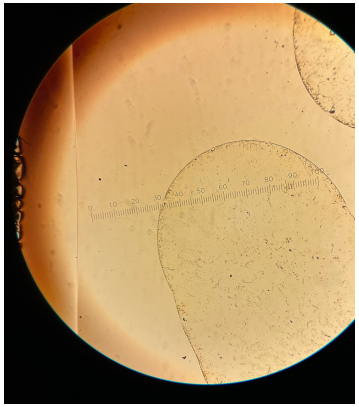

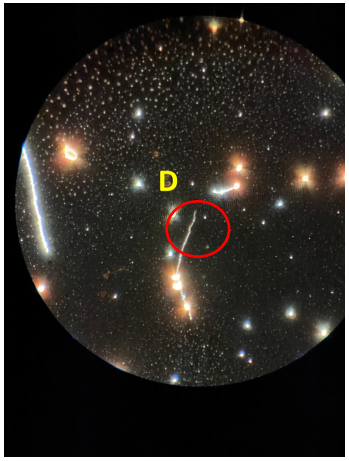

100x

50X

20x

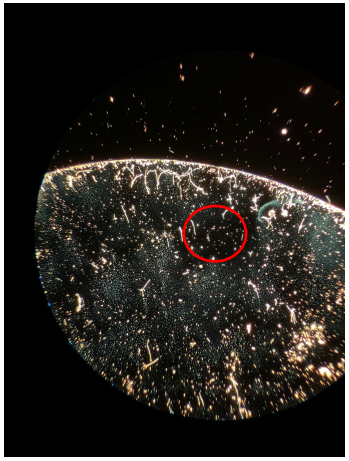

10x

CDE CON DROP 4
Fibril A

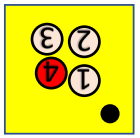

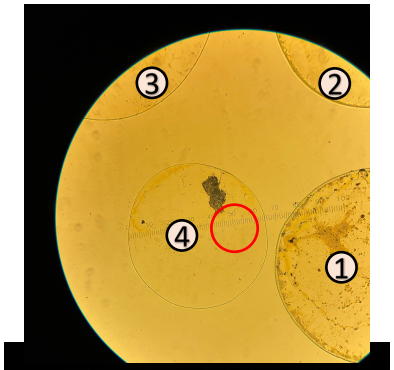

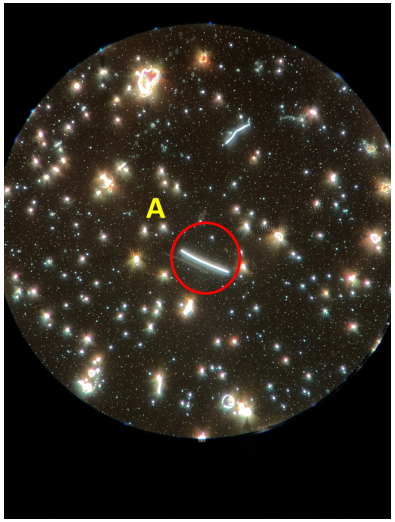

50X

20x

10x

5X

CDE CON DROP 3

Fibril B (Note that C is inside Yellow rectangle)

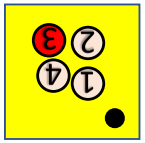

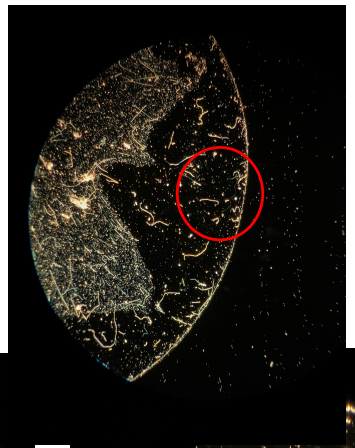

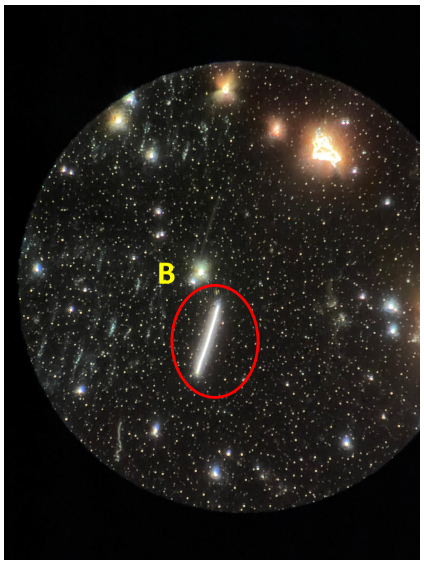

100X

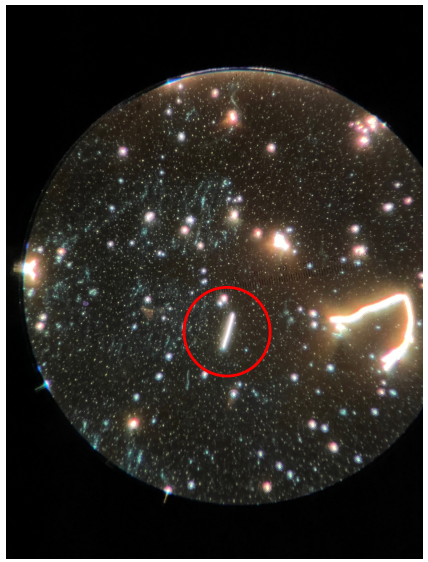

50X

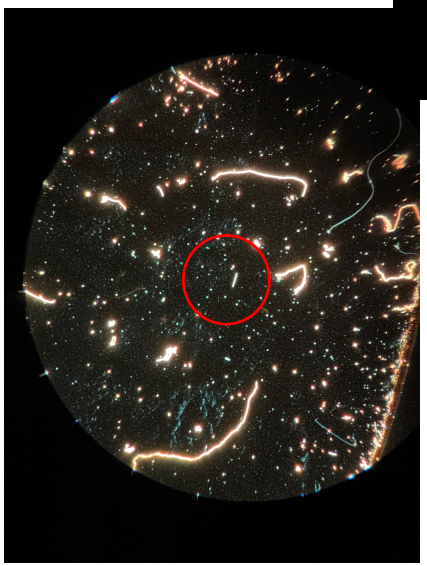

20x

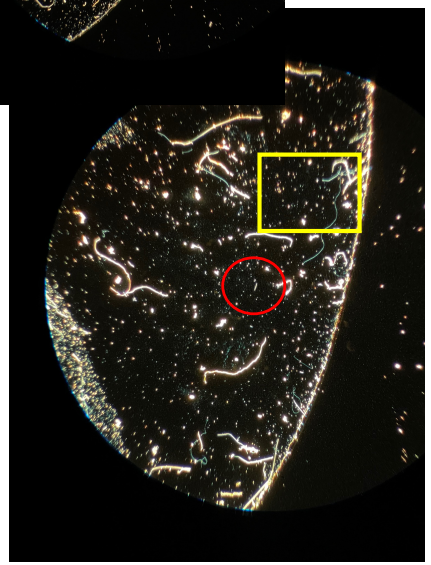

10x

CDE CON DROP 3
Fibril C

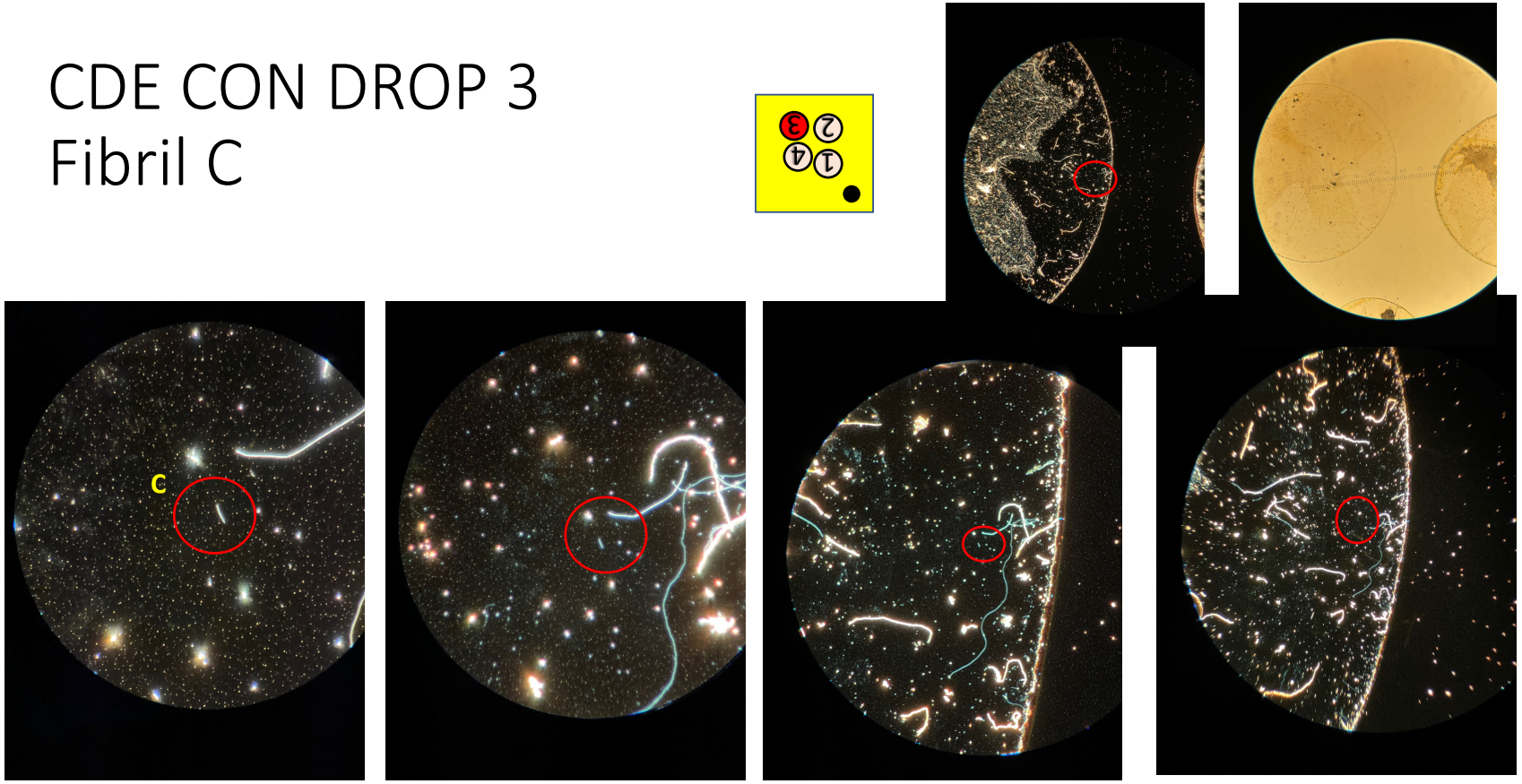

100X 50X 20x 10x

CDE OVER DROP 5

Fibrils A, B and C

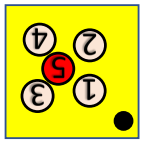

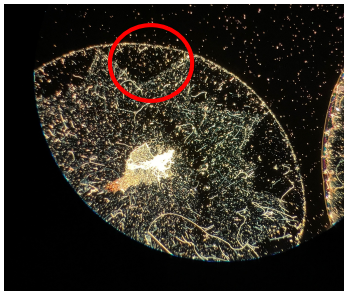

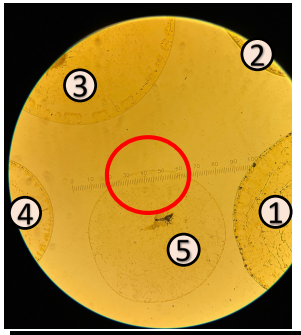

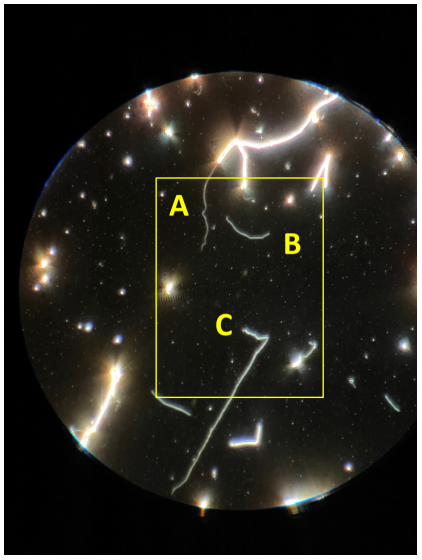

100X

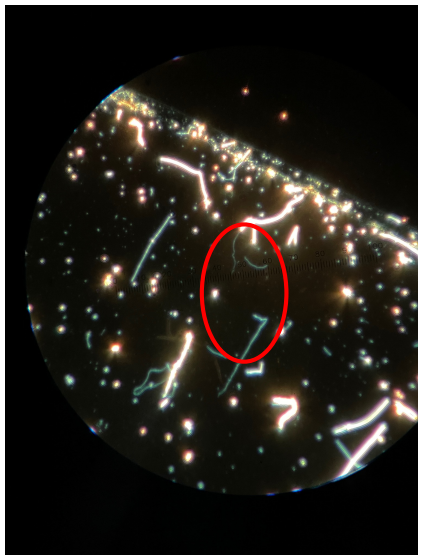

50X

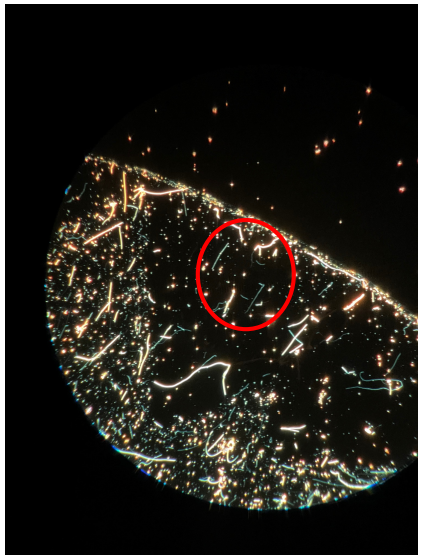

20x

10x

CDE OVER DROP 5
Fibrils D and E

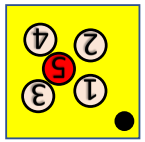

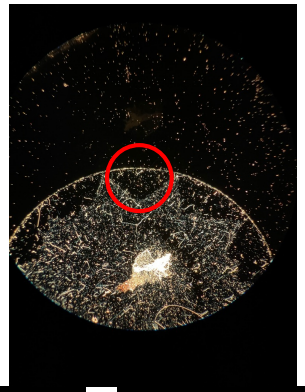

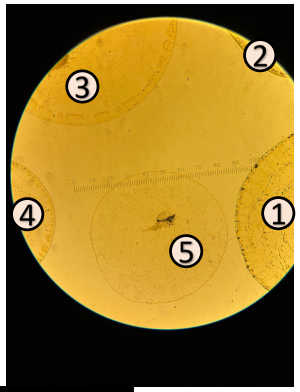

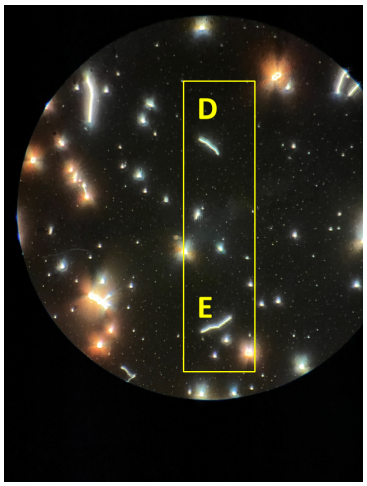

100X

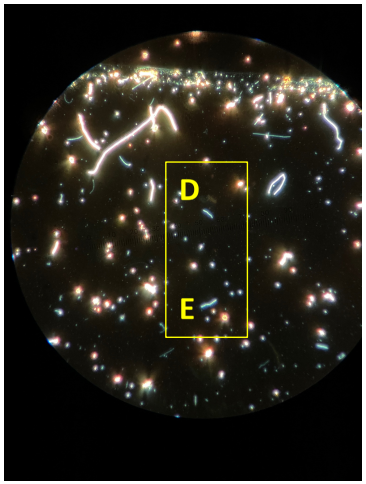

50X

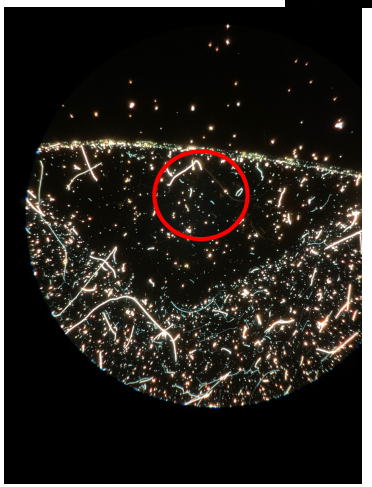

20x

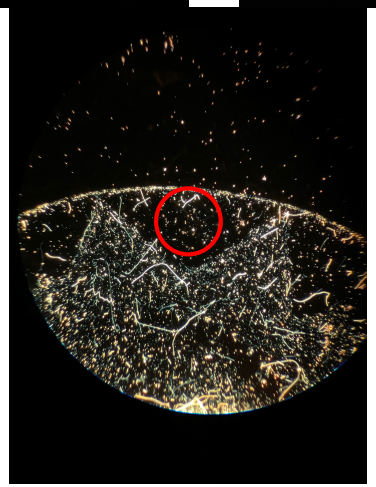

10x

CDE OVER DROP 5
Fibril F

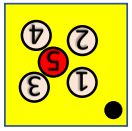

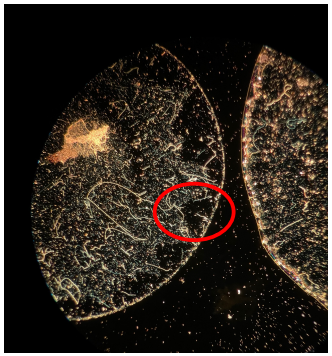

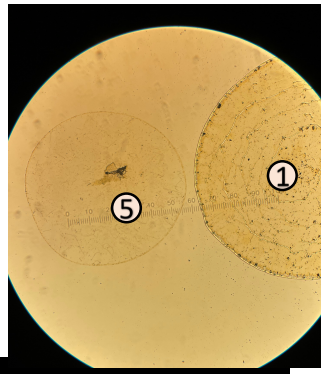

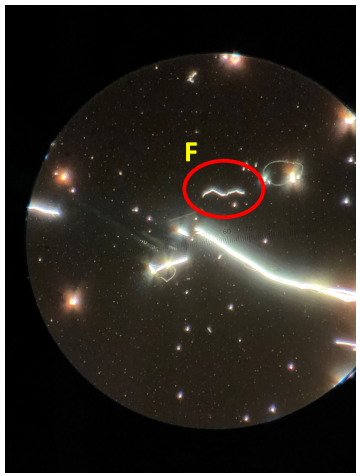

100X

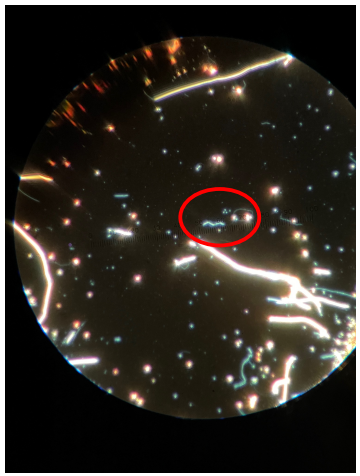

50X

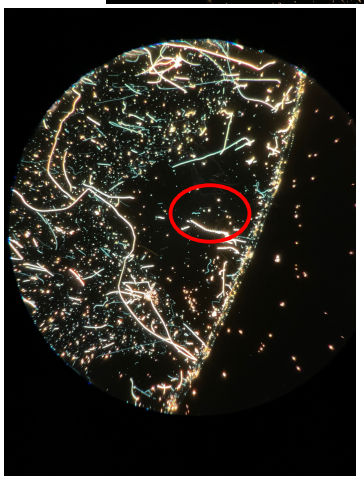

20x

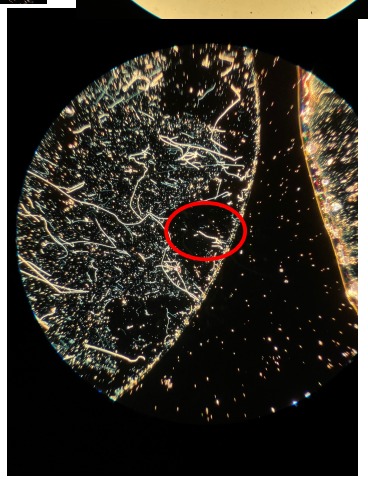

10x

2.11 Appendix II

This appendix shows the steps for data acquisition at the ALS with the Neaspec instrument and SINS. This brief synopsis serves as an illustration of the present steps necessary for obtaining spectra. It aids the reader in appreciating the detail and effort required to get reliable data. The next two pages are screenshots of the Neaspec software obtained while collecting fibril data in May 2022. The first page is the AFM scanning page, and the second is the spectrum acquisition window. The steps below refer to the numbered locations on these screen captures.

2.11.1 Neaspec steps:

Box 1: Sample window. It is the brightfield top-down view from the microscope. The target is under the cantilever.

Box 2: The scan window. It contains several parameters for collecting the Atomic Force Microscope image. In the first scan, a large area (10x10 microns) is scanned to find the target fibril. Once the fibril is located, a smaller area (2x2 or 1x1 micron) is scanned to obtain detailed view.

Box 3: This window is an example of optional AFM views. This AFM image is showing different ways of visualizing the sample under the AFM tip. There are more than 10 options. Here the images to topographical (the Z height) and tapping images, as well as the total infrared absorbance (yellow: no absorbance; red: strongly absorbing, bottom right). Once imaging is complete, we proceed to the next screen.

Box 4: Nano FTIR Spectroscopy window, *Take Spectrum* box: the parameters in that box are adjusted based on the experiment type.

Box 5: Once the background has been acquired, a point is chosen on the fibril and click the play button to collect a spectrum.

Box 6: As soon as the data collection has started the spectrum is name. The screen shows the real and imaginary or amplitude and phase spectra simultaneously as well as the interferogram (top). Right after collection of a few Spectra it's necessary to return to the previous screen and get a fresh AFM to ensure still on the target area to verify that the target has not drifted. Collecting data from one fibril usually takes 1-2 days.

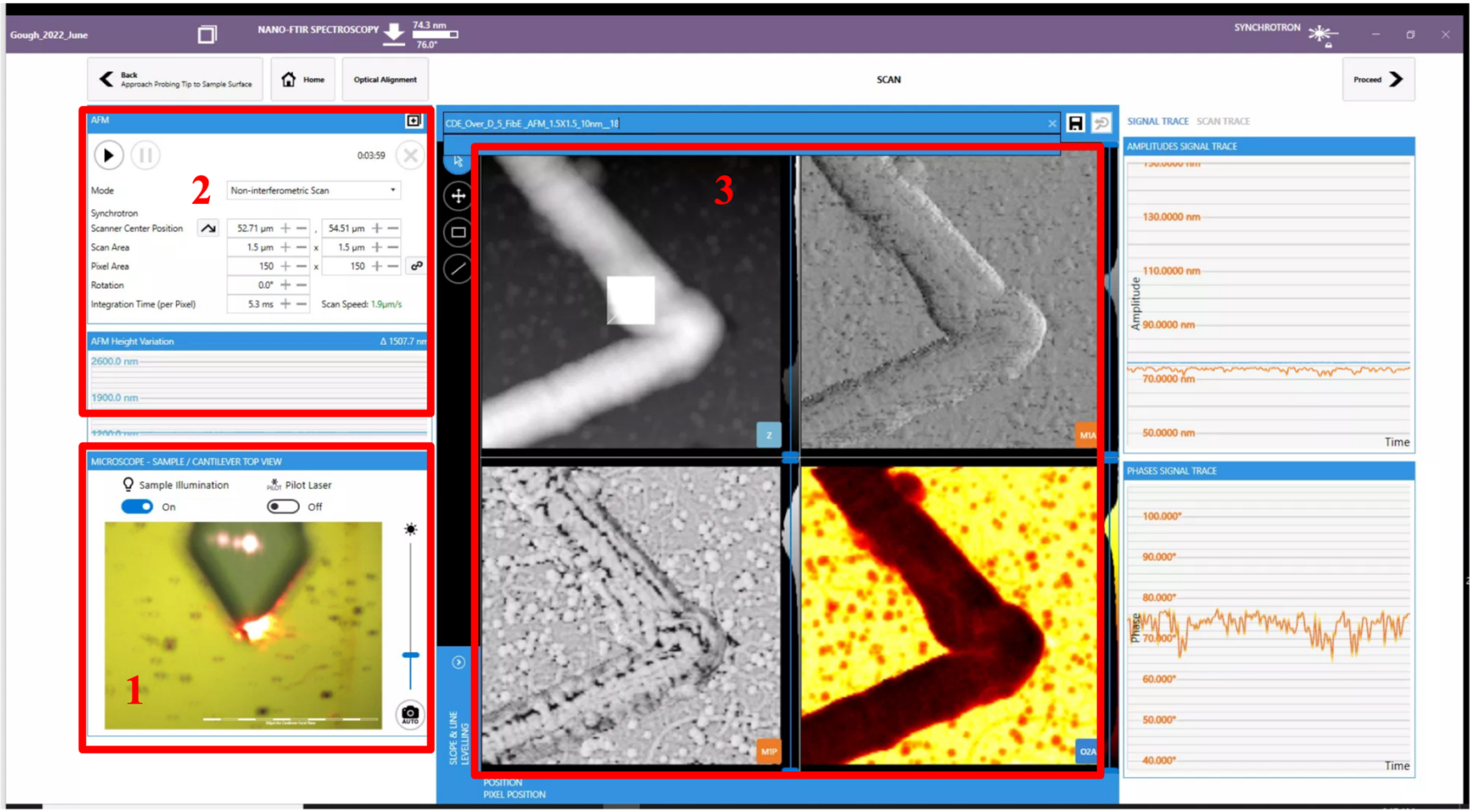
Gough_2022_June
NANO-FTIR SPECTROSCOPY
74.3 nm
76.0°
SYNCHROTRON
Back
Approach Probing Tip to Sample Surface
Home
Optical Alignment
SCAN
Proceed
AFM
0:03:59
Mode
Non-interferometric Scan
Synchrotron
Scanner Center Position
52.71 µm
54.51 µm
Scan Area
1.5 µm
1.5 µm
Pixel Area
150
150
Rotation
0.0°
Integration Time (per Pixel)
5.3 ms
Scan Speed: 1.9µm/s
AFM Height Variation
Δ 1507.7 nm
2600.0 nm
1900.0 nm
MICROSCOPE - SAMPLE / CANTILEVER TOP VIEW
Sample Illumination
Pilot Laser
On
Off
AUTO
1
2
3
CDE_Over_D_5_FibE_AFM_1.5X1.5_10nm_18
Z
M1A
MIP
O2A
SLOPE & LINE LEVELING
POSITION
PIXEL POSITION
SIGNAL TRACE
SCAN TRACE
AMPLITUDES SIGNAL TRACE
130.0000 nm
110.0000 nm
90.0000 nm
70.0000 nm
50.0000 nm
Amplitude
Time
PHASES SIGNAL TRACE
100.000°
90.000°
80.000°
70.000°
60.000°
50.000°
40.000°
Phase
Time

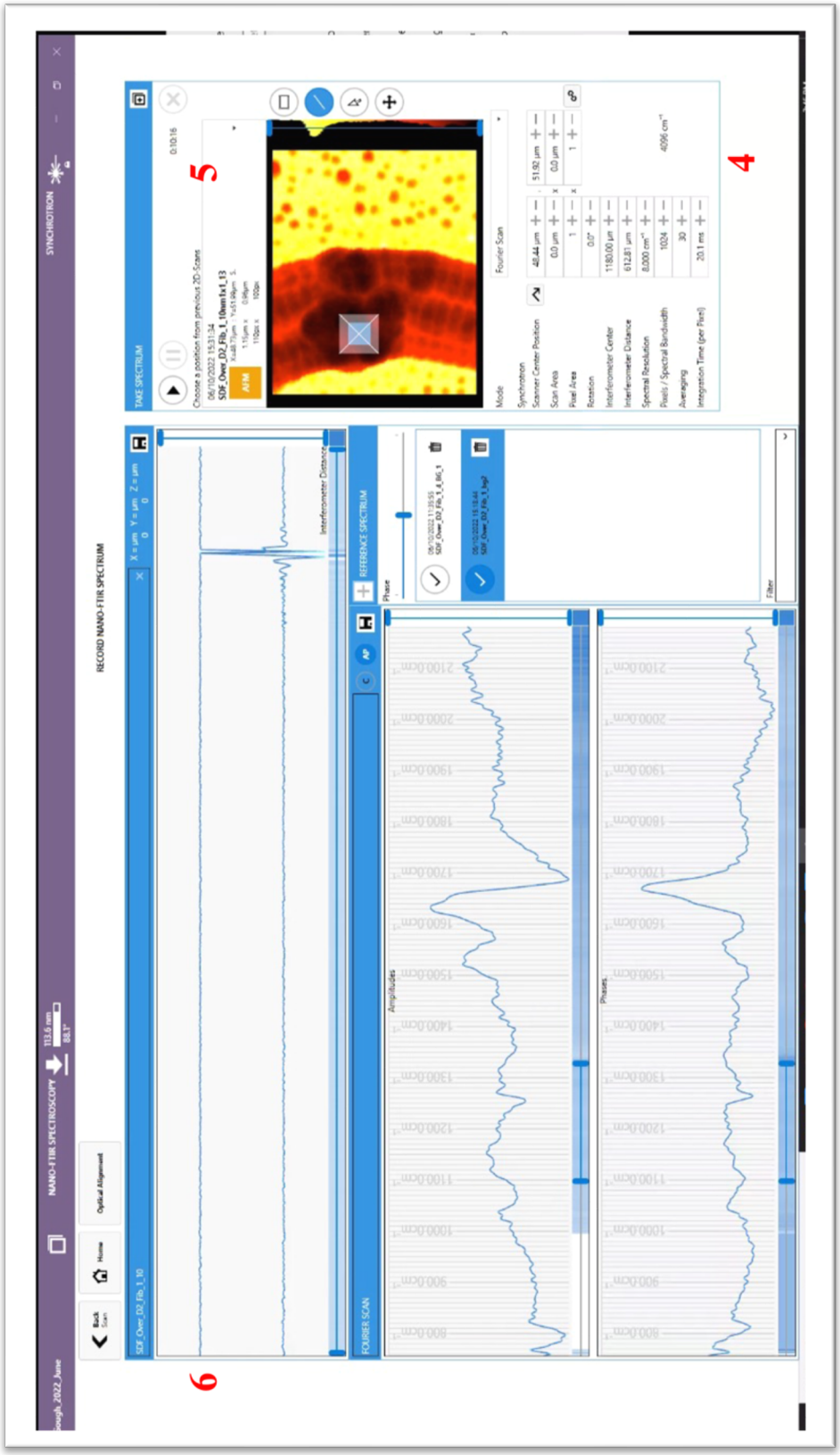
NANO-FTIR SPECTROSCOPY
SYNCHROTRON
RECORD NANO-FTIR SPECTRUM
TAKE SPECTRUM
REFERENCE SPECTRUM
FOURIER SCAN
Interferometer Distance
Amplitudes
Phases
4
5
6

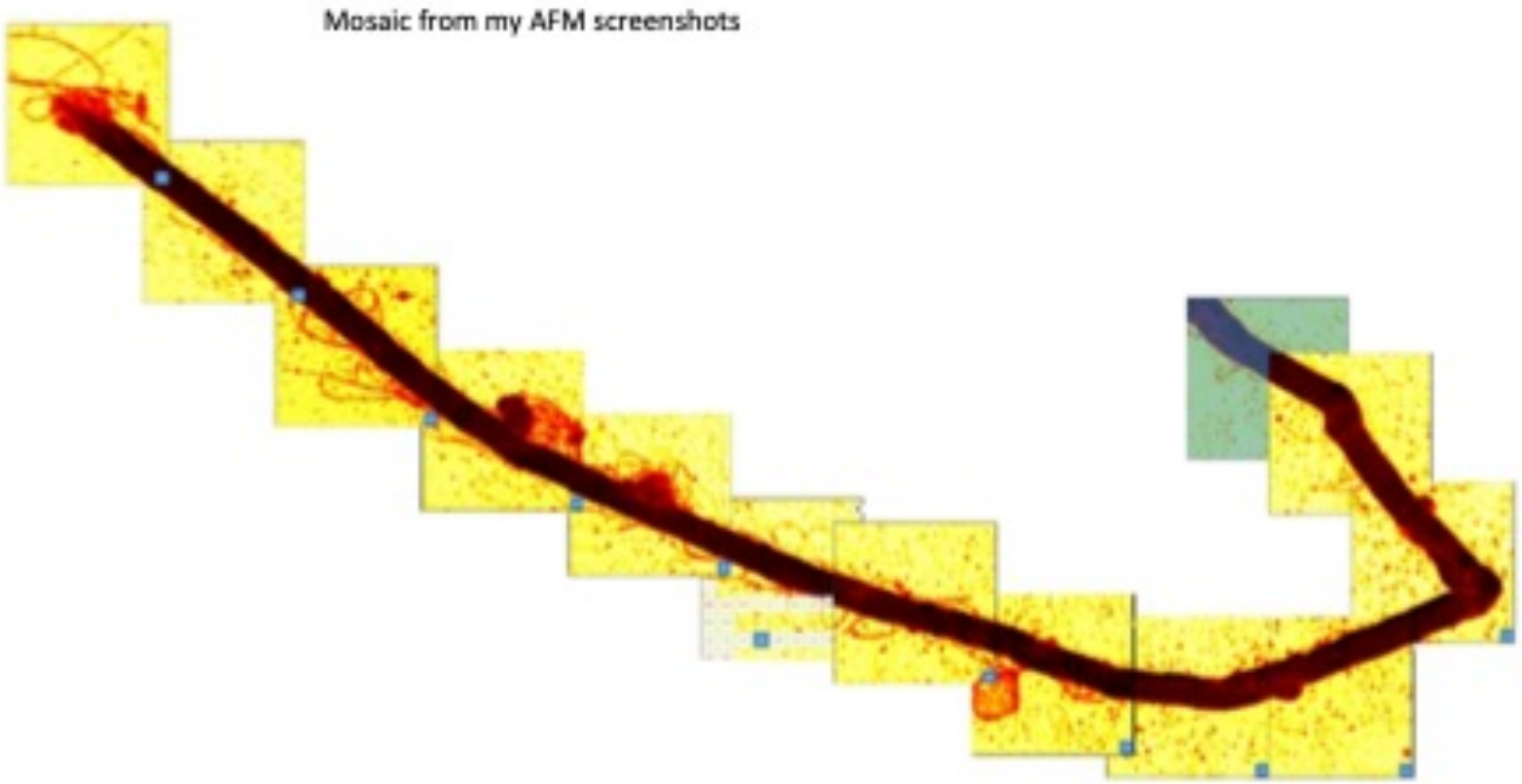
Mosaic from my AFM screenshots

2.11.2 SINS:

This part shows the steps for data acquisition ALS with the SINS instrument. The first page includes photos from the instrument and the second & thirds pages include the screenshots of the SINS software using for data collection. The steps below refer to the numbered locations on these screen captures.

Page 1: First picture: Dr. Bechtel placing the sample underneath the AFM head. He is tuning the position of the mirrors to ensure that the laser beam is directly on the sample.

Second picture: Demonstration of the SINS software. AFM scanning window (left screen), sample view window (middle screen), spectrum collection window (OMNIC software, right screen)

Page 2: This screen shots shows the steps for the AFM scanning steps. It contains several parameters for collecting the Atomic Force Microscope image. In the first scan, a large area (10x10 microns) is scanned to find the target fibril. Once the fibril is located, a smaller area (2x2 or 1x1 micron) is scanned to obtain detailed view. Once the play button is pressed (Box 3), AFM scans are shown on the next window (Box 4).

Box 4: This window is an example of optional AFM views. This AFM image is showing diverse ways of visualizing the sample under the AFM tip.

Box 5: This box shows one of the AFM images in the Box 4. In this window, data points are selected for spectral data acquisition. If an acceptable background was acquired recently, then a few sample spectra may be collected right away. Once the location is selected for data acquisition, and spectrum scan can be started after the parameters for spectrum acquisition can be adjusted in OMNIC window (not shown here, third screen in picture 2, previous page).

Page 3: This window shows the SINS data processing software (custom Fourier Transform analysis package, Berkeley, ALS)

Box 6: This box shows where the raw sample spectrum should be uploaded.

Box 7: This box shows where the reference spectrum should be uploaded.

Box 8: The apodization preference should be adjusted and FT Sample & FT Ref buttons should be pressed for processing.

Box 9: Re, Im & Plot normalized spectra options are selected to process the spectra.

Box 10: The spectrum is saved by pressing save button.


1


2

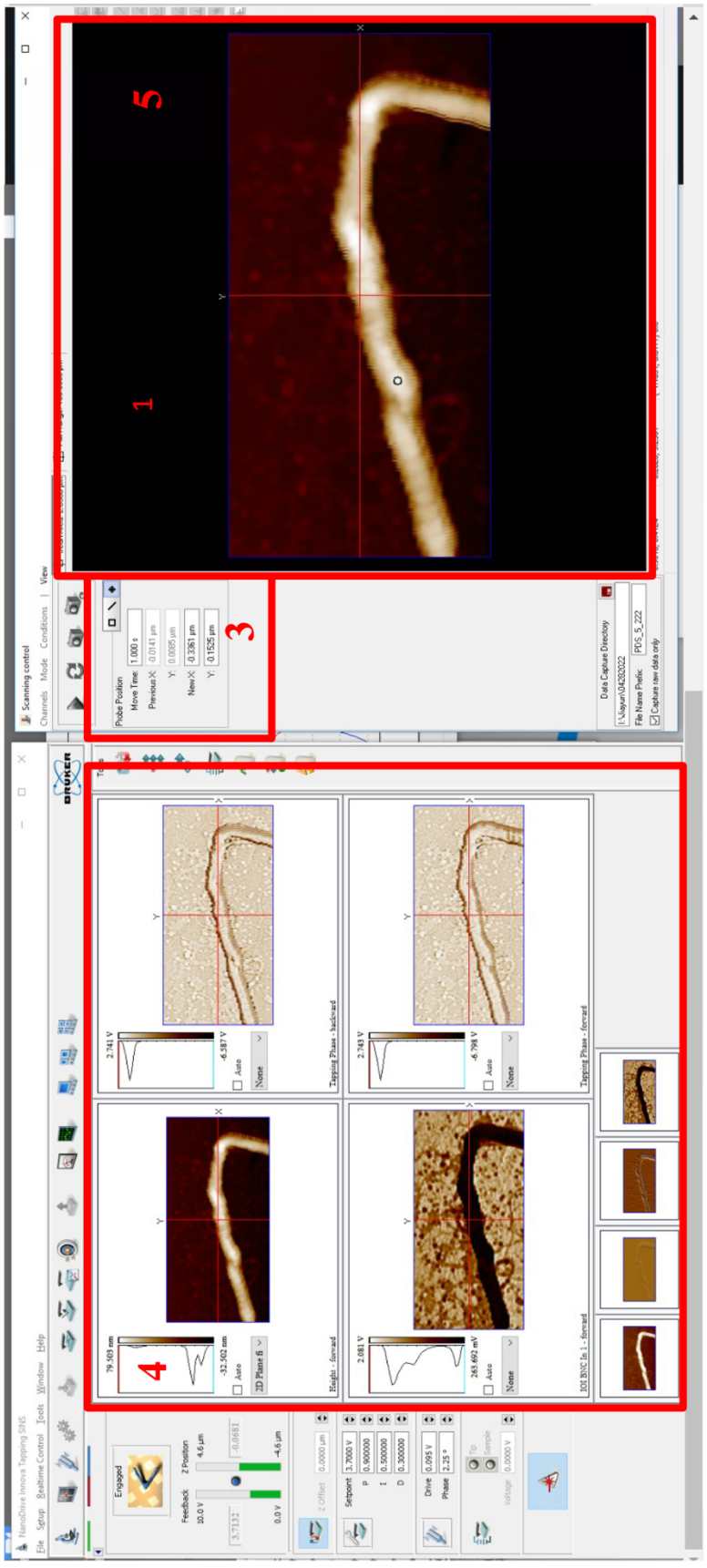
1
2
3
4
5

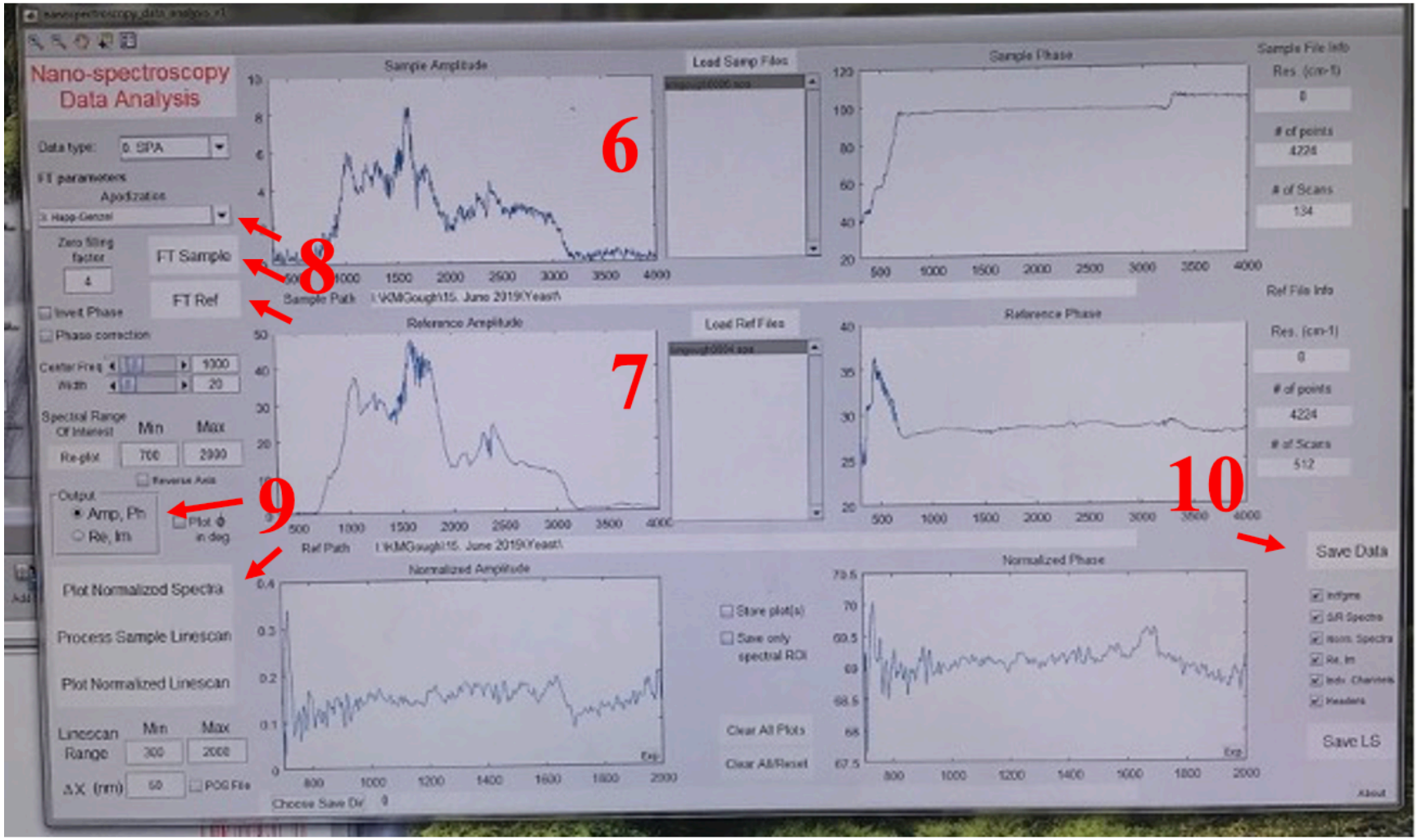
Nano-spectroscopy Data Analysis
Data type:
0: SPA
FT parameters
Apodization
Zero filling factor
FT Sample
FT Ref
Invert Phase
Phase correction
Spectral Range Of Interest
Min
Max
Re-plot
Output
Amp, Ph
Re, Im
Plot ϕ in deg
Plot Normalized Spectra
Process Sample Linescan
Plot Normalized Linescan
Linescan Range
ΔX (nm)
Sample Amplitude
Load Samp Files
Sample Phase
Sample File Info
Sample Path
Reference Amplitude
Load Ref Files
Reference Phase
Ref File Info
Ref Path
Normalized Amplitude
Normalized Phase
Store plot(s)
Save only spectral ROI
Clear All Plots
Clear All/Reset
Save Data
Save LS
6
7
8
9
10

Chapter 3. Orientation Matters: Polarization Dependent IR Spectroscopy of Collagen from Intact Tendon Down to the Single Fibril Level

3.1 Preface

The study in this Chapter of the thesis originated from the study in 2016 (Wiens et al.). For the first time, data were collected with the novel instrument O-PTIR polarization contrast imaging along with Far-field-FTIR with FPA and near-field IR spectroscopy. The results from O-PTIR on control tendons and fibrils were compared with the results from FF-FTIR-FPA and nano-FTIR. Spectra from fibrils showed that Amide I and II bands are narrower in comparison to spectra from tendons and O-PTIR spectra for tendons are similar to FF-FTIR-FPA spectra. This Chapter was published in a special issue of *Molecules* in 2020:

Bakir, G., Girouard, B. E., Wiens, R., Mastel, S., Dillon, E., Kansiz, M., & Gough, K. M. (2020). Orientation Matters: Polarization Dependent IR Spectroscopy of Collagen from Intact Tendon Down to the Single Fibril Level. Molecules, 25(18), 4295.

Members of the Gough group have been working on collagenous tissues for many years, starting in the early 2000s. In 2003, FTIR spectromicroscopy was used to investigate the appearance and distribution of collagenous scars in cardiomyopathic hamsters, some of which had undergone putative drug therapy (Gough et al., 2003). Even though the collagen microdomain distribution was successfully confirmed spectroscopically in the collagen IR fingerprint region (1000-1800 cm^{-1}), the spatial resolution was limited to about 10 microns, as the spectra were acquired as synchrotron raster scan maps. In 2007, the group published a study on collagen scar

formation funding by the Collaborative Health Research Program (Wiens et al., 2007). The synchrotron source was used to increase the spatial resolution, which is essential to understand developing tissues with morphological similarities and drastically different spectroscopic properties. Following that, the Gough group entered a collaborative study on collagen in mechanically damaged tendons with L. Kreplak (Dalhousie University), J. Michael Lee (Dalhousie University), Samuel P. Veres (Saint Mary's University). The first results of FTIR polarization contrast imaging at 1.1 μm on control and mechanically damaged tendons, and the first results of nano-FTIR at about 30 nm on control fibrils were published in 2016 (Wiens et al., 2016). This fundamental study led to the work explained in detail in this Chapter.

Here, we use far-field FTIR with FPA, O-PTIR, and near-field IR techniques, exploiting polarized IR light to show the spectra of intact tendons and fibrils. Tendon samples were prepared from archived frozen tendons by Bakir in the Gough Lab at the University of Manitoba upon receipt from our collaborators. Confirmatory data on intact tendons, not shown in the manuscript, were collected by Bakir at the University of Manitoba using Far-field IR with FPA. The FF-FPA data presented in **Figure 3.1** were originally acquired by Wiens. This archived data was re-analyzed by Bakir, under guidance of Gough to collect suitable data as shown. The same tendon section was sent to Photothermal Spectroscopy Corporation in Santa Barbara, CA, USA, for further analysis with O-PTIR spectroscopy. Intact fibrils isolated from tendons were also prepared in the Gough lab by Bakir and Girouard and sent to Photothermal Spectroscopy Corporation and, for O-PTIR and nano-FTIR analysis, respectively. Kansiz and Dillon collected O-PTIR data with guidance from Bakir and Gough. Mastel collected spectra on fibrils at neaspec GmbH in Munich-Haar, Germany with guidance from Bakir and Gough. Data on those intact fibrils were collected by Bakir and Girouard using the SINS instrument at ALS in Berkeley, CA, USA. All data

processing was performed by Bakir with guidance from Gough in the Gough research lab. Bakir wrote the initial draft of the manuscript including preparation of the figures presented in the manuscript. Dr. Gough provided editing, guidance, and contributions towards the development of the remaining content. All authors made some edits and approved the final manuscript before its submission, and offered advice and edits for the final revision. Preparation of sample and data collection for nano-FTIR is described in more detail in Appendices in Chapter 2.

3.2 Abstract

Infrared (IR) spectroscopy has been used for decades to study collagen in mammalian tissues. While many changes in the spectral profiles appear under polarized IR light, the absorption bands are naturally broad because of tissue heterogeneity. A better understanding of the spectra of ordered collagen will aid in the evaluation of disorder in damaged collagen and in scar tissue. To that end, collagen spectra have been acquired with polarized far field (FF) Fourier Transform Infrared FTIR imaging with a Focal Plane Array detector, with the relatively new method of FF optical photothermal IR (O-PTIR), and with nano-FTIR spectroscopy based on scattering-type scanning near-field optical microscopy (s-SNOM). The FF methods were applied to sections of intact tendon with fibers aligned parallel and perpendicular to the polarized light. The O-PTIR and nano-FTIR methods were applied to individual fibrils of 100-500 nm diameter, yielding the first confirmatory and complementary results on a biopolymer. We observed that the Amide I and II bands from fibrils were narrower than those from intact tendon, and that both relative intensities and band shapes were altered. These spectra represent reliable profiles for normal collagen type I

fibrils of this dimension, under polarized IR light, and can serve as a benchmark for the study of collagenous tissues.

3.3 Introduction

The infrared (IR) spectrum of type I collagen has been studied for decades(Badger & Pullin, 1954; Cheheltani et al., 2012; Eklouh-Molinier et al., 2015; Fraser, 1950; Lazarev et al., 1985a; Payne & Veis, 1988; Wiens et al., 2016). The importance of collagen in the health and maintenance of the human body is extensive; the hierarchical structure and radial symmetry of collagen render it a suitable target for study with polarized IR light, for example: Type I collagen (Badger & Pullin, 1954; Eklouh-Molinier et al., 2015; Fraser, 1950; Sellaro et al., 2007; Wiens et al., 2016) and Type II collagen (Camacho et al., 2001). The dichroic behavior of ordered collagen fibrils was first demonstrated with IR spectro-microscopy nearly 70 years ago (Fraser, 1950). We have studied collagen in scar tissue (Gough et al., 2003; Wiens et al., 2007) and in mechanically damaged tendon (Wiens et al., 2016), where we exploited IR polarization imaging to probe the degree of disorder in the damaged tissue.

A limitation to the IR spectroscopic analyses of collagen has been the lack of definition of the spectral profile that constitutes a molecular level of order in normal control tendon and fibrils. Typically, the IR polarization contrast is defined chiefly by changes in the *relative* intensity of the Amide I (primarily carbonyl stretch) and Amide II (primarily C-N backbone stretch with some C-N-H angle bend) vibrational bands. In fact, numerous bands in the complicated spectrum of highly ordered collagen type I respond differently under polarized infrared light (Badger & Pullin, 1954; Bi et al., 2005; Camacho et al., 2001; Fraser, 1950; Wiens et al., 2016). Our previous work was primarily based on far field Fourier Transform IR (FF-FTIR) imaging with focal plane array (FPA)

detection, which is subject to the usual Rayleigh criterion resolution limits for λ = ~7 μm wavelength, corresponding to the main protein IR absorbance bands, Amide I and II (Wiens et al., 2016). We then began using nanoscale FTIR (nano-FTIR) spectroscopy employing the scattering-type scanning near-field optical microscopy (s-SNOM) method(Amenabar et al., 2013; Bechtel et al., 2014; Huth et al., 2012; Mastel et al., 2015; Taubner et al., 2004), wherein the diffraction limit is circumvented and IR spectra may be obtained with a spatial resolution of ~20 nm, far below the wavelength of the IR radiation (typically 5-10 μm). Another complementary method is Optical Photothermal IR (O-PTIR) imaging and spectroscopy (Baden et al., 2020; Klementieva et al., 2020; Reffner, 2018)**,** a relatively new far-field technique that opens a new window onto the study of collagen, both as intact tissue and as fibrils, with IR wavelength-independent resolution of better than 500 nm.

In this paper, we seek a better understanding of the absolute variation in spectra of ordered collagen, as this can improve the evaluation of disorder in damaged collagen in the future. To this end, we employed multiple techniques that provide a variety of polarized IR sample illumination and spatial resolutions to investigate the dependence of collagen IR spectra on these parameters. Polarized IR spectra and images of intact, mechanically aligned tendon were obtained with FF-FTIR equipped with focal plane array (FPA) detection and with O-PTIR. To polarize the IR radiation in the FF-FTIR measurements, we inserted a polarizer in the path of the IR beam, after passage through the sample; the lasers employed in O-PTIR are inherently linearly polarized. It was also possible to obtain spectra of control, unstretched fibrils with nano-FTIR spectroscopy, and of similar fibrils with a quantum cascade laser (QCL) oriented with (parallel) and across (perpendicular) the fibril direction by O-PTIR. The nano-FTIR spectra are necessarily polarized with respect to the probe tip axis, and thus yield spectra perpendicular to the fibril direction only.

The results from intact tendon (FF-FTIR and O-PTIR) are contrasted with those from sub-micron fibrils (O-PTIR and nano-FTIR), in an effort to obtain a clearer understanding of the variations observed and their relation to internal structural order.

3.4 Results

Infrared spectra have been acquired from intact bovine positional tendon and from fibrils extracted from these tendons. The intent is to compare the spectral profiles that appear under conditions of polarized IR illumination using diverse instrumental approaches. The sample preparation for intact tendon and fibrils should leave the tendon free of possible contamination whether phosphate buffer solution (PBS) or optimal cutting temperature (OCT) cryoprotectant (see Methods). In one case only (O-PTIR spectra of fibrils), some OCT was observed; this was easily removed by spectral subtraction.

3.4.1 Far Field IR Spectroscopy of Intact Tendon with Polarized Light

IR Polarization Contrast FTIR Microscopy with Focal Plane Array detection

In the course of our study on mechanically damaged tendons (Wiens et al., 2016), we acquired a multitude of polarization contrast images of tendon sections. Here, we have drawn on our library of data to present spectra representative of collagen that is intact, and undamaged (**Figure 3.1**). In each case, an FTIR FPA image comprising several thousands of spectra, was examined, and some 20 spectra extracted that met the criteria of similar high-quality signal-to-noise ratio (SNR), level baseline and absence of scattering artifacts. In addition, the spectra were selected only from regions of the image where the polarization contrast and visible record showed

that the normally crimped tendon had been drawn straight, without rupture or introduction of kinks (Wiens et al., 2016).

The spectra exhibit the expected profiles of Type I collagen, with a slightly asymmetric Amide I, and profound differences in the relative intensities of most bands under IR light polarized parallel (**Figure 3.1**, upper set) or perpendicular (**Figure 3.1**, lower set) to the orientation of the fibers in the tendon. Samples were imaged either with a single orientation under two different polarizer settings (0° and 90°) relative to the fiber orientation, or with polarizer set at 90° and sample rotated by 90°, to test for any instrumental bias, as shown in the white light images. Results were consistent regardless of procedure.

We observe a slight narrowing of the full width at half maximum of the Amide I in the perpendicular orientation, 60(SD=2) cm^{-1}, compared to parallel, 74(SD=3) cm^{-1}, which is in part due to the contribution of the much stronger Amide II band in the parallel orientation. Rather than attempt to quantify these variations at this stage, we next compare the results with those from other methodologies that yield data from smaller voxels.

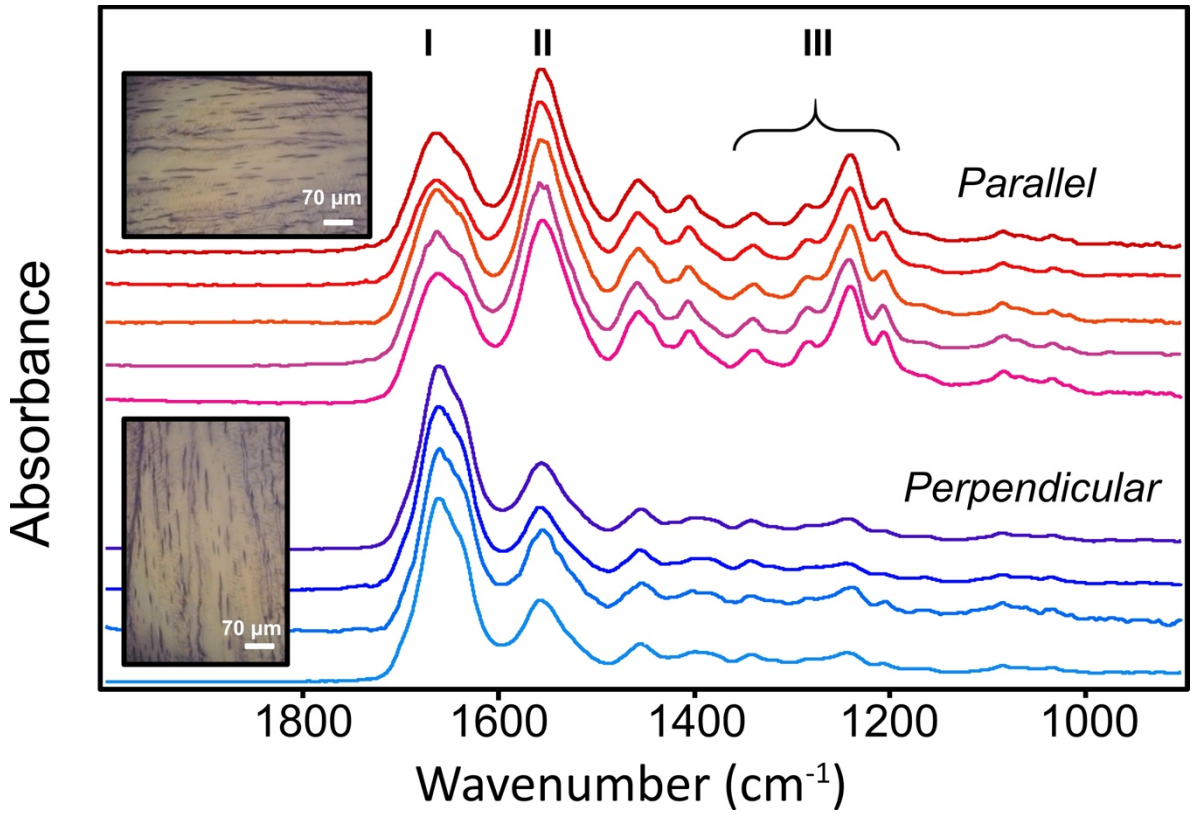

Figure 3.1 Far-field Fourier transform IR (FF-FTIR) spectra spectra of intact tendon on BaF_2 from mosaic images obtained with focal plane array (FPA) detection, labelled to show Amide I, II and III regions. Each spectrum is derived from a different mosaic, and is an average of about 20 spectra selected from the most oriented region in the field of view. Visible images show typical appearance of straightened tendon, imaged with same polarizer setting (90°) aligned with or rotated to be perpendicular to the polarizer. Scale bar = 70 µm.

IR Polarization Contrast Spectroscopy with Optical-Photothermal IR (O-PTIR) Detection

Vibrational spectra were collected with the mIRage O-PTIR microscope (Photothermal Spectroscopy Corp.) from single points (~500 nm) in a region of oriented tissue in one of the sections mounted on a CaF_2 window and shown in **Figure 3.1**. This O-PTIR operates on the principle of photothermal detection (Baden et al., 2020; Klementieva et al., 2020; Reffner, 2018), in which an IR quantum cascade laser (QCL) excites the sample's molecular vibrations in the

spectral range of 1800-900 cm^{-1}; the resultant photothermal effect is detected via a short wavelength probe laser. As the IR lasers are highly linearly polarized, the spectra are expected to be comparable to a great extent with those obtained from the FTIR microscope with IR polarizer. In order to obtain parallel and perpendicular spectra, the samples were oriented to be aligned with, or rotated to be perpendicular to, the laser polarization. The results for tendon on CaF_2 and on glass are shown in **Figure 3.2**.

The spectra in **Figure 3.2**A and 2B show that the high contrast achieved with the inherent laser polarization yields spectra that are very similar to those obtained from the first experiments with FTIR FPA and polarizer. Similar results were obtained for the serial section mounted on a glass microscope slide, and spectra were obtained with equally good SNR quality (**Figure 3.2**B).

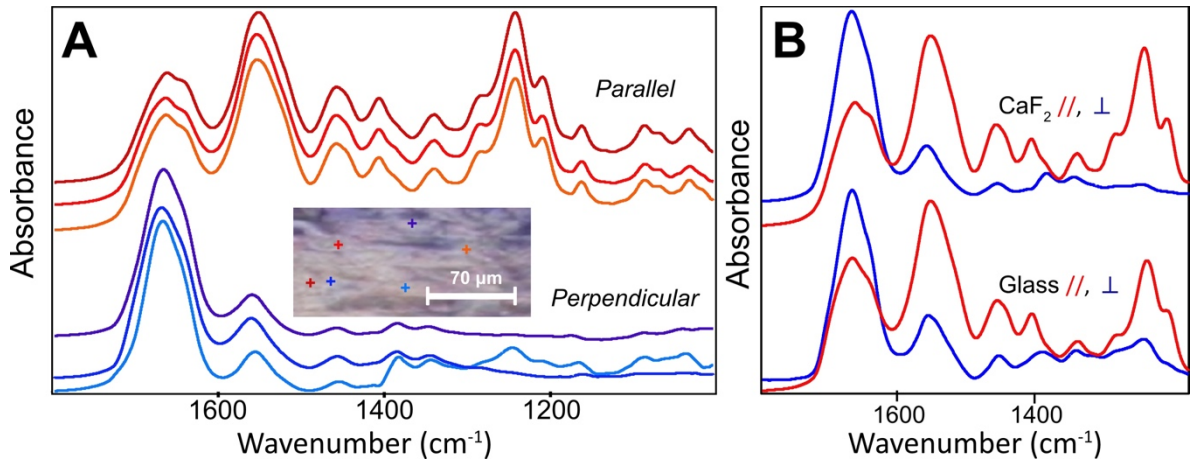

Figure 3.2 Optical photothermal IR (O-PTIR) spectra spectra from intact tendon, from ~500 nm measurement spots. (A) individual spectra obtained from the two orientations of a section mounted on a CaF2 window, relative to the linearly polarized quantum cascade laser (QCL). Inserted visual image shows the 6 locations, all of which lie within the region imaged with FTIR FPA; scale bar = 70 µm. Coloured + correspond to spectral colours. (B) comparison of spectra obtained from CaF2 (top) and Glass (bottom) substrates in parallel and perpendicular orientations to linearly polarized QCL.

3.4.2 Far-Field IR Spectra of Collagen Fibrils with Polarized Light

It was not possible to obtain a spectrum from a single fibril with the FF-FTIR FPA, despite a very high accumulation of scans (2048 for background and 512 for sample) with the high magnitude optics engaged, even without the polarizer in place. Inclusion of the polarizer dropped the SNR for the FF-FTIR FPA by more than one half. This result is not surprising, given that the fibril dimension is an order of magnitude below the diffraction limit of FF-FTIR and there is very little material. Thus, this approach could not reasonably be used on single fibrils. Spectra of individual fibrils, extracted from control tendon in the same manner as described in our previous work (Wiens et al., 2016), were successfully obtained by O-PTIR and by nano-FTIR spectroscopy instruments

IR Polarization Contrast Spectroscopy of Isolated Fibrils with O-PTIR

O-PTIR spectra were obtained from numerous points along a control fibril prepared from a tendon segment that was not subjected to mechanical damage, (**Figure 3.3**). Once identified, the same fibril was examined with the orientation horizontal (parallel) and vertical (perpendicular) to the IR laser polarization, by rotating the sample on the stage, as was done for the intact tendon. Traces of OCT medium were found in all spectra. The fibrils had been extracted from a piece of tendon that had originally been encased in OCT medium and, evidently, removal of this medium by several sequential washings in ultrapure water was insufficient to eliminate it. A single FF-FTIR FPA image of the droplet's centre was taken later (data not shown), and confirmed the contaminant identity as OCT. The spectra in **Figure 3.3** were taken furthest from the concentrated OCT region and were corrected by subtraction of the OCT spectrum. Signature bands of collagen from 1400 to 900 cm^{-1} were evident, but obscured by uneven OCT contamination. Fortunately,

OCT does not absorb across the Amide I and II region, allowing a clean window onto those modes. The O-PTIR SNR was estimated to be 40 for parallel and 70 for perpendicular orientations based on the signal maximum for the strongest band and the peak to peak noise between 1795 to 1750 cm^{-1} in each case.

The Amide I and II profiles are much as expected: in the perpendicular orientation the Amide I dominates, while the Amide II is strongest in the parallel orientation, as seen in intact tendon. Both bands were narrower than those recorded from intact tendon; this observation is discussed below.

The fibril was imaged with O-PTIR at several single frequencies, to get a confirmatory estimate of the apparent physical width. The intense red-yellow band from the single frequency image recorded at 1655 cm^{-1} in perpendicular orientation (**Figure 3.3**, right side) shows this fibril to be no more than 500 nm across, based on the line profile of intensity across the fibril (data not shown). This dimension qualifies the target as a true fibril, and is comparable to the 300 nm fibril examined for the first IR s-SNOM experiments (Wiens et al., 2016).

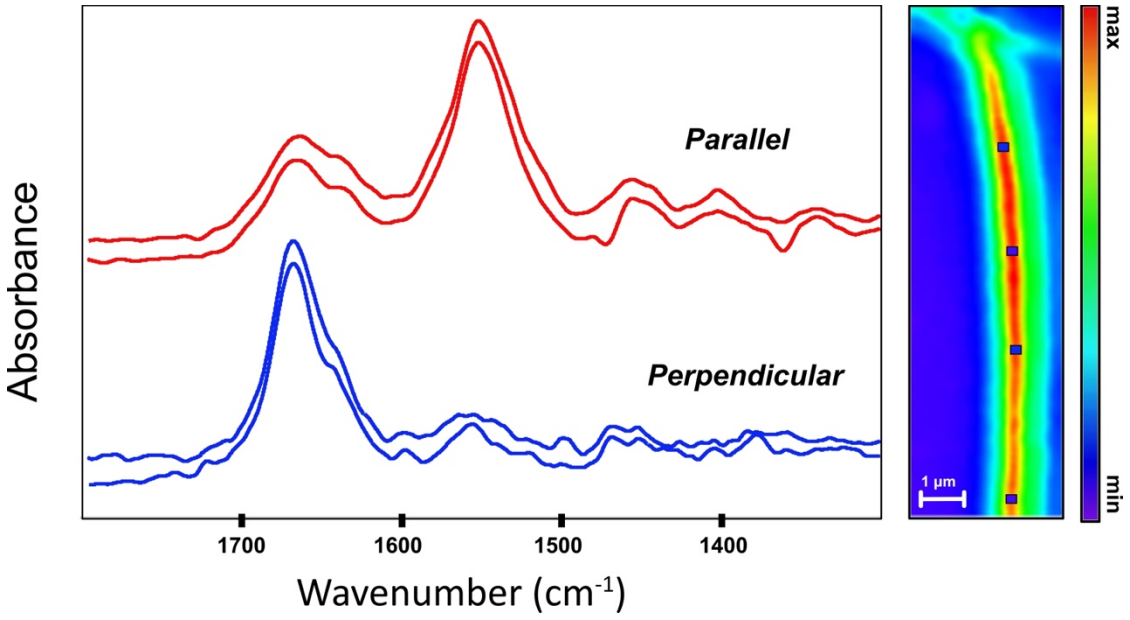

Figure 3.3 Spectra obtained with O-PTIR from control tendon fibrils on CaF_2 window. Top spectra (red) obtained with fibril parallel to laser polarization; bottom spectra, sample rotated by 90°. Single frequency image at right recorded at 1655 cm^{-1} in perpendicular orientation. Squares denote locations at which some of the spectra were acquired. Scale bar = 1 µm.

IR Polarization Contrast Spectroscopy with Nano-FTIR Spectroscopy Detection

As part of an on-going study, we have been collecting nano-FTIR spectra on control and mechanically damaged collagen fibrils at the Advanced Light Source, LBNL, Berkeley CA, USA. One of the motivations for the present analysis of control fibrils is to gain a clearer understanding of the differences between control and damaged fibrils. Earlier studies showed that the nano-FTIR method favors absorption bands that are aligned with the Atomic Force Microscopy (AFM) tip (Wiens et al., 2016). This effect, which was expected (Amenabar et al., 2013), arises from the tip-sample polarization of the electric field; however, prevents acquisition of spectra parallel to a fibril lying on the AuSi substrate. We plan to exploit this feature to identify molecular scale changes in

damaged fibrils. Spectra obtained with nano-FTIR spectroscopy, from control fibrils that were not subjected to mechanical damage, are shown in **Figure 3.4**.

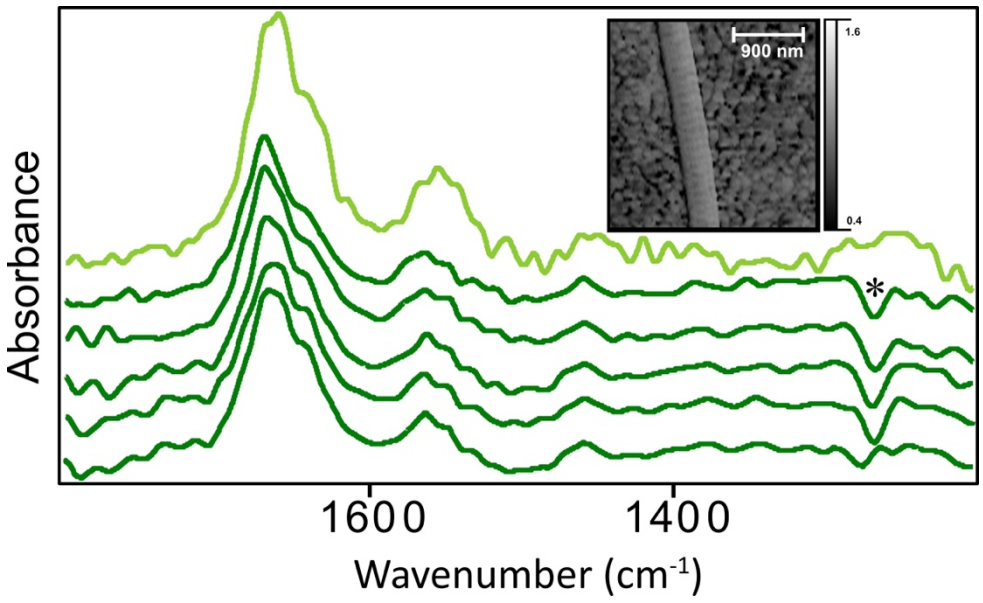

Figure 3.4 Nano-FTIR spectra of control tendon fibrils. Top light green spectrum is average of 19 spectra acquired synchrotron light at the Advanced Light Source. Bottom five spectra (dark green) were acquired with a neaSNOM microscope (neaspec GmbH, Munich-Haar, Germany). Asterisk (*) at 1265 cm^{-1} shows negative peak due to polydimethylsiloxane (PDMS) contamination of the AFM tip. Inserted AFM image shows a typical control fibril, lying on sputtered Au surface, with D-banding; scale bar = 900 nm.

The AFM image in **Figure 3.4** illustrates the normal D-banding in an isolated control fibril, one of the series that were examined. Five spectra were obtained with laser illumination (neaspec GmbH, Munich-Haar, Germany) at points on a fibril previously examined at BL 2.4 Advanced Light Source (ALS) with the neaSNOM microscope and synchrotron illumination. The SNR for spectra obtained at ALS is always weaker than that obtained with nano-FTIR lasers. A total of 19 single point spectra taken from control fibrils at ALS were summed to give the ALS spectrum shown here. The negative polydimethylsiloxane (PDMS) band at 1265 cm^{-1} is noted in some of

the spectra in **Figure 3.4** (see Methods). Its presence interferes with the detection of the Amide III series of bands (1337, 1284, 1240 and 1204 cm^{-1}) but these would not be prominent in the perpendicular orientation.

Significantly, nano-FTIR spectroscopy allows us to record very good spectra on a single fibril; the signal quality is slightly lower due to the small probing volume. For nano-FTIR spectroscopy, and IR s-SNOM in general, the volume is estimated as $(\sim 20\ nm)^3$, compared to other techniques, $(500\ nm)^3$ for FF O-PTIR on fibrils, $(500\ nm)^2 \times (2$ to $3\ \mu m)$ for FF O-PTIR on intact tissue, and $\sim 3\ \mu m \times 3\ \mu m \times 5\ \mu m$ or $\sim 45\ \mu m^3$ for conventional FF-FTIR FPA spectroscopy, adjusted for the IR wavelengths of the Amide I and II bands and tissue depth ~5 μm.

3.4.3 Comparison of Spectra from All Methods

Figure 3.5 summarizes the data above. All spectra were collected as a single average for each orientation and instrument.

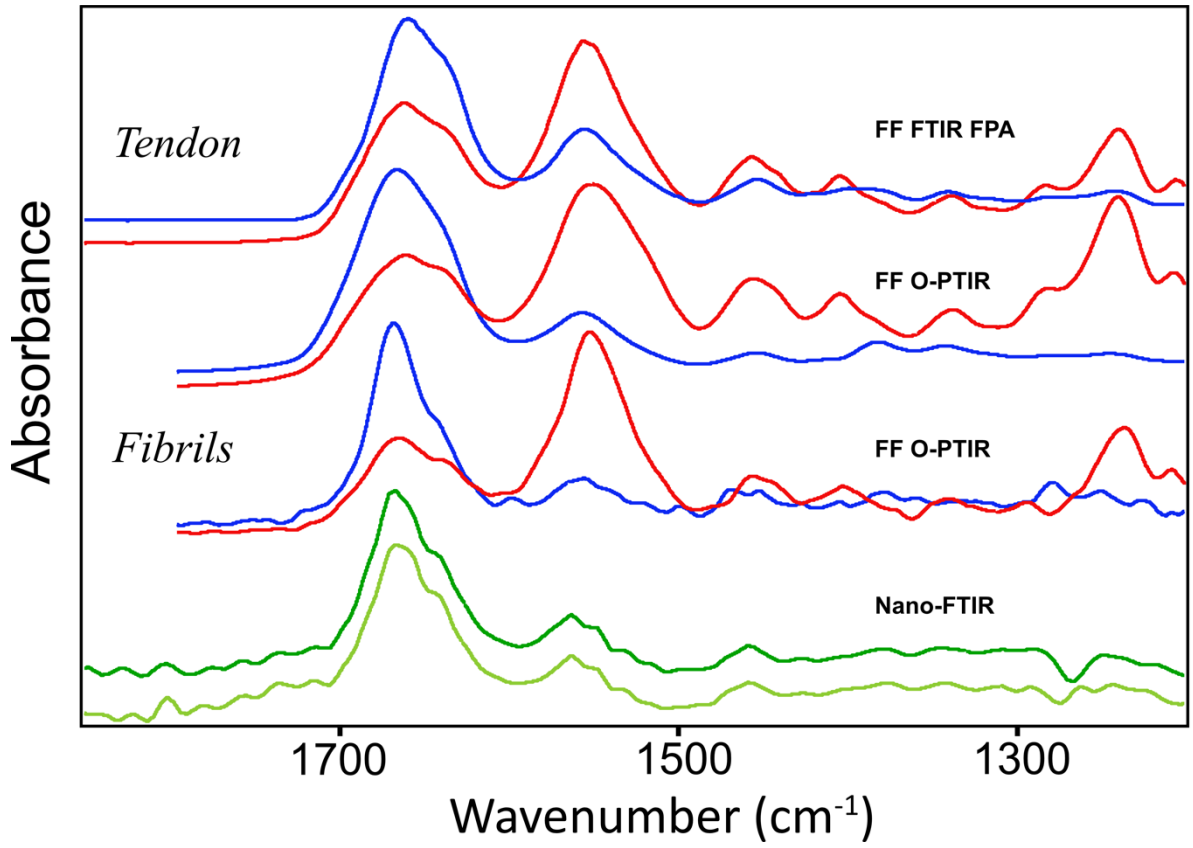

Figure 3.5 Averaged spectra from each experimental procedure, offset for clarity. As in other figures, all spectra with polarization parallel to fiber or fibril direction are shown in red; perpendicular are blue. Intact tendon spectra from FF-FTIR FPA and O-PTIR are sums of spectra appearing in Figure 3.1-3. The nano-FTIR spectra at the bottom represent sums of three separate experiments, two with lasers (dark green) and the sum of 19 spectra from ALS, bottom-most spectrum (light green).

3.5 Discussion

Collagen molecules in a positional tendon are aligned in an inherently organized, hierarchical manner, thus tendon is eminently suitable for analysis with polarized IR light (Fraser, 1950). While polarization studies with other methods are common, few have used polarized IR spectroscopy (Badger & Pullin, 1954; Bi et al., 2005; Camacho et al., 2001; Fraser, 1950; Wiens et al., 2016). IR wavelength-independent spatial resolution FF O-PTIR and nano-FTIR

technologies are rapidly advancing our ability to collect IR spectra at spatial resolutions below the IR diffraction limit. Our motivation in this work has been to get deeper understanding of what the different experimental approaches can reveal for Type I collagen, in order that we can better evaluate mechanically damaged tissue and ordered/disordered scar tissue, where the organization is significantly altered.

Early IR polarization studies of collagen quickly addressed the complexity of dichroism in collagen (Badger & Pullin, 1954; Lazarev et al., 1985a), with recognition that the direction of the change of the molecular dipole moment in the Amide modes would not be precisely parallel to the orientation of the bonds. Some band assignments have been achieved through analysis of synthetic biopolymer mimics (Lazarev et al., 1978) and temperature-dependent studies (Payne & Veis, 1988). The Amide I mode is generally referred to as a C=O stretch, but vibrational energy and alignment of the dipole moment change depend on the amide orientation. The Amide II is mostly due to C-N stretch with some C-N-H angle bend, but the fundamental mode could well be nearly perpendicular to the direction of the N-H bond. The presence of other amino acid residues, and unknown quantities of water of hydration, lead to further unresolvable spectral contributions even in pure collagen.

The hierarchical organizational structures in tendons are loosely classified by their diameter as fiber (2000-500 nm), fibril (100-500 nm) and sub-fibril (<100 nm) diameter, while the diameter of an individual collagen triple helical molecule is about 1.5 nm. Given the mode of self-assembly, it is not realistic to define these more precisely (Kannus, 2000; Orgel et al., 2006). As we showed previously (Wiens et al., 2016), actual rupture results in a mixture of orientations on a micron spatial scale, producing spectra that are intermediate between the primarily parallel and perpendicular extremes. Some variation in orientation must exist simply because of tissue depth,

as those tendons were cryosectioned at 5 and 8 μm thickness. Intact tendons contain additional non-collagenous components that help to maintain the gliding functions, as well as cells, such as fibroblasts and synovial cells (Orgel et al., 2006). The absence of a lipid carbonyl band at 1735-1740 cm^{-1} and of the symmetric CH_2 stretch band (data not shown) shows that we are not detecting any significant amounts of cellular material. These bands were detected in some spectra of intact tendon, and for this reason were not selected for the data presented here.

The spectral information shown in **Figure 3.1** has spatial resolution that is IR wavelength dependent. The volume probed with the FF-FTIR FPA microscope and high magnification option is at best ~ 1.1 μm × 1.1 μm × 5 μm (Reddy et al., 2013) when applied to bands at short wavelengths, such as 3 μm for NH and CH stretch modes. For the Amide bands considered here, the Rayleigh criterion spatial resolution is ~4 μm, with 1.1 μm pixel size oversampling (Findlay et al., 2015; Reddy et al., 2013; Stelzer, 1998), and the probed volumes are estimated to be on the order of 3 μm × 3 μm × 5 μm. In comparison with the fibril spectra below, the Amide bands are relatively broad, as can be expected for the heterogeneity present, even though the tendons had been stretched sufficiently to eliminate normal crimping. The spectra show the expected profiles under parallel and perpendicular polarization, wherein the distinct polarization contrast permits assessment of relative tissue organization at the micron length scale.

The application of O-PTIR for analysis of oriented materials was recently demonstrated for a cross-section of a commercial plastic bottle (Baden et al., 2020). The plastic wall was 350 μm thick, thus it was possible to obtain polarized spectra with an estimated pixel resolution of 500 nm across the wall thickness. Linear dichroism was observed in the spectra for polyethylene terephthalate PET backbone methylene wagging modes, in contrast to C=O stretch modes, which

were anticipated to be mainly perpendicular to the chain direction. Here, we present the first example of O-PTIR polarized spectroscopy of a biopolymer, collagen.

From the FF O-PTIR spectra of intact tendon (Figure 3.2A), we can conclude that the polarization of the lasers in the mIRage microscope give results that are essentially equivalent to those obtained with a thermal source FF-FTIR FPA and IR polarizer. The SNR is excellent, particularly on noting that, for single points at least, the data collection time was 30 s under our operating conditions. The band profiles reveal further differences in the Amide bands. The low energy shoulder in the Amide I under parallel polarized light is even more clearly defined with O-PTIR. It is still apparent, though greatly diminished, in the perpendicular orientation. The depth penetration of the O-PTIR spectra is not precisely definable, though presumably a few microns, and possibly the entire depth of these dried sections as it depends on the material probed; however; the spot size is ~500 nm and the spectrum must be more localized than that of FF-FTIR FPA.

Interestingly, relative intensities of the Amide I and II bands in O-PTIR differed slightly more than was observed with the FPA, as did the contrasting profiles within the Amide I. This is possibly due to a higher IR polarization contrast with the QCL, though this seems unlikely, as the IR polarizer is very efficient. Instead, the higher spatial resolution afforded by O-PTIR may probe a more purely oriented local section of the tendon fibrils. The FF-FTIR gives an average of the chemistry from within a few to several micron diameter voxel, while with better spatial resolution, the submicron heterogeneity may be clearer.

The O-PTIR signal intensity was not dependent on the substrate, as numerically comparable results were obtained from the section on glass compared to that on CaF_2, under the same measurement conditions and sample orientation (Figure 3.2B). Point to point variation was no greater than that typically observed under FF-FTIR, and is ascribed to slight variations in tissue

thickness or condition. The ability to measure samples on standard glass slides, without the loss of signal below 1600 cm^{-1} as occurs with transmission FTIR on salt windows, is another key advantage of using O-PTIR. The sample may be stained after spectra have been recorded, the glass substrate is inexpensive and is a normal part of histology workflow.

The profiles for the Amide bands of fibrils obtained with O-PTIR (**Figure 3.3**) are similar to those of intact tendon obtained with O-PTIR (**Figure 3.2**) but with cleaner and more pronounced differences. The spectra parallel to the fibril length exhibit a strong Amide I shoulder at lower energy that is nearly absent in the perpendicular spectrum. The increased intensity of the main Amide I absorbance, centered around 1655-1660 cm^{-1} could be masking the shoulder but relative intensities of individual bands under different polarizations cannot be ascertained.

Owing to the radial symmetry of the collagen fibril, and the high polarization in the z-direction (parallel to AFM tip), the nano-FTIR spectra of collagen fibrils are expected to be equivalent to spectra acquired perpendicular to the fibril direction, in the sample x-y plane. Spectra in **Figure 3.4** are very similar to those observed in our previous work (Wiens et al., 2016), whether acquired with synchrotron IR light, or the nano-FTIR laser system.

Direct comparison of the averaged spectra from intact tendon and from fibrils, from all experimental techniques (**Figure 3.5**), shows clearly that the Amide bands from intact tendon spectra are considerably broader than those obtained from fibrils, regardless of whether intact tissue spectra were obtained by FF-FTIR FPA or FF O-PTIR. The relative intensity of Amide II to Amide I band drops from about 1.3 (parallel) to 0.3 (perpendicular).

Owing to the sample dimension and sub-fibril heterogeneity (Orgel et al., 2006), it is not possible able to rationally resolve the multiple contributions within either band. It is important to note that, historically, procedures such as curve-fitting, second derivatization (2ndD), and Fourier

Self-Deconvolution (FSD), have sometimes been applied to spectra in an effort to resolve overlapping bands (Payne & Veis, 1988). We applied FSD and 2ndD to the spectra of intact tissue obtained with FF-FTIR FPA and FF O-PTIR. FSD parameters are typically left to the operator choice; we used a bandwidth of 16 cm^{-1} and enhancement factor of 2. The pseudo-deconvolved spectra bore little resemblance to the fibril spectra acquired with sub-micron techniques: relative intensities did not match, multiplets appeared at wavelengths where no bands appeared in the fibril spectra (data not shown). It might be argued that these bands could reflect multiple oblique fibril orientations within the tissue thickness, but these are not unique solutions and cannot provide the information that we have sought. There can be no substitute for data acquired at genuinely wavelength-independent submicron spatial resolution.

Comparisons among all spectra show that Amide bands taken with IR light parallel or perpendicular to the control fibril direction are much narrower than those from intact tendon. This indicates that the fibril target is more uniform, whether assessed at ~500 nm (O-PTIR) or 200 nm (nano-FTIR spectroscopy). These dimensions represent the typical range of the "fibril" width; thus, it is very satisfying to see the similarity.

The Amide I band is sharply narrowed in the perpendicular polarized spectra from either method. The principal contribution is from the higher energy band centered at ~1660 cm^{-1}. The ratio of the Amide II to Amide I integrated band areas is still about 0.3; however, this now reflects the dominant higher energy component. The lower energy shoulder at 1635 cm^{-1} is generally thought to arise from the glycine C=O, which points outward from the triple helix, and is most available for H-bonding with water (Lazarev et al., 1985b; Payne & Veis, 1988). Such H-bonding would weaken the C=O bond and lower the vibrational energy. If so, then the spectra can be interpreted to mean that this carbonyl is generally aligned more with the fibril direction. Only the

O-PTIR technique allows for spectra with polarization *parallel* to the direction of an individual fibril. The intensity of the 1660 cm^{-1} band drops significantly, while that of the lower energy band at 1635 cm^{-1} remains distinct. This observation is in keeping with the perpendicular spectra, in that a band more aligned with the fibril direction (1635 cm^{-1}) should remain strong when the polarization is rotated to the parallel. The triple helix axis is tilted by up to 15 degrees with respect to the microfibril axis (bundle of five collagen triple helices where the molecules are axially quarter-staggered), based on X-ray scattering data on tendons (Orgel et al., 2006). Given the dimensions of the fibrils, we must assume this amount of variation is present. The absence of a lipid carbonyl band at 1735-1740 cm^{-1} region confirms that there is little, if any, cellular debris remaining, and that these are spectra of clean, normal D-banded, undamaged collagen fibrils. The O-PTIR and nano-FTIR spectra of fibrils give confirmatory results for spectra with polarization perpendicular to the fibril axis, while the O-PTIR also enables the complementary result for polarization parallel to the fibril axis. We conclude that these spectra represent reliable profiles for control collagen type I fibrils of this dimension, under polarized IR light, and will serve as benchmark references for future studies.

3.6 Materials and Methods

Tendon samples came from a series described previously (Wiens et al., 2016); preparation is summarized briefly here. Tendons were dissected from the tails of young adult steers killed for food, and immediately stored at 4°C in phosphate buffered saline (PBS) containing 1% antibiotic/antimycotic solution (product A5955, Sigma-Aldrich, Oakville, ON, Canada). Prior to mechanical damage procedure, a 15-mm-long sample was removed from each tendon to serve as an unloaded control. Using a servo-hydraulic materials testing system, the remainder of each

tendon was subjected to 5 cycles of sub-rupture overload at a strain rate of 1%/s, as described previously (Veres et al., 2013; Wiens et al., 2016). Control and stretched tendon segments, approximately 10 mm long by 4 mm diameter, were stored at room temperature for 24 hours in PBS containing 1% antibiotic/antimycotic solution and 1% protease inhibitor (product S8820, Sigma-Aldrich, Oakville, ON, Canada); shipped overnight to the University of Manitoba, where they were immediately removed from PBS medium, covered with OCT [Sakura Finetek Inc. USA], frozen in isopentane-cooled in liquid N_2, and stored at -80°C. Cryosections were cut to 5 or 8 μm thickness at -21°C, and mounted on CaF_2 or BaF_2 salt windows, as well as on glass microscope slides (for O-PTIR).

For fibril analyses, a thawed control tendon segment was washed as follows: the thawed segment was rinsed in ultra-pure water to remove the majority of the OCT; it was then transferred to a 1.5 mL Eppendorf with ultra-pure water, soaked for 20 min, rinsed again and transferred to a fresh Eppendorf.; this was repeated 6 times. The rinsed segment was dissected further using tweezers and a fine tipped glass rod in 1 mL of ultra-pure water until the mixture appeared cloudy, releasing many suitable fibrils (Baldwin et al., 2014). Droplets of the suspensions were deposited on CaF_2 salt windows or on 1 cm^2 gold-coated silicon wafers for O-PTIR and nano-FTIR analysis, respectively.

For FF-FTIR, tissue sections of stretched, sub-rupture tendon were imaged with an Agilent Cary 670 interferometer and 620 IR microscope, equipped with a 64×64 Focal Plane Array Mercury Cadmium Telluride (MCT) detector. High magnification optics (1.1 μm ×1.1 μm pixels, 15x 0.62NA objective) (Findlay et al., 2015) were used to explore collagen orientation within intact tissue. All spectra were acquired as averages of 128 scans, 4 cm^{-1} spectral resolution, ratioed against a background of 512 scans acquired on a clean region of the salt window. Spectral

acquisition and data processing were performed with the ResolutionsPro™ FTIR spectroscopy software (Ver. 5.3.01964, Agilent Technologies Inc., Santa Clara, CA, USA).

O-PTIR spectra and images of tissue and of fibrils were collected on a mIRage+R™ Infrared and Raman microscope (Photothermal Spectroscopy Corp, Santa Barbara, CA, USA). Samples were presented on CaF_2 windows and glass microscope slides, and measured in reflectance mode. The system was equipped with a pulsed, broadly tunable high power QCL covering 1800-800 cm^{-1} as the pump beam (IR source) and a 532 nm continuous wave (CW) probe beam laser. Upon IR frequency-dependent absorption, the photothermal expansion and refractive index changes are detected via lock-in amplifier detection of variations in the reflected probe beam (532 nm) intensity as a function of IR wavelength sweeping. Consequently, the spatial resolution of the IR spectra is now diffraction-limited by the wavelength of the probe beam, to about 350 nm.

The system was purged with dry nitrogen gas to remove water vapor interferences. Data were collected by focusing the sample using the visible image, which was collected with both the 10× visible objective (for sample overview) and the 40×, 0.78 NA reflective Cassegrain-style objective for both sample visualization and O-PTIR data collection. Background spectra were collected on aluminized polypropylene mounted on epoxy to provide an accurate power spectrum of the QCL. This was carried out once at the beginning of the day and used throughout; the QCL was set to 100% power, 100 kHz repetition rate, with a pulse width of 300 ns (3% duty cycle). Probe beam was set to 25% power. Twenty scans were co-added at 6 cm^{-1} spectral resolution, with a QCL scan rate of 100 cm^{-1}/s. Sample spectra were collected at 79% QCL power, 100 kHz repetition rate, 300 nm pulse width (3% duty cycle). Probe beam was also set 79% power. Three scans were co-added at 6 cm^{-1} spectral resolution with a QCL scan rate of 100 cm^{-1}/s. All sample spectra were automatically normalized to the collected background spectrum. IR images were

collected at discrete frequencies as specified in the results section. Images were collected with 100 nm pixel sizes at a line scan rate of 1 Hz, with 10 Hz retrace.

Nano-FTIR data were acquired with a neaSNOM (neaspec GmbH, Munich-Haar, Germany) microscope at beamline 2.4 and with the synchrotron infrared nanospectroscopy (SINS) system (Bechtel et al., 2014) at beamline 5.4, ALS, according to protocols detailed previously (Wiens et al., 2016). With SINS, spectra were recorded with a modified commercial rapid-scan FTIR spectrometer (Nicolet 6700, Thermo-Scientific, Madison, WI, USA), with an asymmetric Michaelson interferometer. The second order amplitude ($s(\omega)$) and phase ($\varphi(\omega)$) spectra of the backscattered light were recorded at locations on (sample) and off (reference) the fibrils as a function of frequency, ω. For each sample and reference spectrum, 512 scans were co-added, with a spectral data spacing of 8 cm^{-1}. Spectra were processed with a fast Fourier-transform analysis suite (Nanospectroscopy Data Analysis (V.1, Advanced Light Source, Berkeley, CA, USA). Data collection with the commercial neaSNOM system at beamline 2.4 was conducted similarly, within the standard operating protocols of the system, synchrotron IR illumination and MCT detector. Finally, spectra were acquired with a neaSNOM microscope and 4.5-15 μm nano-FTIR laser illumination. Spectra were analyzed with the neaPLOT^{TM} software package (Ver. 1.9.702, neaspec GmbH, Munich-Haar, Germany). AFM and s-SNOM image data were processed in Gwyddion (Ver. 2.51, Brno, Czechia) (Nečas & Klapetek, 2012).

For all nano-FTIR spectra, whether acquired with synchrotron source IR or nano-FTIR laser illumination, the sample signal was normalized against a signal obtained from a clean location on the AuSi substrate. The gold- or platinum-coated AFM tips used in these experiments are often provided on a polydimethylsiloxane (PDMS) gel substrate that can lead to slight contamination of the tip. Even when transported in gel-free packaging, some contamination may occur in the

manufacturing process. As a consequence, PDMS appears in the reference spectrum, observed as negative peaks in the sample spectra.

For post-processing of near-field data, the second order amplitude, $s_2(\omega)$, and phase $\varphi_2(\omega)$ spectra of the demodulated complex-valued scattering coefficient σ were recorded, and the imaginary part, which corresponds to the near-field IR absorption, was calculated (Huth et al., 2012; Mastel et al., 2015) according to the relationship:

$$\mathrm{Im}[\sigma_2(\omega)] = \mathrm{Im}[s_2(\omega)e^{i[\varphi_2(\omega)]}] \qquad 3.1$$

The near-field nanoFTIR absorbance spectrum was obtained by normalizing the signal on a fibril against a signal from on a flat, non-absorbing surface location on the gold-coated wafer:

$$\text{nano-FTIR spectrum} = [s_2(\text{fibril}, \omega)/s_2(\text{Au}, \omega)] \times [\sin [\varphi_2 \text{ (fibril)} - \varphi_2 \text{ (Au)}]] \qquad 3.2$$

Spectra from all sources were exported in spc file format for common display purposes.

3.7 Conclusions

We have used three different techniques to obtain polarized IR spectra of collagen in intact tendon and as isolated fibrils. The highly linearly polarized IR laser source in the FF O-PTIR yielded spectra of intact tendon that closely matched those obtained from IR polarized FF-FTIR FPA, and the expected dichroic behavior of spectra with respect to fiber orientation was easily displayed. FF-FTIR with FPA allows for the rapid survey of large areas of intact tissue, with or without polarization, though spatial resolution is wavelength-dependent across the 5-10 μm spectral range. With O-PTIR, individual spectra could be acquired rapidly (30s), with equally good SNR, from tendon mounted on salt windows or glass microscope slides. An obvious advantage of obtaining spectra from samples on glass is that subsequent histochemical or immunohistochemical analysis could be performed.

Acquisition of FF-FTIR FPA data from individual fibrils was not feasible; however, in this first demonstration of FF O-PTIR spectra and images of a biopolymer, good data were obtained from fibrils of ~500 nm diameter. Nano-FTIR spectroscopy gave access to the smallest feasible voxel, and from fibrils of 100 to 300 nm diameter. The O-PTIR spectra with perpendicular orientation were an excellent match to nano-FTIR spectra from the smaller fibrils, obtained under synchrotron infrared light and with nano-FTIR lasers.

Relative intensities and band profiles changed between parallel and perpendicular orientations of the fibers and fibrils to polarized IR light, as expected, but distinct differences were noted among the different samples and techniques. For intact tendon, with IR light polarized parallel to fiber direction, the Amide II band intensity increased relative to the Amide I, again as expected, since the Amide II backbone mode is known to be well aligned with the fiber direction. Interestingly, the 1635 cm^{-1} shoulder in the Amide I band was more clearly defined in the O-PTIR spectra of intact tendon, in comparison to the FF-FTIR FPA results. This shoulder is often described as being mainly due to the C=O modes of the glycine residue. We conclude that the dipole moment change for this mode is more closely aligned with the molecular backbone. The increased definition of this band in the O-PTIR compared to FF-FTIR FPA spectra is thought to be due to the greater spatial resolution, with O-PTIR providing for a more pure local spectrum. The larger voxel probed with FF-FTIR FPA is averaged across more variations in fiber orientation, and could include additional, non-collagen materials. The Amide I and II bands were significantly narrower in fibril spectra compared to those from intact tendon. The low energy shoulder at 1635 cm^{-1} was barely discernible against the high energy band at 1660 cm^{-1} whether from perpendicular O-PTIR or in the smallest fibrils with nano-FTIR. The collagen fibrils have radial symmetry at this length scale, and the electrical field is parallel to the AFM tip in s-SNOM nano-FTIR; these

spectra were also effectively perpendicular. Only the FF O-PTIR could deliver spectra of fibrils with polarization parallel to the fibril orientation. The Amide II band was seen to be norrower than in intact tendon, probably owing to greater orientation purity, while the 1660 and 1635 cm^{-1} maxima were again more clearly resolved. This is the first demonstration that O-PTIR and nano-FTIR spectra give confirmatory and complementary results on collagen fibrils with diameters from 100 to 500 nm. We conclude that these spectra represent reliable profiles for control collagen type I fibrils; taken together, these results provide a broad basis for further studies of collagen in biological samples.

3.8 References

Amenabar, I., Poly, S., Nuansing, W., Hubrich, E. H., Govyadinov, A. A., Huth, F., Krutokhvostov, R., Zhang, L., Knez, M., Heberle, J., Bittner, A. M., & Hillenbrand, R. (2013). Structural analysis and mapping of individual protein complexes by infrared nanospectroscopy. *Nature Communications*, *4*, 1–9. https://doi.org/10.1038/ncomms3890

Baden, N., Kobayashi, H., & Urayama, N. (2020). Submicron-resolution polymer orientation mapping by optical photothermal infrared spectroscopy. *International Journal of Polymer Analysis and Characterization*, *25*(1), 1–7. https://doi.org/10.1080/1023666X.2020.1735851

Badger, R. M., & Pullin, A. D. E. (1954). The Infrared Spectrum and Structure of Collagen. *The Journal of Chemical Physics*, *22*(6), 1142–1142. https://doi.org/10.1063/1.1740293

Baldwin, S. J., Quigley, A. S., Clegg, C., & Kreplak, L. (2014). Nanomechanical Mapping of Hydrated Rat Tail Tendon Collagen I Fibrils. *Biophysical Journal*, *107*(8), 1794–1801. https://doi.org/10.1016/j.bpj.2014.09.003

Bechtel, H. A., Muller, E. A., Olmon, R. L., Martin, M. C., & Raschke, M. B. (2014). Ultrabroadband infrared nanospectroscopic imaging. *Proceedings of the National Academy of Sciences of the United States of America*, *111*(20), 7191–7196. https://doi.org/10.1073/pnas.1400502111

Bi, X., Li, G., Doty, S. B., & Camacho, N. P. (2005). A novel method for determination of collagen orientation in cartilage by Fourier transform infrared imaging spectroscopy (FT-IRIS). *Osteoarthritis and Cartilage*, *13*(12), 1050–1058. https://doi.org/10.1016/j.joca.2005.07.008

Camacho, N. P., West, P., Torzilli, P. A., & Mendelsohn, R. (2001). FTIR microscopic imaging of collagen and proteoglycan in bovine cartilage. *Biopolymers - Biospectroscopy Section*, *62*(1), 1–8. https://doi.org/10.1002/1097-0282(2001)62:1<1::AID-BIP10>3.0.CO;2-O

Cheheltani, R., Rosano, J. M., Wang, B., Sabri, A. K., Pleshko, N., & Kiani, M. F. (2012). Fourier transform infrared spectroscopic imaging of cardiac tissue to detect collagen deposition after myocardial infarction. *Journal of Biomedical Optics*, *17*(5), 056014. https://doi.org/10.1117/1.JBO.17.5.056014

Eklouh-Molinier, C., Happillon, T., Bouland, N., Fichel, C., Diébold, M. D., Angiboust, J. F., Manfait, M., Brassart-Pasco, S., & Piot, O. (2015). Investigating the relationship between changes in collagen fiber orientation during skin aging and collagen/water interactions by polarized-FTIR microimaging. *Analyst*, *140*(18), 6260–6268. https://doi.org/10.1039/c5an00278h

Findlay, C. R., Wiens, R., Rak, M., Sedlmair, J., Hirschmugl, C. J., Morrison, J., Mundy, C. J., Kansiz, M., & Gough, K. M. (2015). Rapid biodiagnostic ex vivo imaging at 1 μm pixel resolution with thermal source FTIR FPA. *Analyst*, *140*(7), 2493–2503. https://doi.org/10.1039/c4an01982b

Fraser, R. D. B. (1950). Infra-red microspectrometry with a 0·8 N.A. reflecting microscope. *Discuss. Faraday Soc.*, *9*(378), 378–383. https://doi.org/10.1039/DF9500900378

Gough, K. M., Zelinski, D., Wiens, R., Rak, M., & Dixon, I. M. C. (2003). Fourier transform infrared evaluation of microscopic scarring in the cardiomyopathic heart: Effect of chronic AT1 suppression. *Analytical Biochemistry*, *316*(2), 232–242. https://doi.org/10.1016/S0003-2697(03)00039-3

Huth, F., Govyadinov, A., Amarie, S., Nuansing, W., Keilmann, F., & Hillenbrand, R. (2012). Nano-FTIR absorption spectroscopy of molecular fingerprints at 20 nm spatial resolution. *Nano Letters*, *12*(8), 3973–3978. https://doi.org/10.1021/nl301159v

Kannus, P. (2000). Structure of the tendon connective tissue. *Scandinavian Journal of Medicine & Science in Sports*, *10*(6), 312–320. https://doi.org/10.1034/j.1600-0838.2000.010006312.x

Klementieva, O., Sandt, C., Martinsson, I., Kansiz, M., Gouras, G. K., & Borondics, F. (2020). Super-Resolution Infrared Imaging of Polymorphic Amyloid Aggregates Directly in Neurons. *Advanced Science*, *7*(6). https://doi.org/10.1002/advs.201903004

Lazarev, Y. A., Grishkovsky, B. A., & Khromova, T. B. (1985a). Amide I band of IR spectrum and structure of collagen and related polypeptides. *Biopolymers*, *24*(8), 1449–1478. https://doi.org/10.1002/bip.360240804

Lazarev, Y. A., Grishkovsky, B. A., & Khromova, T. B. (1985b). Amide I band of IR spectrum and structure of collagen and related polypeptides. *Biopolymers*, *24*(8), 1449–1478. https://doi.org/10.1002/bip.360240804

Lazarev, Y. A., Lazareva, A. v., Shibnev, V. A., & Esipova, N. G. (1978). Infrared spectra and structure of synthetic polytripeptides. *Biopolymers*, *17*(5), 1197–1214. https://doi.org/10.1002/bip.1978.360170508

Mastel, S., Govyadinov, A. A., de Oliveira, T. V. A. G., Amenabar, I., & Hillenbrand, R. (2015). Nanoscale-resolved chemical identification of thin organic films using infrared near-field spectroscopy and standard Fourier transform infrared references. *Applied Physics Letters*, *106*(2), 1–6. https://doi.org/10.1063/1.4905507

Nečas, D., & Klapetek, P. (2012). Gwyddion: An open-source software for SPM data analysis. *Central European Journal of Physics*, *10*(1), 181–188. https://doi.org/10.2478/s11534-011-0096-2

Orgel, J. P. R. O., Irving, T. C., Miller, A., & Wess, T. J. (2006). Microfibrillar structure of type I collagen in situ. *Proceedings of the National Academy of Sciences of the United States of America*, *103*(24), 9001–9005. https://doi.org/10.1073/pnas.0502718103

Payne, K. J., & Veis, A. (1988). Fourier transform ir spectroscopy of collagen and gelatin solutions: Deconvolution of the amide I band for conformational studies. *Biopolymers*, *27*(11), 1749–1760. https://doi.org/10.1002/bip.360271105

Reddy, R. K., Walsh, M. J., Schulmerich, M. v., Carney, P. S., & Bhargava, R. (2013). High-Definition Infrared Spectroscopic Imaging. *Applied Spectroscopy*, *67*(1), 93–105. https://doi.org/10.1366/11-06568

Reffner, J. A. (2018). Advances in infrared microspectroscopy and mapping molecular chemical composition at submicrometer spatial resolution. *Spectroscopy (Santa Monica)*, *33*(9), 12–17.

Sellaro, T. L., Hildebrand, D., Lu, Q., Vyavahare, N., Scott, M., & Sacks, M. S. (2007). Effects of collagen fiber orientation on the response of biologically derived soft tissue biomaterials to cyclic loading. *Journal of Biomedical Materials Research Part A*, *80A*(1), 194–205. https://doi.org/10.1002/jbm.a.30871

Stelzer. (1998). Contrast, resolution, pixelation, dynamic range and signal-to-noise ratio: fundamental limits to resolution in fluorescence light microscopy. *Journal of Microscopy*, *189*(1), 15–24. https://doi.org/10.1046/j.1365-2818.1998.00290.x

Taubner, T., Hillenbrand, R., & Keilmann, F. (2004). Nanoscale polymer recognition by spectral signature in scattering infrared near-field microscopy. *Applied Physics Letters*, *85*(21), 5064–5066. https://doi.org/10.1063/1.1827334

Veres, S. P., Harrison, J. M., & Lee, J. M. (2013). Repeated subrupture overload causes progression of nanoscaled discrete plasticity damage in tendon collagen fibrils. *Journal of Orthopaedic Research*, *31*(5), 731–737. https://doi.org/10.1002/jor.22292

Wiens, R., Findlay, C. R., Baldwin, S. G., Kreplak, L., Lee, J. M., Veres, S. P., & Gough, K. M. (2016). High spatial resolution (1.1 μm and 20 nm) FTIR polarization contrast imaging reveals pre-rupture disorder in damaged tendon. *Faraday Discussions*, *187*, 555–573. https://doi.org/10.1039/c5fd00168d

Wiens, R., Rak, M., Cox, N., Abraham, S., Juurlink, B. H. J., Kulyk, W. M., & Gough, K. M. (2007). Synchrotron FTIR microspectroscopic analysis of the effects of anti-inflammatory therapeutics on wound healing in laminectomized rats. *Analytical and Bioanalytical Chemistry*, *387*(5), 1679–1689. https://doi.org/10.1007/s00216-006-1095-9

Chapter 4. IR spectroscopic analysis of collagen from control and mechanically damaged positional and load-bearing tendons of the bovine foreleg

4.1 Preface

This draft manuscript is being prepared according to the format required for submission to the *Analyst*. G. Bakir conducted the experiments and spectroscopic analysis, and prepared the figures, tables and text of the entire first draft. As is normal for our collaborative manuscripts, Prof. K. M. Gough has suggested edits and then edited further in consultation with G. Bakir. We will be inviting our collaborators to provide comments and suggestions for revision before the manuscript is ready for submission to the *Analyst*, or possibly to some other journal such as *Acta Biomaterialia*, depending on our collaborative group decision. Authorship and title are given here:

G. Bakir, B.E. Girouard, K. Y. Gsell, H. Bechtel, S. Gilbert Corder, L. Kreplak, S. Veres, K. M. Gough, IR spectroscopy of collagen from damaged SDF & CDE tendons and fibrils, *Analyst* (to be submitted).

This work provides new insight, at the nanometer length scale, regarding changes in the molecular structure and organization of mechanically damaged collagen fibrils extracted from tendons that are located closely together in the forelimb but perform very different functions. As explained in the Discussion of Chapter 3, the outcomes from that study provided the basis for further research on mechanically overloaded tendons. In this chapter, changes in overloaded superficial digital flexor (SDF) and common digital extensor (CDE) bovine forelimb tendons are elucidated through the interpretation of nano-FTIR spectra of control and mechanically damaged fibrils. As before,

nano-FTIR spectra have been obtained at ~25 nm voxel resolution using the facilities at the Advanced Light Source (ALS), Berkeley. Our results support and inform parallel studies employing AFM, SEM and enzymatic degradation that found the molecular structure of damaged fibrils differed significantly from that of intact fibrils and from each other. The nano-FTIR spectroscopic analysis of mechanically damaged locations in the collagen fibrils provides new information on the nature of the changes that occur at a molecular level. In this on-going study, spectra were acquired only from points of visible damage, as first determined with AFM. Detailed analysis of the relationship between the structural and mechanical properties of collagen at the fibrillar and sub-fibrillar scale is essential for understanding structure in normal tendon, remodeling events under mechanical overload/rupture in tendons and the development of new bioengineered materials. In this project, all samples were prepared for nano-FTIR spectroscopic analysis by Bakir at the Gough Lab upon receiving the tendon pieces from our collaborator, as explained in the method section of this chapter as well as in the Appendices in Chapter 2. Data collection took place at ALS, Berkeley, CA, USA, using either the Neasnom microscope or the SINS instrument. The data were collected by Bakir on-site at ALS during a beamtime session scheduled in November 2019. The remaining data were collected by Bakir and Girouard remotely during a total of five beamtime sessions scheduled between the years 2020 and 2022. Bechtel and Gilbert-Cobert provided assistance and guidance in instrument setup and sample insertion at ALS after receiving our samples on-site. Subsequently, all data were processed by Bakir in the Gough Lab. The first draft of manuscript to be published is prepared by Bakir with editing and guidance from Dr. Gough.

4.2 Abstract

Collagen is one of the most widely studied proteins due to its natural abundance, the distinctive triple helix molecular structure, and the critical roles it plays in mammalian structures. Individual collagen molecules are ~360 nm length, 1.5 nm diameter, and exhibit cylindrical symmetry in the form of regular annular periodicity along the long axis. The molecules assemble to create fibrils (< 1 μm diameter), with formation of covalent crosslinks between molecules. Fibrils in turn combine to form fibers, banded together into fascicles, the major components of structural tissues throughout the body, including skin, cartilage, and tendon. As tendons interconnect muscle and bone, they have evolved to withstand intense, repeated stress when they transmit the forces from muscles to achieve movement and stability. Near field Fourier Transform Infrared spectroscopy (nano-FTIR) was used here, for the first time, to obtain direct spectrochemical data on control and mechanically damaged collagen fibrils extracted from bovine forelimb superficial digital flexor (SDF) and common digital extensor (CDE) tendons, at ~25 nm spatial resolution. The load-bearing SDF and the positional CDE tendons exhibit different responses to overload that are postulated to derive at least in part from the difference in number, density, and type of crosslinks. Infrared spectroscopy enables us to probe structure and orientation at the nanoscale level, since band positions, shapes, and relative intensities depend on molecular conformation and on the tip-aligned polarization inherent in sSNOM nano-FTIR. We found that the amide I band maximum shifted from 1663 cm^{-1} to 1665 cm^{-1} in all spectra from overloaded fibrils, SDF and CDE. The amide I bands were narrower in all overload fibril spectra owing to a significant decrease in the intensity of the lower energy shoulder within the amide I band, relative to that seen in amide I bands from control fibrils. This decrease was more pronounced in the SDF OVER spectra, giving the first direct spectroscopic evidence that the molecular organization had

changed more significantly in this load bearing tendon. Detailed analysis of the relationship between the structural and mechanical properties of collagen at the fibrillar and sub-fibrillar scale is essential for understanding remodeling events under mechanical overload/rupture in tendons and for contributing to the development of new bioengineered materials.

4.3 Introduction

Collagen is the most abundant protein in mammals, accounting for one-third of the total body protein by dry weight (Gelse et al., 2003; Tiong et al., 2008) and ~75% of the dry weight of tendon. The functional properties of collagen-based mammalian tissues are determined by their complex hierarchical structures, chemical cross-linking, and post-translational modifications (Avery & Bailey, 2008). Collagen molecules are lengthy and slender (~360 nm length, 1.5 nm diameter). When they register and connect to form fibrils (<1 μm diameter), a hierarchical organization is created that imparts a radial symmetry which is maintained when fibrils assemble into fibres, fascicles and then into tendons, which are in turn composed of many aligned collagen fibres, (Buehler, 2006; Zhang et al., 2022). Cross-linking varies with development and age; some changes are normal enzymatic responses, others arise from non-enzymatic changes that occur in diabetes, stress and age to create advanced glycation end products (AGEs) (Ellingson et al., 2022).

Tendons are subject to great physical stresses as their role is to transmit the forces generated by muscle to bone in order to achieve motion and stability in mammals (Magnusson et al., 2016). Positional tendons (e. g.: digital extensors and flexors of the hand) enable precise motion; load-bearing tendons (e. g. Achilles) provide the energy storing/release capability for forward motion, including repetitive, highly stressful actions such as running. In humans, the mechanical characteristics of energy-storing tendons promote locomotor efficiency resulting in increased

resisting performance against significant stress has been reported (Lichtwark & Wilson, 2005, 2007). In contrast, positional tendons have been found to have less ability to withstand strains (Birch, 2007; Depalle et al., 2015; Patel et al., 2021). Establishing the relationship between structural and mechanical properties is key to understanding normal function in healthy tendon, remodeling events in injured tendons, and the development of bioengineered materials.

Different types of responses have been observed in positional and energy-storing tendons in small and large mammals such as rat (Lin et al., 2020, 2023) and steer (Gsell et al., 2023; Herod et al., 2016; Quigley, Bancelin, Deska-Gauthier, Légaré, Kreplak, et al., 2018; Quigley, Bancelin, Deska-Gauthier, Légaré, Veres, et al., 2018). The responses are hypothesized to be related to different crosslinking and may be more likely to appear only when the tendon or fibril is stretched beyond the yield point, and to rupture (Baldwin et al., 2016; Herod et al., 2016). In response to rupture, positional fibrils undergo a repeating kink distortion along their entire length, seen as slippage or discrete plasticity, and serial bulges may be produced, possibly through axial compression. Energy storing fibrils have not shown this in AFM, but tensile tests revealed a three-phase response to stress, with stiffening in the final phase. The results were interpreted as evidence that molecular sliding is limited, and any additional extension must occur via molecular straightening and direct stretching of collagen polypeptide α-chains (Quigley, Bancelin, Deska-Gauthier, Légaré, Kreplak, et al., 2018). Recently, Gsell, Veres and Kreplak have shown that individual fibrils from bovine CDE, SDF and rat tail tendon respond differently to MMP-1 enzymatic degradation (Gsell et al., 2023). Fibrils from the positional tendons are larger on average and more susceptible to enzymatic cleavage, while the smaller, high stress flexor fibrils are resistant. This resistance to enzymatic cleavage may account for lower turnover and thus greater longevity of flexor tendons *in vivo*.

Collagen has been studied with infrared (IR) spectroscopy and polarized IR spectroscopy for many decades because of its unique structure and hierarchical organization, (Badger & Pullin, 1954; Bryan et al., 2007; Fraser, 1950; Gelse et al., 2003; Hodge & Schmitt, 1960; Mankar et al., 2022; Meyer, 2019; Querido et al., 2021). Band intensities change with orientation of polarized IR light; positions of band maxima are sensitive to molecular bonding and conformation. Hence, chemical and mechanical changes to the structure and annular periodicity of normal fibrils should be readily identifiable. In our studies of control and mechanically damaged collagen from bovine tail tendon (Wiens et al., 2016) , we showed the value of far-field polarization contrast IR imaging with a Focal Plane Array and the first nano-FTIR spectra and images of collagen fibrils at 20 nm spatial resolution. More recently, we showed that far field, optical-photothermal IR (O-PTIR) polarization contrast imaging yielded results that could be compared to both far field FPA wavelength-dependent imaging of intact tendon at the micron length scale, and near field nano-FTIR spectroscopy of fibrils at the nanoscale. Since the O-PTIR method data are acquired with 400 to 500 nm, wavelength-independent spatial resolution, it provides an additional link from mm to nm length scales and enables polarization contrast parallel and perpendicular to the fiber or fibril direction (Bakir et al., 2020).

In the present study, we extracted collagen fibrils from the superficial digital flexor (SDF, energy-storing) and common digital extensor (CDE, positional) tendons of the bovine forelimb prepared as before (Quigley, Bancelin, Deska-Gauthier, Légaré, Kreplak, et al., 2018; Quigley, Bancelin, Deska-Gauthier, Légaré, Veres, et al., 2018) for comparison of control and mechanically overloaded fibrils. The sensitivity and spatial resolution achievable with nano-FTIR IR enabled us to examine collagen fibrils with heights as low as 75 to 150 nm. (Gsell et al., 2023; Herod et al., 2016; Kalson et al., 2015). Here, we show the first nano-FTIR spectroscopic analysis of such fibrils

with a probe voxel dimension of ~25 nm, to give direct spectroscopic evidence of molecular differences in the collagen of positional and load-bearing tendons that have undergone overload stress.

4.4 Methods

4.4.1 Preparation of collagen tendons and fibrils

Pairs of control and mechanically damaged tendons from positional and energy-storing parts of the bovine forelimb were prepared at Dalhousie University, as described previously (Bakir et al., 2020; Wiens et al., 2016). Briefly, tendons were dissected from the forelimb; a segment (1 cm in length) was cut from each to serve as a control and stored in phosphate-buffered saline solution (PBS) containing 1% antibiotic/antimycotic solution (product A5955, Sigma-Aldrich Canada) with a pH of 7.4 at 4 °C. A portion of each tendon was clamped into an MTS Series 458 servo-hydraulic testing machine for mechanical loading. Each tendon piece underwent a computer-controlled pre-loading cycle at 1% strain per second to a maximum strain of 10%, followed by 10 overload cycles into the plastic region of the load-deformation curve. The damaged segments, approximately 10 mm long by 4 mm in diameter, were stored at room temperature for 24 hours in PBS, containing 1% antibiotic/antimycotic solution and 1% of protease inhibitor (product S8820, Sigma-Aldrich Canada), and shipped overnight to the University of Manitoba, where they were immediately washed and rinsed in ultra-pure water. In order to remove all contaminants coming from the PBS medium, the tendon segments were transferred to a 1.5 mL Eppendorf with ultra-pure water, soaked for 20 minutes and centrifuged for 5 min at 5300 ×g, rinsed again and transferred to a fresh Eppendorf; this cycle was repeated ten times. The rinsed segment was

dissected further using tweezers and a fine-tipped metal rod in 1 mL of ultra-pure water until the mixture appeared cloudy due to suspended fibers and fibrils. Droplets of the suspensions were deposited on 1 cm^2 square stripped-gold substrates (Platypus Technologies LLC) for nano-FTIR analysis and onto CaF_2 salt windows for O-PTIR analysis. The remaining tendon sections were covered with OCT (Sakura Finetek Inc. USA), frozen in isopentane-cooled in liquid N_2, and stored at -80 °C. Cryosections from these intact tendon segments were cut to 5 μm thickness at −21°C and mounted on CaF_2 salt windows for FFIR analysis.

4.4.2 Nano-FTIR spectroscopy

All Nano-FTIR data were collected with either a neaSNOM (Neaspec GmbH, Germany) microscope on Beam Line 2.4 or with the Synchrotron Infrared NanoSpectroscopy (SINS) instrument (Bechtel et al., 2014) on Beam Line 5.4 at the Advanced Light Source (ALS), Lawrence Berkeley National Laboratory (LBNL), Berkeley, California. The ALS runs in continuous top-off mode with a current of 500 mA. The SINS spectra were collected with a commercial rapid scan FTIR spectrometer (Nicolet 6700, Thermo-Scientific) modified with an asymmetric Michelson interferometer (Bechtel et al., 2014). Synchrotron IR light is transmitted through a beam splitter such that half illuminates the AFM tip, and the other half is sent to the moving mirror. The second order amplitude $s_2(\omega)$ and phase $\varphi_2(\omega)$ spectra of backscattered light were measured as a function of frequency at locations on fibril (sample) and gold (reference). For each sample and reference spectrum, 512 scans were co-added, with a spectral data spacing of 8 cm^{-1}. Spectra were processed with a fast Fourier Transform analysis suite (Nanospectroscopy Data Analysis (V.1, Advanced Light Source). Similarly, data collection using the commercial neaSNOM system at beamline 2.4 was conducted by the regular operating protocols of system, synchrotron IR

illumination, and mercury cadmium telluride detector. Spectra were analyzed with the neaPLOT™ software package (Ver. 1.9.702, neaspec GmbH, Germany). AFM images were processed using the Gwyddion imaging software (Ver. 2.51, Brno, Czechia) (Nečas & Klapetek, 2012).

For all nano-FTIR spectra, whether collected with SINS (BL 5.4) or Neaspec (BL 2.4), the sample signal was ratioed to a signal that was acquired from a spot on the AuSi wafer that was clean. The real and imaginary components of the optical dielectric function of the complex-valued second-order scattering coefficient (σ_2) were used to derive the second-order scattering amplitude $s_2(\omega)$ and phase $\varphi_2(\omega)$ spectra (Huth et al., 2012; Mastel et al., 2015), according to Equation 1:

$$\mathrm{Im}[\sigma_2(\omega)] = \mathrm{Im}\left[s_2(\omega)e^{i[\varphi_2(\omega)]}\right] \quad 4.1$$

The near-field absorbance spectrum was then created by post-processing in a Fast Fourier Transform analysis package (Nanospectroscopy Data Analysis v.1) or NeaPLOT, depending on the instrument, normalizing the signal from fibril against that of background taken at a clear surface on the AuSi wafer, according to equation 2:

$$\text{Nano-FTIR spectrum} = \frac{s_2(fibril,\omega)}{s_2(gold,\omega)}\sin[\varphi_2(fibril,\ \omega) - \varphi_2(gold,\ \omega)] \quad 4.2$$

For standard display reasons, spectra from all sources were exported in the spc file type. Further processing was carried out in OMNIC (Thermo Electron Corporation).

4.5 Results

Typical AFM images of fibrils, recorded at 10 nm step size are shown in **Figure 5.1**. The AFM images from control fibrils show D-banding while overloaded fibrils show unravelled and kinked regions. More obvious bulges were sometimes observed (**Supplemental Figure 4.1**).

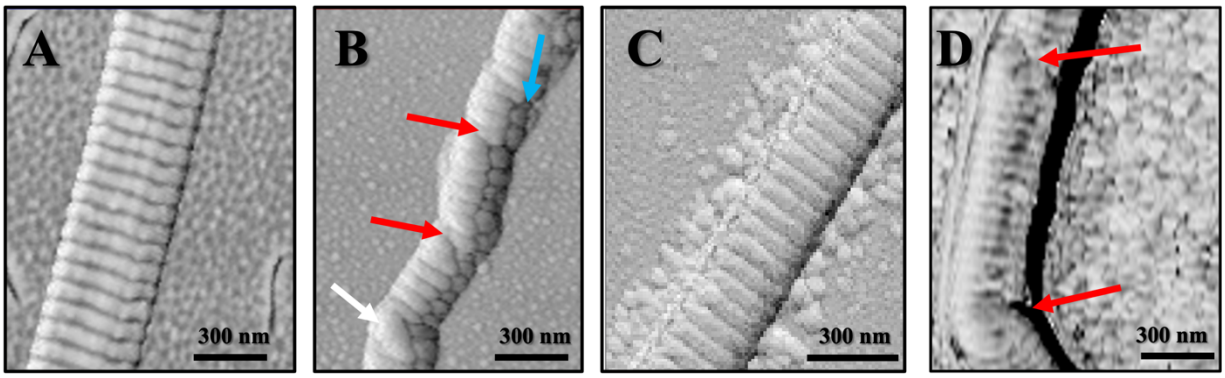

Figure 4.1 Typical AFM images of fibrils, recorded at 10 nm step size. A. SDF Control, B. SDF Overloaded, C. CDE Control, D. CDE Overloaded. AFM images from control fibrils show D-banding structure while overloaded fibrils show kinks (red arrows), unravelled subfibrils (blue arrow), and bulge (white arrow) features.

Representative spectra from control and mechanically damaged fibrils from each type of tendon (SDF and CDE) are shown in **Figure 4.2**. All spectra represent an average of ~10 single point spectra taken on the fibrils. Averaging was necessary as the signal-to-noise ratio (SNR) for spectra acquired at ALS is not very large (Bakir et al., 2020). Most spectra have equally good SNR and similar level baselines. In some cases, the conditions at the end station were poor giving rise to intractable artifacts that could not be removed by averaging, such as can be seen in Fig. 4.2, CDE CON, red spectrum, beam line 2.4, n=12 and to a lesser extent in CDE OVER purple spectrum, beam line 5.4, n=6. Polydimethylsiloxane (PDMS) contamination sometimes appeared in the reference spectrum, resulting in negative peaks at 1265, 1100-1000 and 800 cm^{-1} and interfering with our ability to examine bands below 1300 cm^{-1} (see also:(Bakir et al., 2020).)

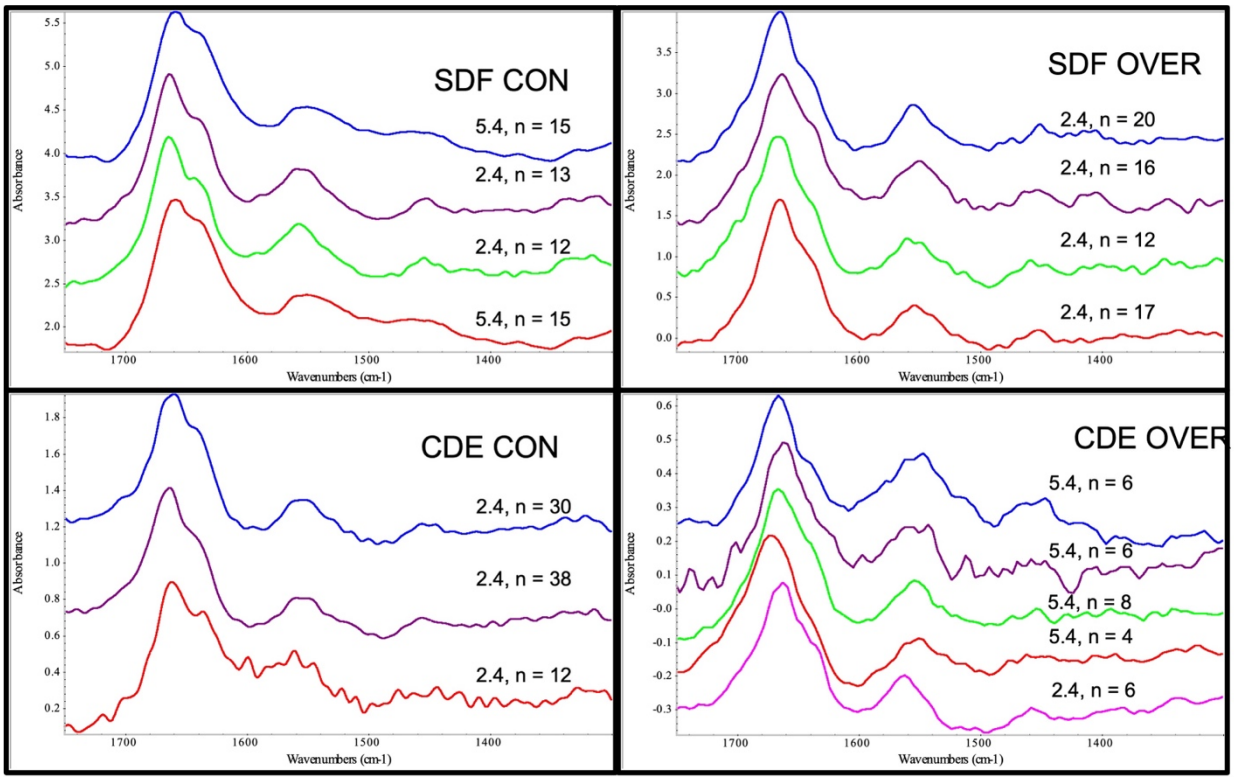

Figure 4.2 Averaged spectra of control and overloaded fibrils from SDF and CDE tendons. Each fibril was imaged at either BL 2.4 or 5.4, as shown, where n = number of spectra averaged from each fibril. The spectra shown in Figure 3 are averages of each of these individual spectra for each type of fibril. Spectra were first displayed as full scale, then offset for clarity.

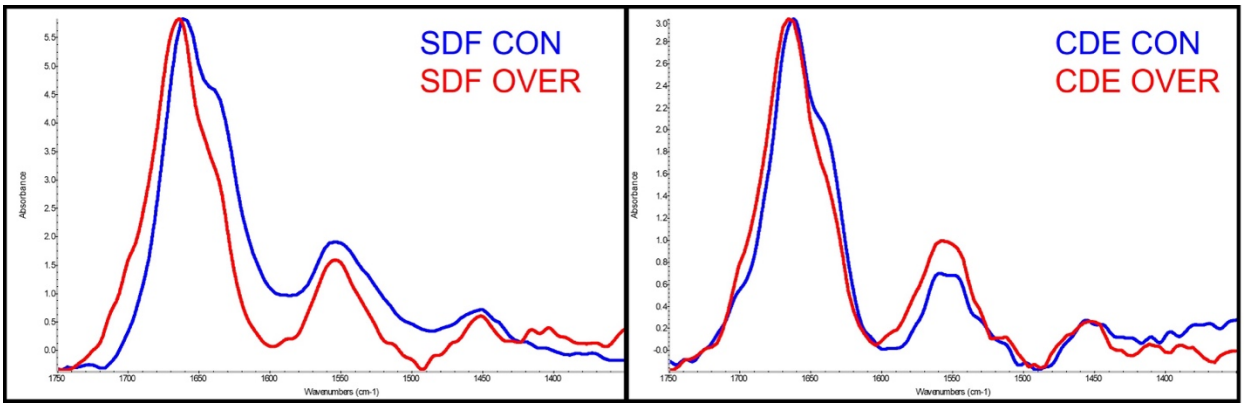

Figure 4.3 Nano-FTIR spectra of Control (blue) and Overloaded (red) tendon fibrils. Left SDF, Right CDE. Each spectrum is the average of ~70 nano-FTIR spectra, acquired at BL 2.4 and 5.4. Spectra are displayed at full scale.

The typical nano-FTIR spectrum for a collagen fibril shows the dominant amide I band (carbonyl stretch at ~1660 cm^{-1}), as it is mainly aligned perpendicularly to the fibril direction, and the weaker amide II band (C-N backbone stretch with some C-N-H angle bend at ~1545 cm^{-1}). A third band is evident around 1465 cm^{-1}, assigned as the CH_2 deformation of the proline ring (Badger & Pullin, 1954; Bakir et al., 2020; Camacho et al., 2001; Fraser, 1950; Wiens et al., 2016). The spectral region shown in **Figure 4.2** and **Figure 4.3** stops at 1300 cm^{-1}, as the expected amide III bands overlapped with the polydimethylsiloxane (PDMS) contamination bands at 1265 cm^{-1} and thus, their analysis was not possible (Bakir et al., 2020).

A summary of the integrated band areas created by processing the averaged spectra in Figure 4.3, is provided in Table 4.1. The ratios of pairs of integrated areas are shown in Table 4.2. along with the full width at half maximum (FWHM) for each band, in all four spectral types. These data enable a comparison of positions of band maxima, relative intensities, and FWHM among the spectra both SDF and CDE control and overload samples.

Table 4.1 Integrated band areas from averaged fibril spectra in Figure 3

Band, Left & Right Edges	SDF CON	SDF OVER	CDE CON	CDE OVER
Amide I (1685.480-1612.198)	299.	262.	396.	136.
Amide I, High (1685.480-1646.911)	174.	188.	279.	104.
Amide I, Low (1646.911-1612.198)	125.	74.	131.	37.
Amide II (1577.486-1527.346)	40.	55.	85.	41.
Proline (1471.420-1434.779)	9.4	9.4	21.	9.5
Amide I Left (1712.479-1685.480)	22.	53.	52.	25.

Table 4.2 Ratios of some integrated band areas given in Table 1 and FWHM of amide I

Ratio of integrated intensities	SDF CON	SDF OVER	CDE CON	CDE OVER
Amide I (Low)/ Amide I (High)	0.72	0.39	0.49	0.38
Amide II / Amide I Total	0.13	0.21	0.21	0.30
Proline/Amide I	0.03	0.04	0.05	0.07
Proline/Amide II	0.23	0.17	0.24	0.22
Amide I FWHM	56	50	56	48

4.6 Discussion

In this work, we have acquired the first nano-FTIR spectra from collagen fibrils extracted from superficial digital flexor (SDF, load-bearing) and common digital extensor (CDE, positional) bovine forelimb tendons with and without mechanical overload. Spectra were acquired at beam lines 2.4 and 5.4 at the ALS, from replicate fibrils prepared at different times. Our goal was to identify molecular changes in damaged fibrils by exploring spectra acquired with tip-aligned

polarized infrared spectroscopy at ~25 nm pixel resolution. Due to this electric field alignment, the absorption bands of functional groups aligning parallel to the fibril direction are essentially inactive, while those perpendicular to the fibril are enhanced (Bakir et al., 2020; Wiens et al., 2016). Changes in the internal alignment and molecular bonding can be discerned by comparison between spectra from control and mechanically overloaded tendon.

The stress-strain curves and shape of positional and energy-storing fibrils were used by Quigley et al. in 2018 to highlight the different response of these fibrils when pulled to rupture (Quigley, Bancelin, Deska-Gauthier, Légaré, Kreplak, et al., 2018; Quigley, Bancelin, Deska-Gauthier, Légaré, Veres, et al., 2018). AFM images acquired prior to nano-FTIR data collection recorded at 10 nm step size show D-banding structure in control fibrils while overloaded fibrils show unravelled and kinked regions (Figure 4.1). The SDE fibrils were more likely to show unravelling instead of the discrete plasticity slippage; however, locations showing such damage were found and nano-FTIR spectra were acquired at these sites.

Bulk tendon-level tensile testing techniques probe average molecular changes within a large population of fibrils but are not sensitive to variations in molecular packing along single collagen fibrils, changes that would explain the appearance of discrete sites of plastic damage (repeating sequential kinks) along fibrils after tensile testing (Baldwin et al., 2016; Herod et al., 2016). Importantly, mechanical stress sufficient to *rupture* a fibril creates a different, localized type of damage in positional tendons, where bulges are likely induced by axial compression (Kreplak et al., 2020; Quigley, Bancelin, Deska-Gauthier, Légaré, Kreplak, et al., 2018). It is thought that the molecules are not denatured within the bulge regions, but this type of distortion was rarely seen in our samples (See Supplemental Figure 4.1) and will have to be explored further under the tip-aligned polarization inherent in nano-FTIR, as well as with polarized O-PTIR.

The entire band and the band maxima were slightly blue-shifted for amide I and II bands in spectra from both the overload tendons Figure 4.2 and Figure 4.3. This is possibly indicative of stretched collagen triple helices. The amide I band maximum was at 1663 cm^{-1} in CDE and SDF CON spectra, while it was found at 1665 cm^{-1} for their corresponding overloaded fibrils. This agrees with Second Harmonic Generation anisotropy parameter measurements on ruptured positional fibrils (Kreplak et al., 2020) showing that collagen triple helices appear to be "straighter" compared to paired unloaded controls (see Figure 7A in (Herod et al., 2016)).

The amide I band typically has two local maxima, the more intense appears ~1660 cm^{-1} while a lower energy, lower intensity shoulder appears ~1635 cm^{-1} and accounts for approximately one third of the total band area in unpolarized IR spectra of intact collagen. The lower energy band has been found to be smaller in control fibrils under tip-aligned nano-FTIR, as well as in O-PTIR spectra with polarization perpendicular to fibril length. It is more prominent in O-PTIR spectra of fibrils where light is polarized parallel to the fibril length (Bakir et al., 2020). The assignment of this shoulder has been tested (2007 Bryan & Mendelsohn) and debated for many years. Glycine represents about one third of all amino acid residues in collagen; proline and hydroxylproline represent about 20% of all residues. The lower energy shoulder at 1635 cm^{-1} may arise from the carbonyl group on proline; the band has been reported to appear at a lower energy than the typical α-helical position of 1655 cm^{-1} (Lazarev et al., 1985; Payne & Veis, 1988). It has also been posited to arise from the glycine carbonyl, which is forced to point outward from the triple helix structure, allowing H-bond formation between C=O and water. This would weaken the bond and lower the vibrational energy of the glycine carbonyl (Payne & Veis, 1988).

In the present study, the nano-FTIR spectra from CDE and SDF CON fibrils (Figure 4.2 and Figure 4.3), FWHM and relative band intensities (Table 4.2) were found to be similar to

previous studies of controls (Bakir et al., 2020). The low-energy shoulder (amide I, Low, Table 4.2) was observed in all spectra, with lower intensity than under other polarizations, as expected. However, it was more prominent in the spectra of the undamaged CDE CON and SDF CON fibrils and the amide I band was narrower compared to the spectra from the control fibrils (See: FWHM in Table 4.2). Regardless of the specific amino acid residue(s) responsible for this low energy shoulder, this information is sufficient to conclude that the molecular orientation and organization at damage sites had been altered. These residues are no long tip-aligned, indicating unravelling and reorientation of the triple helix at the molecular level. The decrease in this shoulder and that associated narrowing of the amide I band was greater for SDF OVER compared to SDF CON than in CDE OVER compared to CDE CON, supporting other evidence of straightening of the molecular structure (Kreplak et al., 2020; Quigley, Bancelin, Deska-Gauthier, Légaré, Kreplak, et al., 2018).

The typical collagen fibril nano-FTIR spectrum shows enhanced amide I band intensity and decreased amide II band intensity (Bakir et al., 2020; Wiens et al., 2016) relative to unpolarized spectra, again because the electric field is aligned perpendicular to the fiber direction. Despite this tip-sample polarization enhancement, backbone mode intensities increased for SDF and CDE OVER spectra compared to their respective controls, as seen from the ratios of amide II to amide I and proline to amide I (Table 4.2). The change is very small for the weak proline band and may not be significant. However, it is much greater for the amide II to amide I ratios and, again, is more pronounced for SDF OVER than CDE OVER. Increase in the intensity of amide II relative to amide I shows that the backbone is twisted to be more closely aligned with the tip. Spectra of the damaged regions that were explored here are further direct evidence of the difference between these types of tendon and disorganized-helical structures that result under mechanical overload.

The unique triple helical structure and hierarchical structure of collagenous materials results in a unique and distinctive IR spectrum that is conformation and orientation dependent, at the nanoscale. Our study confirms that Nano-FTIR could characterize not only intact but also damaged tendons. This finding will impact understanding of the healing process and tissue repair, which provide a unique insight on how damaged tissues could undergo structural changes. Future studies, far field imaging of intact tendon, O-PTIR of intact and fibrillar collagens and nano-FTIR of individual fibrils will allow better understanding of the impact of such damage in all tendons under a wide variety of conditions.

4.7 Conclusions

This study utilized AFM and nano-FTIR spectroscopy to examine the impact of mechanical overload on collagen fibrils in two distinct tendon types, SDF and CDE. Notably, our investigation yielded the first direct spectrochemical evidence derived from overloaded fibrils extracted from these tendons. This pioneering utilization of nano-FTIR spectroscopy in this specific area of research offers valuable insights into the structural and compositional changes induced by mechanical overload in tendons.

The AFM images revealed that overloaded fibrils exhibited kinks, unravelled subfibrils, and bulges. The nano-FTIR spectra showed the differences in band shapes, relative intensities and band maxima. The integrated band areas of these bands were measured and compared between control and overloaded fibrils, as well as between SDF and CDE tendons. Energy-storing tendons are physically and mechanically distinct from positional tendons. The ratio of the amide I (low) to amide I (high) band was significantly lower in overloaded SDF fibrils compared to control SDF fibrils, suggesting a change in the secondary structure of collagen due to mechanical overload.

Similarly, the ratio of the amide II to amide I (high) band was significantly higher in overloaded CDE fibrils compared to control CDE fibrils, indicating a change in the orientation of the collagen fibres. The amide I band was slightly narrower in spectra from overloaded CDE fibrils than the overloaded SDF fibrils. The narrower amide I band and low energy shoulder in the spectra of damaged fibrils indicate altered molecular orientation and organization, with unraveling and reorientation of triple helices. The extent of this alteration was greater in SDF OVER compared to SDF CON and CDE OVER compared to CDE CON, supporting the evidence of molecular structure straightening. Collagen triple helices appear to be straighter in overloaded fibrils compared to unloaded controls, which is consistent with the amide I band maximum being at 1665 cm^{-1} in overloaded fibrils and 1663 cm^{-1} in unloaded controls. This finding is supported by Second Harmonic Generation anisotropy parameter measurements on ruptured positional fibrils.

Overall, the results suggest that mechanical overload can lead to changes in the structure and orientation of collagen fibrils in tendons, which may have implications for tendon injury and healing. The use of AFM and nano-FTIR spectroscopy provides a powerful tool for studying these changes at the nanoscale level. The relationship between structural and mechanical properties is crucial to understanding normal performance and remodelling processes in tendons under mechanical overload/rupture, as well as for the development of bioengineered materials.

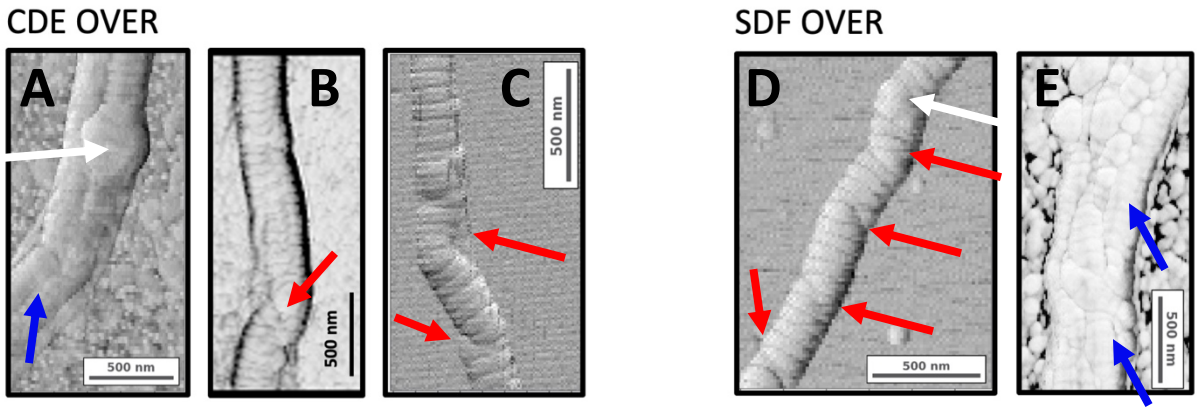

Supplemental Figure 4.1 AFM images of overloaded CDE and SDF fibrils. AFM images show the variations of kinks (red arrows), bulges (white arrows), and unravelling of the larger fibrils into sub-fibrils (blue arrows), that have been observed. In the case of unravelling, D-band structure is seen within the sub-fibrils.

4.8 References

Avery, N. C., & Bailey, A. J. (2008). Restraining cross-links responsible for the mechanical properties of collagen fibers: Natural and artificial. *Collagen: Structure and Mechanics*, 81–110. https://doi.org/10.1007/978-0-387-73906-9_4

Badger, R. M., & Pullin, A. D. E. (1954). The Infrared Spectrum and Structure of Collagen. *The Journal of Chemical Physics*, *22*(6), 1142–1142. https://doi.org/10.1063/1.1740293

Bakir, G., Girouard, B. E., Wiens, R., Mastel, S., Dillon, E., Kansiz, M., & Gough, K. M. (2020). Orientation Matters: Polarization Dependent IR Spectroscopy of Collagen from Intact Tendon Down to the Single Fibril Level. *Molecules*, *25*(18), 4295. https://doi.org/10.3390/molecules25184295

Baldwin, S. J., Kreplak, L., & Lee, J. M. (2016). Characterization via atomic force microscopy of discrete plasticity in collagen fibrils from mechanically overloaded tendons: Nano-scale structural changes mimic rope failure. *Journal of the Mechanical Behavior of Biomedical Materials*, *60*, 356–366. https://doi.org/10.1016/j.jmbbm.2016.02.004

Bechtel, H. A., Muller, E. A., Olmon, R. L., Martin, M. C., & Raschke, M. B. (2014). Ultrabroadband infrared nanospectroscopic imaging. *Proceedings of the National Academy of Sciences of the United States of America*, *111*(20), 7191–7196. https://doi.org/10.1073/pnas.1400502111

Birch, H. L. (2007). Tendon matrix composition and turnover in relation to functional requirements. *International Journal of Experimental Pathology*, *88*(4), 241–248. https://doi.org/10.1111/j.1365-2613.2007.00552.x

Bryan, M. A., Brauner, J. W., Anderle, G., Flach, C. R., Brodsky, B., & Mendelsohn, R. (2007). FTIR studies of collagen model peptides: Complementary experimental and simulation approaches to

conformation and unfolding. *Journal of the American Chemical Society*, *129*(25), 7877–7884. https://doi.org/10.1021/ja071154i

Buehler, M. J. (2006). Nature designs tough collagen: Explaining the nanostructure of collagen fibrils. *Proceedings of the National Academy of Sciences of the United States of America*, *103*(33), 12285–12290. https://doi.org/10.1073/pnas.0603216103

Camacho, N. P., West, P., Torzilli, P. A., & Mendelsohn, R. (2001). FTIR microscopic imaging of collagen and proteoglycan in bovine cartilage. *Biopolymers - Biospectroscopy Section*, *62*(1), 1–8. https://doi.org/10.1002/1097-0282(2001)62:1<1::AID-BIP10>3.0.CO;2-O

Depalle, B., Qin, Z., Shefelbine, S. J., & Buehler, M. J. (2015). Influence of cross-link structure, density and mechanical properties in the mesoscale deformation mechanisms of collagen fibrils. *Journal of the Mechanical Behavior of Biomedical Materials*, *52*, 1–13. https://doi.org/10.1016/j.jmbbm.2014.07.008

Ellingson, A. J., Pancheri, N. M., & Schiele, N. R. (2022). Regulators of Collagen Crosslinking in Developing and Adult Tendons. *European Cells and Materials*, *43*, 130–152. https://doi.org/10.22203/eCM.v043a11

Fraser, R. D. B. (1950). Infra-red microspectrometry with a 0·8 N.A. reflecting microscope. *Discuss. Faraday Soc.*, *9*(378), 378–383. https://doi.org/10.1039/DF9500900378

Gelse, K., Pöschl, E., & Aigner, T. (2003). Collagens - Structure, function, and biosynthesis. *Advanced Drug Delivery Reviews*, *55*(12), 1531–1546. https://doi.org/10.1016/j.addr.2003.08.002

Gsell, K. Y., Veres, S. P., & Kreplak, L. (2023). Single collagen fibrils isolated from high stress and low stress tendons show differing susceptibility to enzymatic degradation by the interstitial collagenase matrix metalloproteinase-1 (MMP-1). *Matrix Biology Plus*, *18*, 100129. https://doi.org/10.1016/j.mbplus.2023.100129

Herod, T. W., Chambers, N. C., & Veres, S. P. (2016). Collagen fibrils in functionally distinct tendons have differing structural responses to tendon rupture and fatigue loading. *Acta Biomaterialia*, *42*, 296–307. https://doi.org/10.1016/j.actbio.2016.06.017

Hodge, A. J., & Schmitt, F. O. (1960). The charge profile of the tropocollagen macromolecule and the packing arrangement in native-type collagen fibrils. *Proceedings of the National Academy of Sciences*, *46*(2), 186–197. https://doi.org/10.1073/pnas.46.2.186

Huth, F., Govyadinov, A., Amarie, S., Nuansing, W., Keilmann, F., & Hillenbrand, R. (2012). Nano-FTIR absorption spectroscopy of molecular fingerprints at 20 nm spatial resolution. *Nano Letters*, *12*(8), 3973–3978. https://doi.org/10.1021/nl301159v

Kalson, N. S., Lu, Y., Taylor, S. H., Starborg, T., Holmes, D. F., & Kadler, K. E. (2015). A structure-based extracellular matrix expansion mechanism of fibrous tissue growth. *ELife*, *4*(MAY), 1–22. https://doi.org/10.7554/eLife.05958

Kreplak, L., Peacock, C., Lee, E., Beral, T., Cisek, R., & Tokarz, D. (2020). Buckling and torsional instabilities of a nanoscale biological rope bound to an elastic substrate. *ACS Nano*, *14*(10), 12877–12884. https://doi.org/10.1021/acsnano.0c03695

Lazarev, Y. A., Grishkovsky, B. A., & Khromova, T. B. (1985). Amide I band of IR spectrum and structure of collagen and related polypeptides. *Biopolymers*, *24*(8), 1449–1478. https://doi.org/10.1002/bip.360240804

Lichtwark, G. A., & Wilson, A. M. (2005). In vivo mechanical properties of the human Achilles tendon during one-legged hopping. *Journal of Experimental Biology*, *208*(24), 4715–4725. https://doi.org/10.1242/jeb.01950

Lichtwark, G. A., & Wilson, A. M. (2007). Is Achilles tendon compliance optimised for maximum muscle efficiency during locomotion? *Journal of Biomechanics*, *40*(8), 1768–1775. https://doi.org/10.1016/j.jbiomech.2006.07.025

Lin, A. H., Allan, A. N., Zitnay, J. L., Kessler, J. L., Yu, S. M., & Weiss, J. A. (2020). Collagen denaturation is initiated upon tissue yield in both positional and energy-storing tendons. *Acta Biomaterialia*, *118*, 153–160. https://doi.org/10.1016/j.actbio.2020.09.056

Lin, A. H., Slater, C. A., Martinez, C. J., Eppell, S. J., Yu, S. M., & Weiss, J. A. (2023). Collagen fibrils from both positional and energy-storing tendons exhibit increased amounts of denatured collagen when stretched beyond the yield point. *Acta Biomaterialia*, *155*, 461–470. https://doi.org/10.1016/j.actbio.2022.11.018

Magnusson, S. P., Heinemeier, K. M., & Kjaer, M. (2016). Metabolic Influences on Risk for Tendon Disorders. In P. W. Ackermann & D. A. Hart (Eds.), *Advances in Experimental Medicine and Biology* (Vol. 920). Springer International Publishing. https://doi.org/10.1007/978-3-319-33943-6

Mankar, R., Gajjela, C. C., Bueso-Ramos, C. E., Yin, C. C., Mayerich, D., & Reddy, R. K. (2022). Polarization Sensitive Photothermal Mid-Infrared Spectroscopic Imaging of Human Bone Marrow Tissue. *Applied Spectroscopy*, *76*(4), 508–518. https://doi.org/10.1177/00037028211063513

Mastel, S., Govyadinov, A. A., De Oliveira, T. V. A. G., Amenabar, I., & Hillenbrand, R. (2015). Nanoscale-resolved chemical identification of thin organic films using infrared near-field spectroscopy and standard Fourier transform infrared references. *Applied Physics Letters*, *106*(2), 1–6. https://doi.org/10.1063/1.4905507

Meyer, M. (2019). Processing of collagen based biomaterials and the resulting materials properties. *BioMedical Engineering Online*, *18*(1), 1–74. https://doi.org/10.1186/s12938-019-0647-0

Nečas, D., & Klapetek, P. (2012). Gwyddion: An open-source software for SPM data analysis. *Central European Journal of Physics*, *10*(1), 181–188. https://doi.org/10.2478/s11534-011-0096-2

Patel, D., Zamboulis, D. E., Spiesz, E. M., Birch, H. L., Clegg, P. D., Thorpe, C. T., & Screen, H. R. C. (2021). Structure-function specialisation of the interfascicular matrix in the human achilles tendon. *Acta Biomaterialia*, *131*, 381–390. https://doi.org/10.1016/j.actbio.2021.07.019

Payne, K. J., & Veis, A. (1988). Fourier transform ir spectroscopy of collagen and gelatin solutions: Deconvolution of the amide I band for conformational studies. *Biopolymers*, *27*(11), 1749–1760. https://doi.org/10.1002/bip.360271105

Querido, W., Kandel, S., & Pleshko, N. (2021). Applications of vibrational spectroscopy for analysis of connective tissues. *Molecules*, *26*(4). https://doi.org/10.3390/molecules26040922

Quigley, A. S., Bancelin, S., Deska-Gauthier, D., Légaré, F., Kreplak, L., & Veres, S. P. (2018). In tendons, differing physiological requirements lead to functionally distinct nanostructures. *Scientific Reports*, *8*(1), 1–14. https://doi.org/10.1038/s41598-018-22741-8

Quigley, A. S., Bancelin, S., Deska-Gauthier, D., Légaré, F., Veres, S. P., & Kreplak, L. (2018). Combining tensile testing and structural analysis at the single collagen fibril level. *Scientific Data*, *5*(1), 180229. https://doi.org/10.1038/sdata.2018.229

Tiong, W. H. C., Damodaran, G., Naik, H., Kelly, J. L., & Pandit, A. (2008). Enhancing amine terminals in an amine-deprived collagen matrix. *Langmuir*, *24*(20), 11752–11761. https://doi.org/10.1021/la801913c

Wiens, R., Findlay, C. R., Baldwin, S. G., Kreplak, L., Lee, J. M., Veres, S. P., & Gough, K. M. (2016). High spatial resolution (1.1 μm and 20 nm) FTIR polarization contrast imaging reveals pre-rupture disorder in damaged tendon. *Faraday Discussions*, *187*, 555–573. https://doi.org/10.1039/c5fd00168d

Zhang, S., Ju, W., Chen, X., Zhao, Y., Feng, L., Yin, Z., & Chen, X. (2022). Hierarchical ultrastructure: An overview of what is known about tendons and future perspective for tendon engineering. *Bioactive Materials*, *8*(March 2021), 124–139. https://doi.org/10.1016/j.bioactmat.2021.06.007

Chapter 5. Ultrastructural and SINS analysis of the cell wall integrity response of *Aspergillus nidulans* to the absence of galactofuranose

5.1 Preface

The work presented in Chapter 5 is a peer-reviewed article published in the journal Analyst:

Bakir, G., Girouard, B. E., Johns, R. W., Findlay, C. R.-J., Bechtel, H. A., Eisele, M., Kaminskyj, S. G. W., Dahms, T. E. S., Gough, K. M. (2019). Ultrastructural and SINS analysis of the cell wall integrity response of Aspergillus nidulans to the absence of galactofuranose. The Analyst, 144(3), 928–934.

Here, we showed the first SINS results from the *A. nidulans* cell wall at the nanoscale (~30 nm). The diffraction limit is finally broken with the AFM tip limited spatial resolution. Over the past 15 years, members of the Gough group have worked with various fungi and IR techniques in an effort to understand the fungal cell structure and biochemical composition. Fungi have different impacts on humans and the environment, positive (biotechnology) or negative (pathogenicity & toxicity). Besides their advantages in the industry (winemaking, brewing and baking), it is essential to control their activities and growth to prevent the spread of diseases they may cause to humans and the environment. In 2007, the group achieved the first synchrotron FTIR data acquisition from hyphae of *Aspergillus, Neurospora* and *Rhizopus* (Szeghalmi, Kaminskyj, & Gough, 2007). In contrast to older areas, where cells are vacuolated, FTIR spectra reveal that the cytoplasm close to the apical tip contains more organelles rich in protein and membranes. Following this study, they compared the spectra of hypha and spore from *Neurospora* and *Rhizopus* with synchrotron FTIR

(Jilkine et al., 2008). While results showed biochemical changes in hyphae during sporulation and susceptibility to altered pH of growth medium, they only provided information about the entire cell content. Synchrotron FTIR provides a biochemical profile of proteins, lipids, carbohydrates and other cell contents; however, these can be obtained with, at best, a diffraction-limited spatial resolution of around 3 μm at the shorter wavelengths. Thus, it is impossible to distinguish between the cytoplasm and cell wall components with this technique (Kaminskyj et al., 2008). Isenor et al. (2010) used FTIR and Raman to characterize *Curvularia protuberata* hyphae, comparing the biochemical composition of geothermal and non-geothermal isolates grown in culture. Single point IR spectra acquired with a synchrotron light source and FTIR-FPA (64x64) imaging results allowed the first direct observation of crystalline deposits of mannitol in the geothermal intact hyphae thought to play a protective role. However, these results were again from both the cytoplasm and cell wall. As fungi have different components, ultrastructure and activities at different cellular levels (from cell wall to organelle), acquiring data from the entire cell does not provide sufficient information from the cell wall. To overcome this problem, Prusinkiewicz et al. (2012) and Rak et al. (2014) used different imaging techniques: Surface Enhanced Raman Scattering (SERS) imaging and X-ray microfluorescence (μXRF) imaging, respectively. Although the synthesis of Au nanoparticles (AuNPs) was successful and SERS spectra were obtained from the *A. nidulans* hyphae surrounded by AuNPs, spectra were not sufficiently consistent for useful analysis. The μXRF data of *A. nidulans* highlighted features of gene knockout phenotypes. The absence of gene *ugeA*, responsible for galactose metabolism, and gene *ugmA*, responsible for the biosynthesis of minor cell wall components, resulted in changes in the morphology of the fungi. Although the *ugmA*Δ has the thickest cell wall section, μXRF results suggested that this wall is significantly damaged, permitting cell component leakage. This study highlighted the necessity

for further analysis and characterization of wild type and the mutants of *A. nidulans,* with the focus on spectra from the cell wall only. This was achieved with near-field IR spectroscopy as presented in this Chapter.

This project has been ongoing since 2014, and most of the experiments were conducted in collaboration with our partners, except for the infrared spectroscopy. The first SINS data were collected on samples prepared by Dr. Gough, in-person with Dr. Dahms and Dr. Kaminskyj in 2014. Additional spectra were obtained by Dr. Gough, on subsequent in-person trips in 2015 with some assistance from Findlay, Bechtel and Johns. In 2018, Bakir took over the responsibility of processing all the data collected until that point. Additionally, Bakir contributed to the literature research to identify previously assigned bands associated with cell wall components. After completing the data processing, Bakir conducted a thorough analysis of all spectra collected to best assign the bands to their respective components. This in-depth analysis was essential for gaining insights into the composition and structure of the samples under investigation. The first draft of the manuscript was prepared by Bakir and Gough with the assistance of Girouard in figure generation. All authors reviewed the manuscript, offered comments for editing original and revised versions, and approved the final version of manuscript.

5.2 Abstract

With lethal opportunistic fungal infections on the rise, it is imperative to explore new methods to examine virulence mechanisms. The fungal cell wall is crucial for both the virulence and viability of *Aspergillus nidulans*. One wall component, Gal*f*, has been shown to contribute to important fungal processes, integrity of the cell wall and pathogenesis. Here, we explore gene deletion strains lacking the penultimate enzyme in Gal*f* biosynthesis (*ugmAΔ*) and the protein that

transports Gal*f* for incorporation into the cell wall (*ugtAΔ*). In applying gene deletion technology to the problem of cell wall integrity, we have employed multiple micro- and nano-scale imaging tools, including confocal fluorescence microscopy, electron microscopy, X-Ray fluorescence and atomic force microscopy. Atomic force microscopy allows quantification of ultrastructural cell wall architecture while near-field infrared spectroscopy provides spatially resolved chemical signatures, both at the nanoscale. Here, for the first time, we demonstrate correlative data collection with these two emerging modalities for the multiplexed *in situ* study of the nanoscale architecture and chemical composition of fungal cell walls.

5.3 Introduction

Invasive opportunistic fungal infections are becoming increasingly prevalent in hospital patients, particularly those with cancer who receive immunosuppressive medications, those with HIV who are treated with broad-spectrum antibiotics, and those receiving organ and hematopoietic stem cell transplants, catheters, or prosthetics (Fuchs & Mylonakis, 2009; Valiante et al., 2015; Yoshimi et al., 2016). Invasive aspergillosis, caused by *Aspergillus* spp., arises in a significant portion of such patients, resulting in increased hospital readmissions, duration of stay and mortality (Zilberberg et al., 2018).

The virulence and viability of opportunistic fungal pathogens is directly dependent on the biosynthesis, architecture, composition, and integrity of their fungal cell walls, which surround, support, and protect the cell and mediate interactions with the environment. The cell wall integrity (CWI) signalling pathway regulates cell wall biosynthesis as well as the cell division cycle, allowing fungal cells to coordinate responses to a diverse set of adverse conditions (Dagley et al.,

2011; Latgé, 2007). Accordingly, these walls and pathways have long been prime targets for the development of antifungal drugs (de Groot et al., 2009; Perfect, 2005).

Like all fungi, *Aspergillus* cell walls are a complex matrix of chitin fibrils, α- and β-glucans, galactomannans, other sugars, proteins and glycoproteins (Latgé et al., 1994; Valiante et al., 2015). Galactofuranose (Gal*f*), a polysaccharide and glycoconjugate component, is a minor component of the cell wall by weight. Nonetheless, Gal*f* is important for fungal growth, adhesion, morphogenesis, wall architecture, spore development and pathogenesis. It is often found in *Aspergillus* fungal-type galactomannan (Latgé et al., 1994) and glycoproteins (e.g. O-mannose glycans, *N*-glycans) which modify extracellular enzymes and cell wall proteins (Goto, 2007; Tefsen et al., 2012; Wallis, 2001). UDP-galactopyranose mutase catalyzes the final step in UDP-Gal*f* biosynthesis while the UDP-galactofuranose transporter moves Gal*f* out of the cell for incorporation into the cell wall. Gene deletion strains *ugmAΔ* (El-Ganiny et al., 2008) and *ugtAΔ*(Afroz et al., 2011), which lack the mutase catalyst and transporter enzymes, respectively, were developed to explore the possible role of Gal*f* in CWI. Interestingly, whole cell ELISA quantification and total immunofluorescence intensity of *ugmAΔ* showed higher levels of α-glucan, controlled by CWI pathways, and lower levels of β-glucan compared to wild type (Alam et al., 2014). Both gene deletion strains were more susceptible to caspofungin (which inhibits β-glucan synthesis), while the sensitivity to Calcofluor and Congo red (which bind to chitin) was similar to that of wild type (Afroz et al., 2011; Alam et al., 2012, 2014).

We have imaged fungi and their cell walls in multiple ways, including confocal fluorescence microscopy, scanning and transmission electron microscopy (SEM, TEM)(Afroz et al., 2011; Alam et al., 2012, 2014; El-Ganiny et al., 2008; Paul et al., 2011), atomic force microscopy (AFM), force spectroscopy (FS) (Paul et al., 2011), and X-Ray fluorescence (Rak et

al., 2014). We next sought spatially-resolved chemical imaging of the cell wall using vibrational spectra of hyphae, *in situ*. Information obtained from vibrational spectroscopy (Infrared and Raman) has enabled us to clarify distinctions among species, including differing effects of pH and temperature stress on mature hypha (Kaminskyj et al., 2008; Szeghalmi, Kaminskyj, & Gough, 2007). Growing tips and sporulating hyphae have been characterized (Jilkine et al., 2008), along with the identification and spatial location of secondary metabolites (Isenor et al., 2010b; Liao et al., 2010). Our efforts to obtain vibrational spectroscopic signatures from cell walls have proved challenging, as the wall is typically only tens of nm thick, with a composition that changes along the length behind the growing tip during maturation. Neither whole cell Fourier-transform infrared (FTIR) imaging (Jilkine et al., 2008; Kaminskyj et al., 2008; Szeghalmi, Kaminskyj, & Gough, 2007) nor surface enhanced Raman spectroscopy (Prusinkiewicz et al., 2012b; Szeghalmi, Kaminskyj, Rösch, et al., 2007) were successful. To address this problem, we chose a novel correlative approach that would allow us to probe morphology and cell wall ultrastructure *via* AFM, and explore the spectrochemical composition of the cell wall at nano-scale spatial resolution, *viz*. near-field IR.

Synchrotron infrared nanospectroscopy (SINS) at the Advanced Light Source (ALS) illuminates an AFM tip with synchrotron infrared radiation which is used to probe a target (Bechtel et al., 2014). Thus, SINS enables AFM imaging and near-field broadband infrared spectroscopy with a tip-limited spatial resolution of < 30 nm, to simultaneously examine spatially-resolved envelope ultrastructure and chemical composition at high resolution. This is a proven technique; however, the majority of studies have been on hard, mostly inorganic materials, with only a few focussing on biological targets, and most of the latter are on purified nano-size components(Berweger et al., 2013; Govyadinov et al., 2013; Muller et al., 2015; Qin et al., 2016;

Wiens et al., 2016a) . The tip-substrate coupling required to obtain scatter is weaker for soft organic materials (Keilmann & Hillenbrand, 2004).

Here we report the first near-field infrared study of chemical differences in the cell walls of wild type *A. nidulans* and the two gene deletion strains, *ugmAΔ* and *ugtAΔ.* Our results illustrate how the combined results of AFM (and potentially AFM-FS) data with the spectrochemical information obtained from near-field infrared spectroscopy can open new avenues for the exploration of cell wall function and composition, *in situ*, at the nanoscale.

5.4 Methods

5.4.1 Strains and culture conditions.

Preparation of wild type *A. nidulans* (*A1149*) and gene deletion strains *ugmAΔ* and *ugtAΔ* was similar to that previously described (Jilkine et al., 2008; Rak et al., 2014). Spores from each strain were streaked onto freshly prepared potato dextrose agar (PDA) in Petri dishes, which were sealed and incubated at 37°C for 24-48 hours to yield mature, sporulating colonies. Several μL of ultrapure water was pipetted onto a freshly prepared gold-coated silicon wafer (AuSi, ~1 cm^2) fixed to a glass microscope slide with double-sided tape. A cube of sterile PDA (~3mm) was pressed into a mature colony to pick up spores and then placed, spore side down, onto the water droplet. The slide assembly was sealed in a humid environment and incubated for 24 to 36 hours. Gene deletion strains grew much more slowly and required longer incubation times. Under these conditions, spores germinated and the emerging hyphae grew out beyond any PDA outwash and onto the pristine gold surface. Once there was sufficient growth, slides were snap frozen at -80 °C, and then air-dried for at least 24 hours. The residual PDA block was peeled off, leaving an imprint,

with hyphae for imaging at the periphery (ESI Figure 1A). Even dried, the residual PDA block was at least 1 mm thick, and would have impeded SINS analyses.

Fresh samples of *A1149* and *ugmAΔ* were prepared for each of three SINS experiments at ALS; *ugtAΔ* was analysed during the final data collection session. Multiple points on several hyphae were analysed each time. Similar spectra were acquired at Neaspec, Germany, using their Neaspec nano-FTIR spectroscopy system on one sample of each strain, at points very close to those initially examined with SINS at ALS.

5.4.2 AFM imaging.

AFM was performed on the correlative instrument prior to SINS. An AuSi wafer with hyphae was taped to a metal chuck (ESI Figure 1B) and placed in the sample chamber; the SINS AFM unit was mounted above. Hyphae were first viewed by bright-field to identify suitable targets. AFM images were collected in tapping mode using high resonant frequency platinum silicide probes (PtSi-NCH, NanoSensors) with a nominal resonant frequency of 330 kHz and nominal spring constant of 42 N m^{-1}. The AFM image was collected across the region of interest, providing height, width and ultrastructural data as well as a nm-scale guide for SINS data collection.

5.4.3 SINS spectral collection.

The SINS spectra were collected at points of interest identified in each AFM image. SINS scans were co-added for about 15 minutes to ensure good signal to noise ratio (SNR). Although the ALS ring runs in continuous top-up mode, maintaining a current of 500 mA, the background varied over time. The metal-coated tips are very delicate: minute alterations in the tip coating and

adherence of particles change the scattering properties. Contamination occurred more often during lengthy AFM topographic scans of the soft protein/carbohydrate hyphal surfaces. Accordingly, a fresh background spectrum was acquired at a clean gold surface after every few spectra, to ensure that sample spectra were consistent with reference signals. Tip quality always degraded over time and tips had to be replaced every day or two.

5.4.4 Neaspec spectral collection.

In this system, the AFM tip is illuminated with a laser-based broadband mid-IR nano-FTIR illumination unit to perform nanoscale infrared spectroscopy. The spectra measured at Neaspec, GmbH were recorded within less than 5 min at a spectral resolution of 8.3 cm^{-1}, normalized to a background scan acquired on the gold substrate. All spectral data had a zero-fill factor of 4, so that the final spectra were saved at a nominal spectral resolution of 2.1 cm^{-1}.

5.4.5 Processing to obtain near-field IR spectra.

Both near-field methods employ the scattering Scanning Near-field Optical Microscopy (sSNOM) arrangement whereby mid-IR light illuminates an AFM tip operated in tapping mode and the second order back-scattered light is recorded. Using interferometric detection schemes, (nano-FTIR) amplitude, A(ν), and phase, $\varphi_2(\nu)$, spectra were obtained with nanometer spatial resolution from the complex-valued second order scattering coefficient, (σ_2) (Bechtel et al., 2014; Mastel et al., 2015; Wiens et al., 2016b), given by Equation5.1:

$$\boldsymbol{\sigma_2(\nu)} = \mathrm{A_2}(\boldsymbol{\nu})\mathrm{e}^{\boldsymbol{i\{\varphi(\nu)\}}} \qquad 5.1$$

The SINS infrared absorbance spectrum was obtained by taking a ratio of this term against a background signal, collected at a near-by clean surface on the gold-coated wafer, and then extracting the imaginary component according to Equation (5.2 :

$$\mathrm{Im}\{\boldsymbol{\sigma_2}(\nu)\} = \frac{A_2(\text{hypha}, \nu)}{A_2(\text{gold}, \nu)} \sin[\varphi(\text{hypha}, \nu) - \varphi(\text{gold}, \nu)] \qquad (5.2)$$

The most recent background spectrum was used in each case. Where two backgrounds (one before and one after) were available, both were evaluated and the better spectrum (good signal to noise, flat baseline) was selected.

Post-processing of Neaspec data was done with neaPLOTTER software (Neaspec GmbH, Germany), which effectively performs the same mathematical procedures as above to yield near-field IR absorbance spectra.

5.5 Results and Discussion

5.5.1 Bright-field and TEM images

Representative images clearly show the altered growth habits of the gene deletion strains, (**Figure 5.1**A). Bright field images show the long, unbranched hyphae typical of the fast-growing wild type strain, *A1149*, which grew several hundred microns in 24 hours. In comparison, hyphae from gene deletion strains were, as expected, shorter, thicker and highly branched (Afroz et al., 2011; Alam et al., 2012, 2014; El-Ganiny et al., 2008; Paul et al., 2011). Liquid spread in a thin pool from the PDA block, appearing yellow in the bright field images of strains. Hyphae were located mainly within the residual PDA traces. Only a few hyphae extended beyond the media,

and of these only a few lay against the AuSi surface; the latter were suitable for SINS data collection.

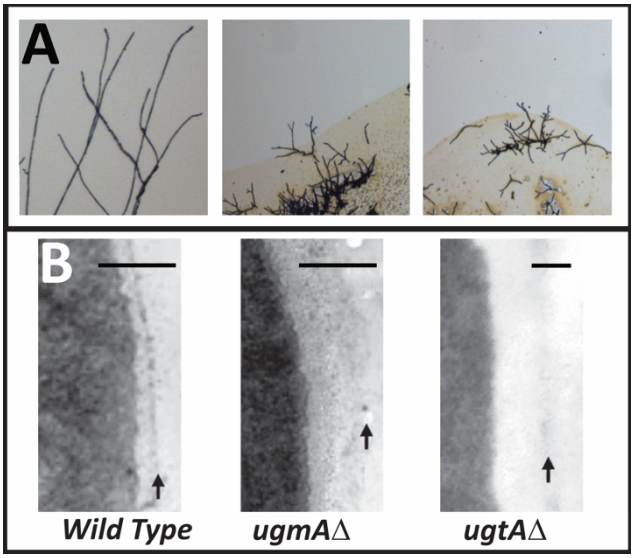

Figure 5.1 Images of hyphae, right to left, *A1149*, *ugmAΔ* and *ugtAΔ*, respectively A) Bright-field images of strains on AuSi wafers for AFM and SINS data collection, photographs at 50x. B) TEM of cell walls (adapted from refs. (Afroz et al., 2011 and El-Ganiny et al., 2008). Arrows denote dark outer edge of walls. Scale bars in B = 100 nm.

TEM images (**Figure 5.1**B) have shown that *A1149* walls are ~50 nm thick, whereas those of *ugmAΔ* and *ugtAΔ* are three to four times thicker (Afroz et al., 2011; Alam et al., 2012, 2014; El-Ganiny et al., 2008; Paul et al., 2011). Edges of the walls (arrows in Fig. 51B) are delineated by electron-dense material. The *ugmAΔ* and *ugtAΔ* cytoplasm appeared to be wild type, but the lack of Gal*f* altered the cell wall and, presumably, its composition (Afroz et al., 2011; El-Ganiny et al., 2008). The *ugmAΔ* cell wall appeared to be less well organized than wild type; the dark outer layer that defined the wall edge was broken and uneven. Total lack of dark layering within the wall of the *ugtAΔ* strain indicated significantly altered internal composition. A plausible explanation is that this strain has less protein and more carbohydrate, which does not stain strongly (Alam et al.,

2014); alternatively, there could be some protein, albeit more thinly dispersed in a less well ordered wall. TEM images provide high spatial resolution information on cross sections, but minimal morphological and chemical analyses.

5.5.2 Reproducibility of near-field IR Data

The goal was to obtain near field infrared spectra of the cell wall, uncontaminated by the cellular contents within, making it critical to acquire reproducible data. The challenge included obtaining many spectra in a limited time frame, while samples were relatively fresh. The spatial resolution afforded by near field IR increased the need for many replicate spectra, which was time consuming given the low SNR, at 8 to 18 minutes per spectrum. A second challenge was the limitation imposed by the spectroscopic probe itself. Here, we report steps taken to ensure quality and reproducibility of data.

5.5.3 AFM and near-field IR of wild type hyphae and exudate.

The best AFM images are typically acquired from fixed hyphae with good turgor, so that the AFM tip probes only the topographical surface (Paul et al., 2011), excluding contributions from interior structures, but hyphae for SINS were prepared by freezing unfixed hyphae. Furthermore, high resolution AFM imaging would require longer collection times, during which the tip could be damaged before acquisition of SINS data. For proof of principle, the most important consideration was the reproducibility of the near field IR data itself; thus, most AFM images were acquired as surveys for SINS targets, using the PtSi probes.

AFM images of typical targets for near field IR recorded with the SINS instrument showed that wild type hyphae had retained a cylindrical, tubular form, with a maximum height of 400-500

nm along the centre (**Figure 5.2**A). SINS spectra were acquired from the centre of the mature hyphal wall, some 50-100 µm behind the growing tips, from multiple hyphae (**Figure 5.2**B). Spectra in this and other figures were displayed on common scale, and offset for clarity. Note that total intensities of different spectra depend in part on the strength of the tip-substrate coupling, so that the absolute intensities cannot be quantified. However, relative intensities within spectra depend on amounts of the individual functional groups present in the probed volume.

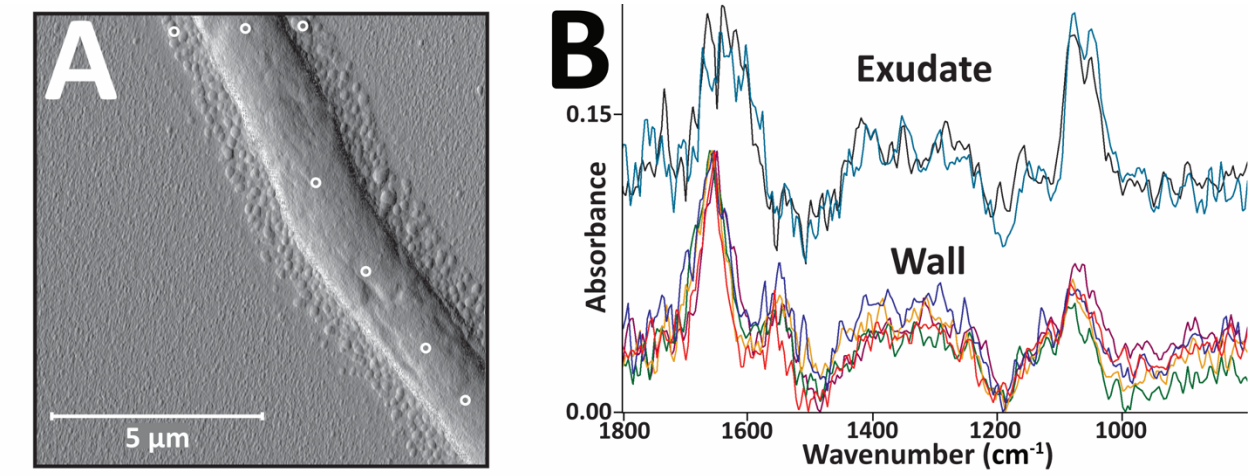

Figure 5.2 AFM image (tapping amplitude) of an *A1149* hypha and associated SINS spectra. A) AFM image recorded with 512 x512 pixel resolution, shows mature cell wall and dried droplets (30 – 150 nm height). B) SINS spectra from points along mature walls and at putative exudate points (white circles). Spectra have been offset for clarity.

Though individual spectra were noisy, the profiles were very similar to each other and unlike those from far field FTIR experiments (Jilkine et al., 2008; Kaminskyj et al., 2008; Szeghalmi, Kaminskyj, & Gough, 2007). In far-field, the amide I and II bands around 1650 and 1545 cm^{-1} were much more intense than those of the carbohydrate region (900-1200 cm^{-1}). The latter region always presents as a group of overlapping bands, but the number and relative intensity of bands in the SINS spectra were different, *vide infra*. Since the fungal cell wall is rich in

carbohydrates, the increased carbohydrate signal was good evidence that the SINS method was indeed probing the surface, with an estimated voxel edge of 30-40 nm.

Fungi interact with their surroundings bidirectionally, exuding materials to test for nutrients, and imbibing nutrients. AFM of this wild type hyphae showed what appeared to be minute droplets of dried liquid, which were tentatively ascribed to dried exudate. Spectra recorded at random spots were similar, showing both amide and carbohydrate bands. However, this phenomenon was only observed for one hypha out of three different sample preparations and several hyphae observed in each case. Detailed band assignments were not attempted; we concluded that this was a sample preparation issue, possibly due to cell rupture, which we will investigate in future.

5.5.4 Cell thickness and reproducibility.

For this study, multiple hyphae from 6 separate preparations of wild type and *ugmAΔ* were studied over three different ALS synchrotron experiments. The gene deletion strains were thicker than wild type, with maximum heights of > 1 μm. The hyphae of the *ugmAΔ* strain is very slow growing; even after 36 hours of incubation, the hyphae barely extended beyond the vestiges of dried agar (**Figure 5.1**A). The quick freeze and thaw step for mature hyphae on AuSi caused some hyphae to collapse slightly, creating uneven heights reflecting underlying organelles, as seen for a hyphal branch of *umgAΔ* (**Figure 5.3**A). Even at the thinnest locations, the height was ~400 nm above the AuSi wafer. Spectra acquired at points along hyphae in collapsed regions with little underlying structure (**Figure 5.3**. B, C) were very similar. The example spectra shown here were acquired from two different hyphae, on different days, by two different operators at approximately the same regions.

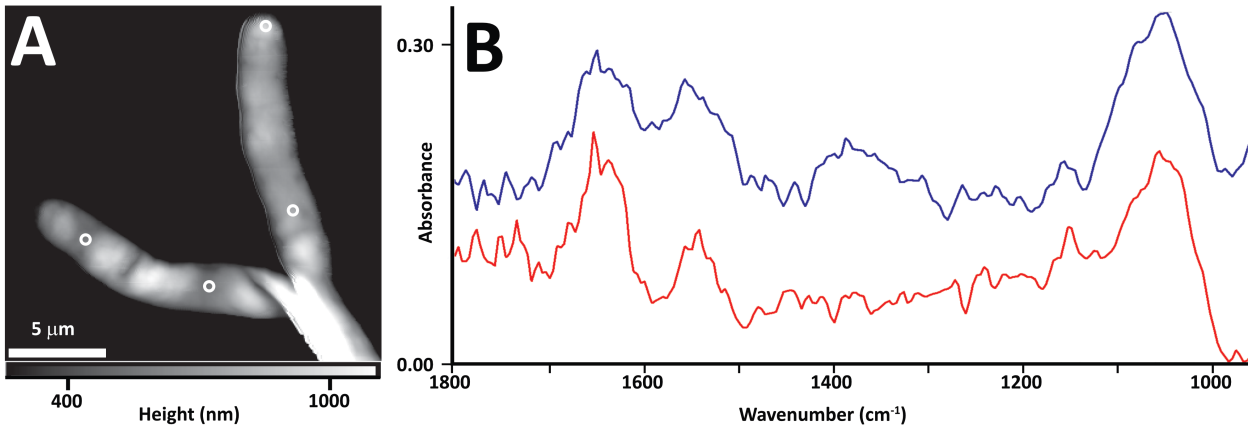

Figure 5.3 AFM and SINS spectra of *ugmAΔ* hyphal branch. A) AFM topography and selected locations for SINS data, at points ~ 400 nm in height. B) SINS spectra from four points, recorded on different days, by 2 different operators, were found to be reliably similar, with proper sample preparation and spectral locations selected as shown above.

5.5.5 Reproducibility on different instruments.

To test this further, near field infrared spectra were obtained from the same hyphae at nearly the same locations, with SINS and with a Neaspec instrument, for each of the three strains. Both SINS and Neaspec instruments incorporate the sSNOM approach, the SINS illuminated with synchrotron light and the Neaspec with the broadband mid-infrared nano-FTIR illumination unit. The similarity between the spectra is sufficient to give confidence in the main features in all spectral profiles (**Figure 5.4**).

5.5.6 SINS spectra reveal effects of Gal*f* deletion in cell walls

SINS spectra were collected over multiple experiments at ALS. Spectra representative of the three fungal strains, shown in **Figure 5.4**, can now be used for a more detailed spectrochemical analysis. Given that spectra from similar points had similar profiles, individual spectra from

comparable locations were summed to improve SNR for all three strains. The only difference introduced by gene deletions was the absence of Galf (Afroz et al., 2011; Alam et al., 2012, 2014; El-Ganiny et al., 2008; Paul et al., 2011) and, as a minor component, its absence should not have a noticeable impact on the wall spectra. Nonetheless, there were significant spectral differences that could aid in our understanding of the downstream impact of the gene deletions.

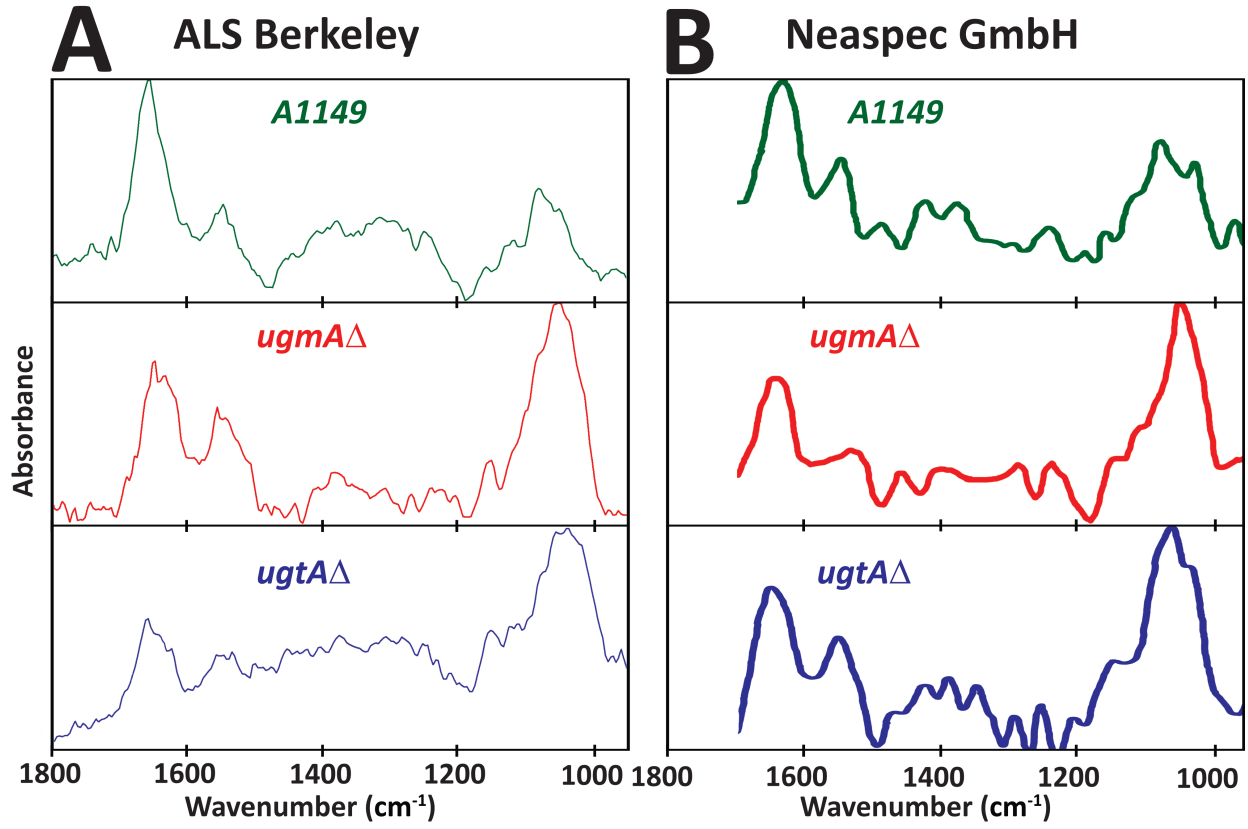

Figure 5.4 Near-field infrared spectra of mature hyphal walls from wild type, ugmAΔ and ugtAΔ strains. A) SINS spectra are sums of 7-10 spectra, acquired from similar regions, different preparations and dates, and summed for improved SNR. B) Spectra from Neaspec were acquired from one of each of the three strains at approximately the same locations as probed with SINS at ALS.

In an AFM-FS study of surface architecture, the *ugmAΔ* strain was previously found to be less rough (subunit size ~3x greater than in wild type), and less well ordered, with an elastic

modulus one tenth that of normal wild type hyphae (Paul et al., 2011). This fact, and the loss of viscoelasticity, indicated that, despite being a minor wall component, Gal*f* likely has a role in cross-linking.

The first obvious difference between the spectra of *wild type* and *ugmAΔ* and *ugtAΔ* gene deletion strains is in the relative intensities of the amide (I & II) and carbohydrate bands (Table 5.1). The amide bands are the most prominent in the wild type spectra, and much weaker in those of the *ugmAΔ* and *ugtAΔ.* The TEM images showed that the cell walls of the gene deletion strains are 3 to 5 times thicker than the wild type (**Figure 5.1**); decreased staining had been interpreted as a decrease in protein content of the cell walls, with *ugtAΔ* having the least. Reduction of protein content in these strains could explain the reduction in the amide band intensities; however, the N-acetyl groups in chitin also absorb in this region, with band maxima reported to be ~1640 and 1540 cm^{-1} (Table 5.1). In fungal cell walls, chitin is located at the base of the wall, adjacent to the lipid membrane of the encapsulated cells (Fuchs & Mylonakis, 2009; Valiante et al., 2015; Yoshimi et al., 2016). The thin wall of wild type hyphae (estimated to be 25 – 50 nm) could potentially allow chitin acetamide bands to appear in the SINS spectra but most likely at longer wavelengths than protein. The amide I band maximum in *A1149* is observed at 1655 cm^{-1}, best assigned as α-helical protein rather than chitin. In contrast, the increased wall thickness would preclude detection of the underlying chitin layer in *ugmAΔ* and *ugtAΔ.* The significant loss of intensity at this region in spectra of the gene deletion strains is therefore attributed to lack of protein within cell wall itself. This spectrochemical result is consistent with the physical structure, and further confirms that the SINS spectra are probing the surface of the hyphae.

Table 5.1 NFIR Band positions (cm^{-1}) and assignments in NFIR of *A. nidulans* strains

A1149	*ugmAΔ*	*ugtAΔ*	Assignment
1049	1020-1040	1020-1040	α, β-glucan[a,b]
1079			ν(CO), β-glucan[a]
1116-1130		1113-1125	ν (CC), C-O-C chitin, β-glucan[a,c]
1157	1153	1157	ν (COC), ν (CC) α-glucan[a]
1546	1549	1550	Amide II, β-glucan [b,d]
	1630	1623	ν (C=O) chitin (acetamide) [a,b,d]
1655	1650	1650	Amide I [a,b.d]

[a](Šandula et al., 1999), [b](Hromádková et al., 2003), [c](Mehranian et al., 2017), [d](Zechner-Krpan et al., 2010)

Overall, spectra of both gene deletion strains exhibit much higher relative intensity than *wild type* in the 1150 to 900 cm^{-1} region, variously attributed to carboxymethyl groups of glucans (Hromádková et al., 2003; Mehranian et al., 2017; Šandula et al., 1999; Zechner-Krpan et al., 2010). Amide and chitin bands are well known; however, literature assignments for glucan bands are hampered by problems with sample consistency. Literature values reported for these compounds are often based on partially refined extracts from various natural sources, ranging from shellfish and insects to fungi and yeasts. Our analyses of the spectra in the 1150-900 cm^{-1} region are based on peak assignments from spectra of chitin and α- and β-glucans, purified from *A. niger* (Šandula et al., 1999), *S. cerevisiae* (Hromádková et al., 2003; Šandula et al., 1999; Zechner-Krpan et al., 2010), a moth (*Ephestia kuehniella* Zeller) and commercial shrimp chitin (Mehranian et al., 2017). The *ugmAΔ* and *ugtAΔ* strains have significantly lower peaks than wild type at 1079 cm^{-1} and significantly higher peaks than wild type at 1130-1155 cm^{-1}. These absorbance bands are assigned to β-glucan and α-glucan, respectively (Table 5.1). Thus the SINS spectra provide direct evidence that gene deletions preventing Gal*f* from contributing to wall structure induce a response that preferentially increases the α-glucan content.

One of the major advantages of opportunistic fungi is their ability to respond dynamically to threats through pathway regulation cells (Fuchs & Mylonakis, 2009; Valiante et al., 2015;

Yoshimi et al., 2016). Cell wall stresses are known to activate genes responsible for the synthesis of cell wall components such as chitin or α-(1,3) glucan (Damveld et al., 2005; Fujioka et al., 2007; Katayama et al., 2015; Oka, 2018; Park et al., 2016). Gal*f* is only a minor component in cell wall, but possible roles for Gal*f* in cell wall synthesis have been noted by us and others (Afroz et al., 2011; Alam et al., 2012, 2014; Damveld et al., 2008; El-Ganiny et al., 2008; Latge, 2009; Paul et al., 2011; Pedersen & Turco, 2003; Schmalhorst et al., 2008). Based on the cell wall remodelling in strains deficient in Gal*f*, we originally hypothesized that its absence would alter not only the organization of cell wall components, but also their biochemical composition through CWI and other signalling pathways (Afroz et al., 2011; Alam et al., 2012, 2014; El-Ganiny et al., 2008; Paul et al., 2011).

The typical CWI response is to upregulate certain cell wall components in a compensatory fashion (Valiante et al., 2015). AFM and TEM of these strains had shown that an absence of Gal*f* significantly altered the cell wall architecture, composition, function and integrity. Nonetheless, this CWI response failed to protect it against certain antifungal drugs (Afroz et al., 2011; Alam et al., 2012, 2014), underscoring the importance of Gal*f* in cell wall maturation and hyphal extension. The SINS spectra show increases in the α-glucan wall content in the *ugmAΔ* and *ugtAΔ* gene deletion strains, consistent with our previous studies (Alam et al., 2014) and an *Aspergillus* CWI response (Valiante et al., 2015).

5.6 Conclusions

Next-wave single cell analyses must include the production of highly resolved structural and compositional analyses of biological specimens. For dried samples, AFM reports on gross morphology, nanoscale surface architecture and roughness that can be further articulated by near-

field FTIR surface chemical analysis. Here, we have demonstrated how SINS offers powerful multiplexed data with nm-scale resolution that complements and clarifies changes in fungal cell wall integrity induced by genetic alteration. These methods, used in conjunction with existing tools, offer an exciting new way to study previously inaccessible regions of single cells.

5.7 References

Afroz, S., El-Ganiny, A. M., Sanders, D. A. R., & Kaminskyj, S. G. W. (2011). Roles of the *Aspergillus nidulans* UDP-galactofuranose transporter, UgtA in hyphal morphogenesis, cell wall architecture, conidiation, and drug sensitivity. *Fungal Genetics and Biology*, *48*(9), 896–903. https://doi.org/10.1016/j.fgb.2011.06.001

Alam, M. K., El-Ganiny, A. M., Afroz, S., Sanders, D. A. R., Liu, J., & Kaminskyj, S. G. W. (2012). *Aspergillus nidulans* galactofuranose biosynthesis affects antifungal drug sensitivity. *Fungal Genetics and Biology*, *49*(12), 1033–1043. https://doi.org/10.1016/j.fgb.2012.08.010

Alam, M. K., van Straaten, K. E., Sanders, D. A. R., & Kaminskyj, S. G. W. (2014). *Aspergillus nidulans* cell wall composition and function change in response to hosting several Aspergillus fumigatus UDP-galactopyranose mutase activity mutants. *PLoS ONE*, *9*(1). https://doi.org/10.1371/journal.pone.0085735

Bechtel, H. A., Muller, E. A., Olmon, R. L., Martin, M. C., & Raschke, M. B. (2014). Ultrabroadband infrared nanospectroscopic imaging. *Proceedings of the National Academy of Sciences of the United States of America*, *111*(20), 7191–7196. https://doi.org/10.1073/pnas.1400502111

Berweger, S., Nguyen, D. M., Muller, E. A., Bechtel, H. A., Perkins, T. T., & Raschke, M. B. (2013). Nano-Chemical Infrared Imaging of Membrane Proteins in Lipid Bilayers. *Journal of the American Chemical Society*, *135*(49), 18292–18295. https://doi.org/10.1021/ja409815g

Dagley, M. J., Gentle, I. E., Beilharz, T. H., Pettolino, F. A., Djordjevic, J. T., Lo, T. L., Uwamahoro, N., Rupasinghe, T., Tull, D. L., McConville, M., Beaurepaire, C., Nantel, A., Lithgow, T., Mitchell, A. P., & Traven, A. (2011). Cell wall integrity is linked to mitochondria and phospholipid homeostasis in Candida albicans through the activity of the post-transcriptional regulator Ccr4-Pop2. *Molecular Microbiology*, *79*(4), 968–989. https://doi.org/10.1111/j.1365-2958.2010.07503.x

Damveld, R. A., Franken, A., Arentshorst, M., Punt, P. J., Klis, F. M., van den Hondel, C. A. M. J. J., & Ram, A. F. J. (2008). A novel screening method for cell wall mutants in Aspergillus niger identifies UDP-galactopyranose mutase as an important protein in fungal cell wall biosynthesis. *Genetics*, *178*(2), 873–881. https://doi.org/10.1534/genetics.107.073148

Damveld, R. A., Vankuyk, P. A., Arentshorst, M., Klis, F. M., van den Hondel, C. A. M. J. J., & Ram, A. F. J. (2005). Expression of agsA, one of five 1,3-α-d-glucan synthase-encoding genes in *Aspergillus niger*, is induced in response to cell wall stress. *Fungal Genetics and Biology*, *42*(2), 165–177. https://doi.org/10.1016/j.fgb.2004.11.006

de Groot, P. W. J., Brandt, B. W., Horiuchi, H., Ram, A. F. J., de Koster, C. G., & Klis, F. M. (2009). Comprehensive genomic analysis of cell wall genes in *Aspergillus nidulans*. *Fungal Genetics and Biology : FG & B*, *46*(1), S72–S81. https://doi.org/10.1016/j.fgb.2008.07.022

El-Ganiny, A. M., Sanders, D. A. R., & Kaminskyj, S. G. W. (2008). *Aspergillus nidulans* UDP-galactopyranose mutase, encoded by ugmA plays key roles in colony growth, hyphal

morphogensis, and conidiation. *Fungal Genetics and Biology*, *45*(12), 1533–1542. https://doi.org/10.1016/j.fgb.2008.09.008

Fuchs, B. B., & Mylonakis, E. (2009). Our Paths Might Cross: the Role of the Fungal Cell Wall Integrity Pathway in Stress Response and Cross Talk with Other Stress Response Pathways. *Eukaryotic Cell*, *8*(11), 1616–1625. https://doi.org/10.1128/EC.00193-09

Fujioka, T., Mizutani, O., Furukawa, K., Sato, N., Yoshimi, A., Yamagata, Y., Nakajima, T., & Abe, K. (2007). MpkA-Dependent and -Independent Cell Wall Integrity Signaling in *Aspergillus nidulans*. *Eukaryotic Cell*, *6*(8), 1497–1510. https://doi.org/10.1128/EC.00281-06

Goto, M. (2007). Protein O-glycosylation in fungi: Diverse structures and multiple functions. *Bioscience, Biotechnology and Biochemistry*, *71*(6), 1415–1427. https://doi.org/10.1271/bbb.70080

Govyadinov, A. a, Amenabar, I., Huth, F., & Carney, P. S. (2013). Quantitative Measurement of Local Infrared Absorption and Dielectric Function with Tip-Enhanced Near-Field Microscopy Brief overview of tip-sample inter- action models Spectral resolution and nano-FTIR calibration: Supplement. *The Journal of Physical Chemistry Letters*, Supplement.

Hromádková, Z., Ebringerová, A., Sasinková, V., Šandula, J., Hříbalová, V., & Omelková, J. (2003). Influence of the drying method on the physical properties and immunomodulatory activity of the particulate (1 → 3)-β-D-glucan from Saccharomyces cerevisiae. *Carbohydrate Polymers*, *51*(1), 9–15. https://doi.org/10.1016/S0144-8617(02)00110-8

Isenor, M., Kaminskyj, S. G. W., Rodriguez, R. J., Redman, R. S., & Gough, K. M. (2010a). Characterization of mannitol in *Curvularia protuberata* hyphae by FTIR and Raman spectromicroscopy. *Analyst*, *135*(12), 3249–3254. https://doi.org/10.1039/c0an00534g

Isenor, M., Kaminskyj, S. G. W., Rodriguez, R. J., Redman, R. S., & Gough, K. M. (2010b). Characterization of mannitol in *Curvularia protuberata* hyphae by FTIR and Raman spectromicroscopy. *Analyst*, *135*(12), 3249–3254. https://doi.org/10.1039/c0an00534g

Jilkine, K., Gough, K. M., Julian, R., & Kaminskyj, S. G. W. (2008). A sensitive method for examining whole-cell biochemical composition in single cells of filamentous fungi using synchrotron FTIR spectromicroscopy. *Journal of Inorganic Biochemistry*, *102*(3), 540–546. https://doi.org/10.1016/j.jinorgbio.2007.10.023

Kaminskyj, S., Jilkine, K., Szeghalmi, A., & Gough, K. (2008). High spatial resolution analysis of fungal cell biochemistry - Bridging the analytical gap using synchrotron FTIR spectromicroscopy. *FEMS Microbiology Letters*, *284*(1), 1–8. https://doi.org/10.1111/j.1574-6968.2008.01162.x

Katayama, T., Ohta, A., & Horiuchi, H. (2015). Protein kinase C regulates the expression of cell wall-related genes in RlmA-dependent and independent manners in *Aspergillus nidulans*. *Bioscience, Biotechnology and Biochemistry*, *79*(2), 321–330. https://doi.org/10.1080/09168451.2014.973365

Keilmann, F., & Hillenbrand, R. (2004). Near-Field microscopy by elastic scattering from a tip. *Phil. Trans. R. Soc. Lond. A*, *362*, 787–805.

Latgé, J. P. (2007). The cell wall: A carbohydrate armour for the fungal cell. *Molecular Microbiology*, *66*(2), 279–290. https://doi.org/10.1111/j.1365-2958.2007.05872.x

Latge, J. P. (2009). Galactofuranose containing molecules in *Aspergillus fumigatus*. *Medical Mycology*, *47*(SUPPL. 1), 104–109. https://doi.org/10.1080/13693780802258832

Latgé, J. P., Kobayashi, H., Debeaupuis, J. P., Diaquin, M., Sarfati, J., Wieruszeski, J. M., Parra, E., Bouchara, J. P., & Fournet, B. (1994). Chemical and immunological characterization of

the extracellular galactomannan of *Aspergillus fumigatus*. *Infection and Immunity*, *62*(12), 5424–5433. https://doi.org/10.1128/iai.62.12.5424-5433.1994

Liao, C., Piercey-Normore, M. D., Sorensen, J. L., & Gough, K. (2010). In situ imaging of usnic acid in selected Cladonia spp. by vibrational spectroscopy. *Analyst*, *135*(12), 3242–3248. https://doi.org/10.1039/c0an00533a

Mastel, S., Govyadinov, A. A., de Oliveira, T. V. A. G., Amenabar, I., & Hillenbrand, R. (2015). Nanoscale-resolved chemical identification of thin organic films using infrared near-field spectroscopy and standard Fourier transform infrared references. *Applied Physics Letters*, *106*(2), 1–6. https://doi.org/10.1063/1.4905507

Mehranian, M., Pourabad, R. F., Bashir, N. S., & Taieban, S. (2017). Physicochemical characterization of chitin from the Mediterranean flour moth, Ephestia kuehniella Zeller (Lepidoptera: Pyralidae). *Journal of Macromolecular Science, Part A: Pure and Applied Chemistry*, *54*(10), 720–726. https://doi.org/10.1080/10601325.2017.1332461

Muller, E. A., Pollard, B., & Raschke, M. B. (2015). Infrared chemical nano-imaging: Accessing structure, coupling, and dynamics on molecular length scales. *Journal of Physical Chemistry Letters*, *6*(7), 1275–1284. https://doi.org/10.1021/acs.jpclett.5b00108

Oka, T. (2018). Biosynthesis of galactomannans found in filamentous fungi belonging to Pezizomycotina. *Bioscience, Biotechnology and Biochemistry*, *82*(2), 183–191. https://doi.org/10.1080/09168451.2017.1422383

Park, J., Hulsman, M., Arentshorst, M., Breeman, M., Alazi, E., Lagendijk, E. L., Rocha, M. C., Malavazi, I., Nitsche, B. M., van den Hondel, C. A. M. J. J., Meyer, V., & Ram, A. F. J. (2016). Transcriptomic and molecular genetic analysis of the cell wall salvage response of *Aspergillus*

niger to the absence of galactofuranose synthesis. *Cellular Microbiology*, *18*(9), 1268–1284. https://doi.org/10.1111/cmi.12624

Paul, B. C., El-Ganiny, A. M., Abbas, M., Kaminskyj, S. G. W., & Dahms, T. E. S. (2011). Quantifying the importance of Galactofuranose in *Aspergillus nidulans* hyphal wall surface organization by atomic force microscopy. *Eukaryotic Cell*, *10*(5), 646–653. https://doi.org/10.1128/EC.00304-10

Pedersen, L. L., & Turco, S. J. (2003). Galactofuranose metabolism: A potential target for antimicrobial chemotherapy. *Cellular and Molecular Life Sciences*, *60*(2), 259–266. https://doi.org/10.1007/s000180300021

Perfect, J. R. (2005). Nuances of new anti- Aspergillus antifungals. *Medical Mycology*, *43*(s1), 271–276. https://doi.org/10.1080/13693780400020071

Prusinkiewicz, M. A., Farazkhorasani, F., Dynes, J. J., Wang, J., Gough, K. M., & Kaminskyj, S. G. W. (2012a). Proof-of-principle for SERS imaging of *Aspergillus nidulans* hyphae using in vivo synthesis of gold nanoparticles. *Analyst*, *137*(21), 4934–4942. https://doi.org/10.1039/c2an35620a

Prusinkiewicz, M. A., Farazkhorasani, F., Dynes, J. J., Wang, J., Gough, K. M., & Kaminskyj, S. G. W. (2012b). Proof-of-principle for SERS imaging of Aspergillus nidulans hyphae using in vivo synthesis of gold nanoparticles. *Analyst*, *137*(21), 4934–4942. https://doi.org/10.1039/c2an35620a

Qin, N., Zhang, S., Jiang, J., Corder, S. G., Qian, Z., Zhou, Z., Lee, W., Liu, K., Wang, X., Li, X., Shi, Z., Mao, Y., Bechtel, H. A., Martin, M. C., Xia, X., Marelli, B., Kaplan, D. L., Omenetto, F. G., Liu, M., & Tao, T. H. (2016). Nanoscale probing of electron-regulated structural

transitions in silk proteins by near-field IR imaging and nano-spectroscopy. *Nature Communications*, *7*(1), 13079. https://doi.org/10.1038/ncomms13079

Rak, M., Salome, M., Kaminskyj, S. G. W., & Gough, K. M. (2014). X-ray microfluorescence (μXRF) imaging of *Aspergillus nidulans* cell wall mutants reveals biochemical changes due to gene deletions. *Analytical and Bioanalytical Chemistry*, *406*(12), 2809–2816. https://doi.org/10.1007/s00216-014-7726-7

Šandula, J., Kogan, G., Kačuráková, M., & MacHová, E. (1999). Microbial (1→3)-β-D-glucans, their preparation, physico-chemical characterization and immunomodulatory activity. *Carbohydrate Polymers*, *38*(3), 247–253. https://doi.org/10.1016/S0144-8617(98)00099-X

Schmalhorst, P. S., Krappmann, S., Vervecken, W., Rohde, M., Müller, M., Braus, G. H., Contreras, R., Braun, A., Bakker, H., & Routier, F. H. (2008). Contribution of galactofuranose to the virulence of the opportunistic pathogen *Aspergillus fumigatus*. *Eukaryotic Cell*, *7*(8), 1268–1277. https://doi.org/10.1128/EC.00109-08

Szeghalmi, A., Kaminskyj, S., & Gough, K. M. (2007). A synchrotron FTIR microspectroscopy investigation of fungal hyphae grown under optimal and stressed conditions. *Analytical and Bioanalytical Chemistry*, *387*(5), 1779–1789. https://doi.org/10.1007/s00216-006-0850-2

Szeghalmi, A., Kaminskyj, S., Rösch, P., Popp, J., & Gough, K. M. (2007). Time Fluctuations and Imaging in the SERS Spectra of Fungal Hypha Grown on Nanostructured Substrates. *The Journal of Physical Chemistry B*, *111*(44), 12916–12924. https://doi.org/10.1021/jp075422a

Tefsen, B., Ram, A. F. J., van Die, I., & Routier, F. H. (2012). Galactofuranose in eukaryotes: aspects of biosynthesis and functional impact. *Glycobiology*, *22*(4), 456–469. https://doi.org/10.1093/glycob/cwr144

Valiante, V., Macheleidt, J., Föge, M., & Brakhage, A. A. (2015). The Aspergillus fumigatus cell wall integrity signaling pathway: drug target, compensatory pathways, and virulence. *Frontiers in Microbiology*, *06*(MAR), 1–12. https://doi.org/10.3389/fmicb.2015.00325

Wallis, G. (2001). β-Galactofuranoside glycoconjugates on conidia and conidiophores of *Aspergillus niger*. *FEMS Microbiology Letters*, *201*(1), 21–27. https://doi.org/10.1016/S0378-1097(01)00219-1

Wiens, R., Findlay, C. R., Baldwin, S. G., Kreplak, L., Lee, J. M., Veres, S. P., & Gough, K. M. (2016a). High spatial resolution (1.1 μm and 20 nm) FTIR polarization contrast imaging reveals pre-rupture disorder in damaged tendon. *Faraday Discussions*, *187*, 555–573. https://doi.org/10.1039/c5fd00168d

Wiens, R., Findlay, C. R., Baldwin, S. G., Kreplak, L., Lee, J. M., Veres, S. P., & Gough, K. M. (2016b). High spatial resolution (1.1 μm and 20 nm) FTIR polarization contrast imaging reveals pre-rupture disorder in damaged tendon. *Faraday Discussions*, *187*, 555–573. https://doi.org/10.1039/c5fd00168d

Yoshimi, A., Miyazawa, K., & Abe, K. (2016). Cell wall structure and biogenesis in *Aspergillus* species. *Bioscience, Biotechnology, and Biochemistry*, *80*(9), 1700–1711. https://doi.org/10.1080/09168451.2016.1177446

Zechner-Krpan, V., Petravić-Tominac, V., Gospodarić, I., Sajli, L., Daković, S., & Filipović-Grčić, J. (2010). Characterization of β-glucans isolated from brewer's yeast and dried by different methods. *Food Technology and Biotechnology*, *48*(2), 189–197.

Zilberberg, M. D., Nathanson, B. H., Harrington, R., Spalding, J. R., & Shorr, A. F. (2018). Epidemiology and Outcomes of Hospitalizations With Invasive Aspergillosis in the United

States, 2009–2013. *Clinical Infectious Diseases*, *67*(5), 727–735. https://doi.org/10.1093/cid/ciy181

Chapter 6. *Saccharomyces cerevisiae* cell wall remodeling in the absence of Knr4 and Kre6 revealed by nano-FTIR spectroscopy

6.1 Preface

In this chapter, we used the information gained from the study in Chapter 5 to characterize the yeast cell wall. This manuscript has been submitted to the journal Applied Spectroscopy:

Gorkem Bakir, Tanya E. S. Dahms, Helene Martin-Yken, Hans A. Bechtel, Kathleen M. Gough, Saccharomyces cerevisiae cell wall remodeling in the absence of Knr4 and Kre6 revealed by nano-FTIR spectroscopy*, Applied Spectroscopy (submitted, 25 Jan 2023, the revised version is about to be submitted)*

We concluded in the previous chapter that nano-FTIR is an excellent method of providing information at the nanoscale with a probe voxel dimension of ~25 nm edge and presented direct spectrochemical information from the *Aspergillus nidulans* cell wall (less than 100 nm). In Chapter 6 we used the same technique we developed in the previous chapter and applied to obtain spectrochemical information from another small voxel area, yeast cell wall (~100nm). In this study we looked at different strains with gene deletions and compared with wild type to observe the alterations in their cell wall. We used the table for NFIR band positions (cm^{-1}) and assignments in NFIR of *A. nidulans* strains from Chapter 5 and new reference carbohydrate standards (shown in this chapter) to assign the bands we observed in Near-field IR spectra of *Saccharomyces cerevisiae*. We studied with two mutants lacking protein genes, *kre6Δ* and *knr4Δ*. Kre6 is an integral membrane protein required for biosynthesis of β-1,6-glucan and Knr4 is a cell signaling

protein involved in the control of cell wall biosynthesis The spectra of *kre6Δ* and *knr4Δ* strains showed differences in carbohydrate and protein regions compared to wild type strain. The β-1,6-glucan content is decreased in *kre6Δ*, while all glucan content is decreased in the *knr4Δ* cell wall. These alterations are discussed in detail below. After receiving gene-deleted strains from our collaborator, Bakir cultivated fresh samples at the University of Manitoba and prepared for nano-FTIR analysis. The data were collected by Bakir on-site at ALS, Berkeley, CA, USA. All data were processed and analyzed for band assignments by Bakir. It is important to note that all aspects of this research, including data collection, analysis, and interpretation, were performed solely by Bakir. To complement the study, commercially purchased carbohydrate standards were examined using ATR spectroscopy at the University of Manitoba. The analysis of these standards was also conducted by Bakir. First draft of the manuscript was prepared by Bakir with editing and guidance from Dr. Gough. All authors approved the manuscript before its submission to the journal *Applied Spectroscopy*. All authors are now working on responses to the reviewers comments.

6.2 Abstract

The cell wall integrity (CWI) signaling pathway regulates yeast cell wall biosynthesis, cell division, and responses to external stress. The cell wall, comprised of a dense network of chitin, β-1,3- and β-1,6- glucans, and mannoproteins, is very thin, less than 100 nm. Alterations in cell wall composition may activate the CWI pathway. *Saccharomyces cerevisiae*, a model yeast, was used to study the role of individual wall components in altering the structure and biophysical properties of the yeast cell wall. Near-field Fourier Transform Infrared (FTIR) spectroscopy (nano-FTIR) was used for the first direct, spectrochemical identification of cell wall composition in a background (wild-type) strain and two deletion mutants from the yeast knock-out collection: *kre6Δ*

and *knr4Δ*. Kre6 is an integral membrane protein required for biosynthesis of β-1,6-glucan, while Knr4 is a cell signaling protein involved in the control of cell wall biosynthesis, in particular, biosynthesis and deposition of chitin. Complementary spectral data were obtained with far-field (FF) FTIR, in transmission and with attenuated total reflectance (ATR) spectromicroscopy with 3-10 μm wavelength-dependent spatial resolution. The FF-FTIR spectra of cells and spectra of isolated cell wall components showed that components of the cell body dominated transmission spectra and were still evident in ATR spectra. In contrast, the nano-FTIR at ~25 nm spatial resolution could be used to characterize the yeast wall chemical structure. Our results show that the β-1,6-glucan content is decreased in *kre6Δ*, while all glucan content is decreased in the *knr4Δ* cell wall. The latter may be thinner than in wild type, since not only are mannan and chitin detectable by nano-FTIR, but also lipid membranes and protein, indicative of cell interior.

6.3 Introduction

Saccharomyces cerevisiae, instrumental in brewing and baking, is a model organism for understanding yeast cell wall biology (Lesage & Bussey, 2006). The *S. cerevisiae* cell wall is composed of inner and outer layers. The inner layer consists primarily of β-1,3-glucan chains with β-1,6 branches, and β-1,6-glucan chains; chitin chains at the outer and inner surfaces of this layer confer significant tensile strength though they represent the smallest fraction (~2%) of the cell wall. The outer layer is predominantly comprised of a glycoprotein lattice (mannoprotein) (Orlean, 2012). The strength and elasticity of the yeast cell wall arises from these interwoven macromolecular components which protect the organism from osmotic shock and mechanical stress while maintaining cell shape and enabling cell cycle progression and adhesion (Klis et al.,

2006; Orlean, 2012; Stratford, 1994). The chemical composition of the cell wall is difficult to determine by direct measurement, as it is on the order of 100 nm thick (Lesage & Bussey, 2006; Stratford, 1994).

The cell wall integrity (CWI) signaling pathway plays a critical role in the maintenance and remodeling of the cell wall, particularly during budding and in response to external stress (Dagley et al., 2011; Latgé, 2007; Levin, 2011). In this study, we focus on deletion mutants of two *S. cerevisiae* proteins, Kre6 and Knr4, that are involved in cell wall biogenesis and have homologues across the fungal kingdom. Knr4 and Kre6 mutants were specifically chosen for investigation in this study due to their known roles in cell wall biogenesis and their presence across multiple fungal species, including pathogenic yeasts, indicating their potential significance and similarity in understanding cell wall-related processes.

Kre6 (Killer toxin resistant 6) is a type II integral membrane protein that plays a key role in the biosynthesis of β-1,6-glucan (Kurita et al., 2011; Levin, 2011; Roemer & Bussey, 1991). In *S. cerevisiae,* simultaneous deletion of Kre6 and its homolog Skn1 results in a severe growth defect (Roemer et al., 1993). In *Aureobasidium pullulans*, deletion of two Kre6-like homologs alters the cell wall and cell morphology, and reduces branching and overall production of soluble extracellular β-glucans, without clearly impacting cell viability (Uchiyama et al., 2018). The *Candida albicans* mutant *kre6Δ/Δskn1Δ/Δ* exhibits cell wall abnormalities and greatly diminishes cell growth (Han et al., 2019a). Knr4 is a cell signaling protein involved in the control of cell wall biosynthesis and cell cycle, as well as chitin deposition during vegetative growth and sporulation (Dagkessamanskaia et al., 2001, 2010; Martin et al., 1999; Martin-Yken et al., 2016). In the human fungal pathogen *C. albicans*, Knr4 has two homologs, Smi1 and Smi1B, that are involved in adhesion and antibiotic resistance (Martin-Yken et al., 2018; Nett et al., 2011). These observations

show that Kre6, Knr4, and their homologs have conserved roles in cell wall biogenesis among these fungi.

In the studies of Kre6 (Han et al., 2019b; Kurita et al., 2011; Roemer et al., 1993; Roemer & Bussey, 1991; Uchiyama et al., 2018)and Knr4 (Dagkessamanskaia et al., 2001, 2010; Martin et al., 1999; Martin-Yken et al., 2016, 2018; Nett et al., 2011) above, yeasts and wall composition were investigated by conventional fluorescence staining of cells or by extraction and isolation of components for chemical analysis. Infrared (IR) spectroscopy has been used to gain insight into cellular composition based on known IR absorption bands, many of which are distinct for various biocomponents: proteins, fats, and sugars, including chitin and glucans (Bakir et al., 2019; Burattini et al., 2008; Cavagna et al., 2010; Šandula et al., 1999). Building on our recent study of *Aspergillus* fungal cell walls (Bakir et al., 2019), we have now used far-field (FF) and near-field nanoscale (nano) FTIR spectroscopy on intact yeast cells to explore differences in the cell wall composition of a wild-type strain and two yeast knock out (YKO) strains: *kre6Δ* and *knr4Δ*. FF-FTIR hyperspectral images were recorded from whole cells in transmission mode and by attenuated total reflection with a microdevice (FF-FTIR + ATR), with an FTIR microscope and a Focal Plane Array (FPA) detector. Although the ATR spectra should contain a relatively greater contribution from the cell wall than transmission spectra, both methods probe whole cells at the μm scale. These FF spectra served as a basis for comparison with nano-FTIR spectra recorded with scattering scanning near-field optical microscopy (s-SNOM), which should access only the cell wall, by probing a voxel on the order of ~25 nm (Bechtel et al., 2014, 2020; Huth et al., 2012; Mastel et al., 2015; Nečas & Klapetek, 2012). Herein, we present the first direct nanoscale spectrochemical analysis of differences in the cell walls of these wild-type and mutant strains.

6.4 Methods

6.4.1 Materials

Wild-type (BY4741), *knr4Δ* and *kre6Δ* strains of *S. cerevisiae* were obtained from the Open Biosystems YKO collection. Yeast extract Peptone Dextrose broth (YPD, Y1375) and bacteriological agar (A5306) were purchased from Sigma-Aldrich Co. Ultra-pure (18 MΩ) water was obtained by filtration (Thermo Scientific™ Barnstead™ Easypure™ II system). Reference standards of isolated components [chitin (C9752), laminarin (L9634), mannan (M7504) and β-1,3-glucan (89862)] were purchased as powders from Sigma-Aldrich Co. Infrared transparent BaF_2 crystal windows (25 mm diameter, 2 mm thick, COE Optics) were used for FFIR transmission spectroscopy. Gold coated silicon wafers (AuSi) were prepared in-house and cut into ~1 cm squares for FF micro-ATR and nano-FTIR of yeast cell walls.

6.4.2 Yeast cell preparation

Yeast cells were cultured for 24 hours at 30 °C on YPD solid medium (50 g/L YPD broth, 20 g/L agar) in Petri dishes. For each strain, a single mature colony was removed from the culture plate, suspended in 1 ml of ultra-pure water, and centrifuged for 5 min at 5300 ×*g*; the supernatant was discarded. This procedure was repeated three times, then cells were resuspended in 1 mL ultra-pure water. A 5 µL aliquot from this suspension was placed onto either an AuSi square or a BaF_2 window, dried in a desiccator at room temperature for 15 to 30 min and stored in a sealed plastic case, in the dark, at room temperature until IR data collection.

6.4.3 FF-FTIR transmission and ATR

Cells on BaF_2 windows were imaged in transmission mode with an Agilent Cary 670 interferometer and 620 IR microscope equipped with a Focal Plane Array (FPA) MCT detector with normal magnification optics (15×, 0.62 NA), yielding a 64×64 array of 4096 spectra with an effective geometric pixel size of 5.5 × 5.5 μm^2. Sample spectra were acquired as 128 coadded scans (6 minutes) using ResolutionsPro™ software (Ver. 5.3.01964, Agilent Technologies Inc., USA). Sample spectra were normalized against a background of 256 scans taken on a clean area of the BaF_2 window.

FF-FTIR + ATR spectra were acquired from yeast cells on AuSi squares with the Agilent slide-on micro-ATR accessory (Ge crystal), as sums of 128 sample scans ratioed against an air background of 512 scans. All spectra were collected at 4 cm^{-1} spectral resolution. The index of refraction of Ge is 4, thus the effective geometric pixel size is 1.4 × 1.4 μm^2 in the ATR-FPA image, with a wavelength-dependent penetration depth of about 1 to 1.5 μm. ATR spectra were corrected for the wavelength dependence of penetration depth into the sample using ResolutionsPro™ software. FF-FTIR + ATR spectra of standard carbohydrates in powder form were collected with a Bruker Alpha-P FTIR spectrometer (diamond crystal) as sums of 128 sample scans ratioed against an air background of 512 scans; the ATR correction was applied automatically in the Bruker OPUS software [ver. 7.2.139.1294].

.

6.4.4 AFM imaging and Near-Field nano-FTIR Spectroscopy

AFM images were recorded with a specially modified AFM (Innova, Bruker) within the Synchrotron Infrared NanoSpectroscopy (SINS) instrument (Bechtel et al., 2014) on beamline 5.4

at the Advanced Light Source (ALS), Lawrence Berkeley National Laboratory, USA. AFM images were collected in tapping mode using a platinum silicide AFM tip (Nanosensors^{TM} PtSi-NCH), for which the cantilever had a nominal resonant frequency of 330 kHz. AFM images were processed with the Gwyddion imaging software (Ver. 2.51, Brno, Czechia) (Nečas & Klapetek, 2012). Isolated single yeast cells were identified by AFM prior to nano-FTIR spectroscopy. Cells with heights <2.5 um were selected for analysis since they were within the AFM z-piezo range.

The SINS system is constructed as an asymmetric Michelson interferometer (Bechtel et al., 2014). Synchrotron IR light is passed through a beam splitter such that half of the light illuminates the AFM tip while the other half is directed to the moving mirror of a modified commercial rapid scan FTIR spectrometer (Nicolet 6700, Thermo-Scientific). The backscattered light from the tip is combined with the reflected light from the reference moving mirror and interferometrically detected with an MCT detector.

A background spectrum was first recorded on a clean portion of the AuSi square. An AFM scan of the target cell was used to locate a suitable region for spectral acquisition. For each background and sample spectrum, 512 scans were co-added with a spectral resolution of 8 cm^{-1}. A rapid AFM scan, typically 2x2 μm^2, with 20 nm step size, was recorded immediately prior to and after each spectral acquisition to ensure that the target cell had not drifted. Typically, 3 or 4 sample spectra were acquired, followed by collection of a new background spectrum to allow for slight variations in beam alignment. The total time to acquire a spectrum was typically about 15 minutes, given 6 minutes per spectrum, the requirement for frequent background spectra and numerous rapid AFM images to counter drift.

For all near-field spectra, the second order scattering amplitude $s_2(\omega)$ and phase $\varphi_2(\omega)$ spectra were obtained by demodulating the interferometric signal at the second harmonic of the tip

tapping frequency with a lock-in amplifier (Huth et al., 2012; Mastel et al., 2015) and then Fourier transforming the resulting signal using a custom Fourier Transform analysis package (Nanospectroscopy Data Analysis, v. 2, Advanced Light Source). Nano-FTIR spectra of yeast were normalized against background spectra acquired at a clear surface on the AuSi square, according to equation 6.1:

$$\text{Nano-FTIR spectrum} = \frac{s_2(yeast,\omega)}{s_2(gold,\omega)}\sin[\varphi_2(yeast,\omega) - \varphi_2(gold,\omega)] \quad 6.1$$

For our data, tapping amplitudes of ~70-90 nm were used, as per the recommended settings for optimal signal (Bechtel et al., 2020). Spectral bands from the known tip contaminant, polydimethylsiloxane (PDMS) (Bechtel et al., 2020), were removed by subtracting a reference PDMS spectrum from any sample spectrum in which it appeared.

6.5 Results

IR spectra from all three methods were used to characterize the cell wall composition and to compare differences among the three *S. cerevisiae* strains (wild-type BY4741, *knr4Δ* and *kre6 Δ*). Each method provided a different perspective: whole cell (FF-FTIR), cell wall plus some cytoplasm (FF-FTIR+ATR), and cell wall alone (nano-FTIR). Initial analyses were based on the presence and relative intensity of standard reference absorption bands for protein (amide I at ~1650 cm^{-1}, mainly carbonyl stretch mode, and amide II at 1545 cm^{-1}, mainly protein C-N stretching + N-H bending) and bands in the predominantly carbohydrate region (900–1200 cm^{-1}) (Bakir et al., 2019; Hromádková et al., 2003; Mehranian et al., 2017; Šandula et al., 1999; Zechner-Krpan et al., 2010).

6.5.1 FF-FTIR transmission spectroscopy of yeast cells

For each strain, several FPA hyperspectral images were collected from freshly harvested cells mounted on BaF_2 windows (**Figure 6.1**). Typical bright-field images (**Figure 6.1**, left column) showed numerous dense yeast cell clusters, in which the cells appeared dark against the transparent salt window. False colour FPA images were generated in ResolutionsPro™ by integrating the area of the amide I band (**Figure 6.1**, middle column) showed that IR absorption by protein corresponded to the cell locations, as expected. The wavelength-dependent spatial resolution at 1650 cm^{-1} is ~6μm; therefore, individual cells could not be resolved. Since cells had a rounded shape with dimensions on the order of the IR wavelengths, some spectra exhibited significant Mie and Resonant Mie scattering (RMieS) artifacts, including rolling baselines and dispersion-like characteristics in strong bands (Bassan et al., 2010; Mie, 1908; Mohlenhoff et al., 2005). Average spectra were created from the 20 best spectra from each image, selected for the best signal-to-noise ratio (SNR), baseline flatness and absence of scattering artifacts (Figure 6.1, right column). All spectra contained traces of water vapour that were removed by subtracting a spectrum from within the same FPA image where cells were absent (see Supplemental Figure 6.1)**.** In the average spectra of all 3 strains, the bands for the amide I and II modes were much stronger than those in the predominantly carbohydrate region (900–1200 cm^{-1}). Despite some observable differences among the strains, bands from the cell body, such as C=O from lipid membranes at 1740 cm^{-1} were strongly evident. It was concluded that the FF-FTIR transmission spectra of cells on salt windows represented the content of the whole cell body, as had been anticipated. As such, the FF-FTIR transmission spectra provided a useful whole cell standard for comparison with ATR and nano-FTIR data. Spectral and structural differences were explored further with IR methods that probe smaller voxels, to approach spectra that reflect primarily the cell wall composition.

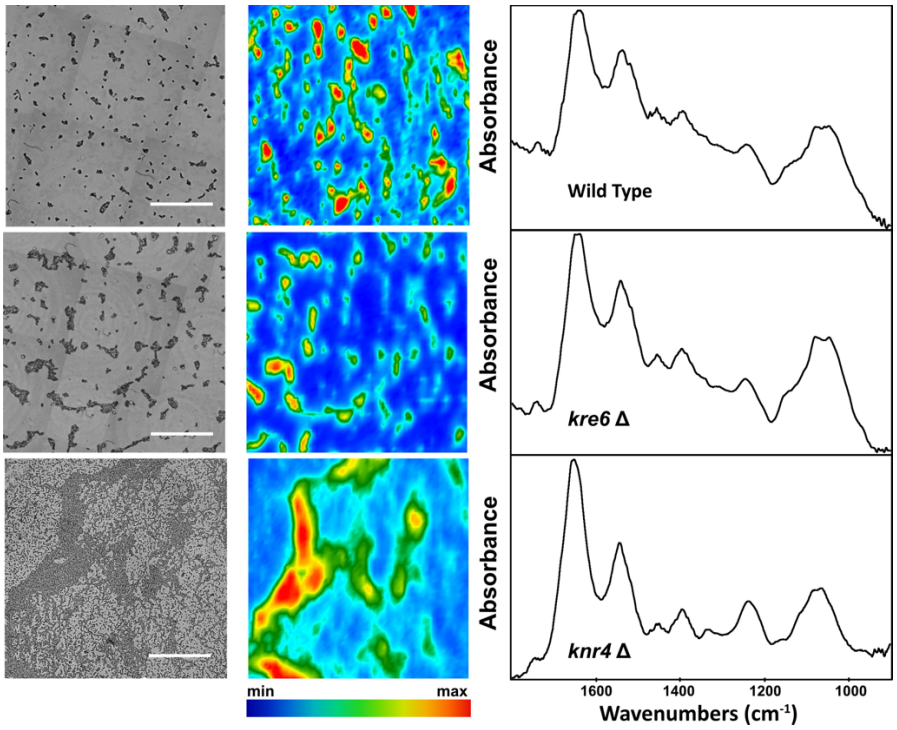

Figure 6.1 Images of wild-type BY4741, *kre6Δ* and *knr4Δ* whole cells recorded in bright field and transmission FF-FTIR with FPA. Left: Bright field images of cells mounted on BaF_2 windows. Scale bar = 100 μm. Centre: Corresponding false-colour 64×64 FPA images, processed on the integrated area of the amide I band at 1650 cm^{-1}. Maximum signal (red) corresponds to location of cells and cell clusters. Right: Average of 20 best quality spectra extracted from each image.

6.5.2 *FF-FTIR + ATR spectroscopy of wild-type and mutants*

FF-FTIR + ATR spectra of the three yeast strains were collected by direct crystal contact to cells mounted on AuSi squares, at several locations for each strain (Figure 6.2). The micro-ATR field of view was focused onto the FPA, again yielding an array of 64×64 spectra at each contact site. Bright field microscopy images (Figure 6.2, insert) show the cells before and after the ATR crystal touch down. In each case, a cluster of cells had been disturbed, evidence that they had been

contacted directly. Yeast cells are sharply rounded and hard, resulting in poor contact with the ATR crystal (**Supplemental Figure 6.2**). The spectra in Figure 6.2 were created by averaging the 20 best spectra from FPA images for each strain, with selection based on the same criteria adopted for the transmission FF-FTIR. The original ATR spectra (**Supplemental Figure 6.3**) contained water vapour bands and required the standard ATR correction for wavelength dependent depth penetration. After the removal of water, the standard ATR correction was applied in the ResolutionsPro™ software using the refractive index of 4.003 for Ge, and 1.5 for the yeast cells. The relative intensity of the carbohydrate bands had increased noticeably relative to that of amide bands, as seen in the whole cell spectra acquired in transmission mode, but the lipid C=O band was still evident.

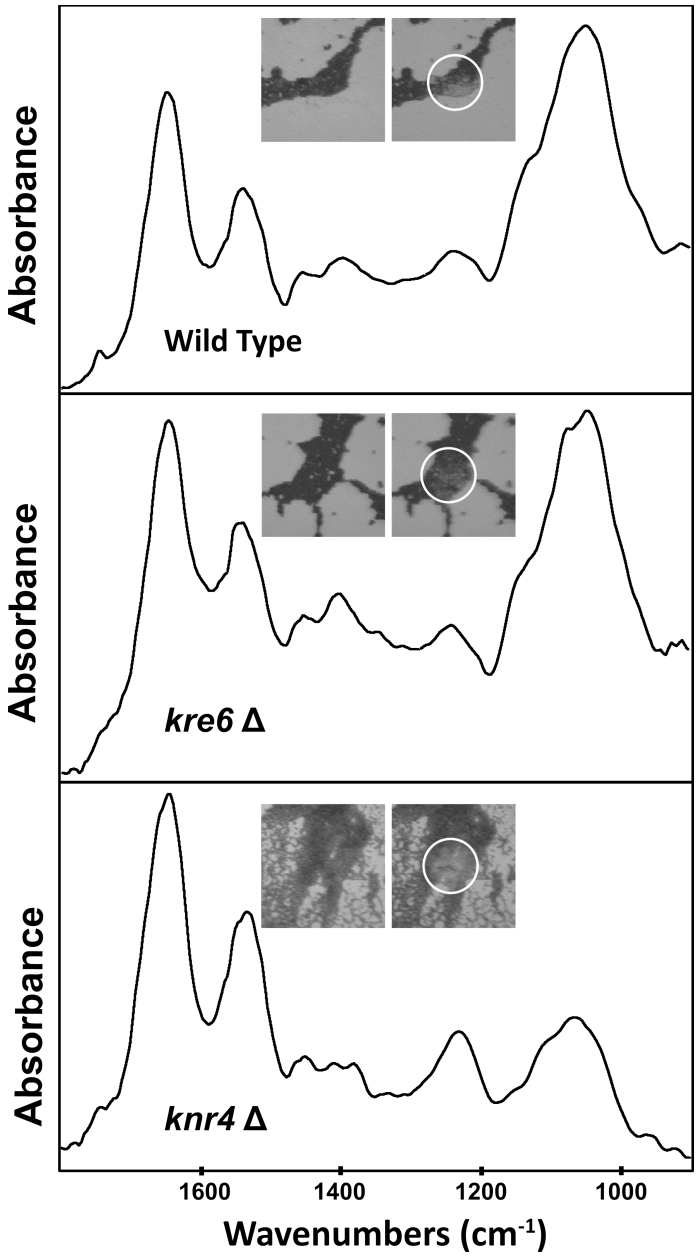

Figure 6.2 Bright field images (insets) and FF-FTIR-ATR spectra of wild-type, *kre6Δ* and *knr4*Δ whole cells mounted on AuSi squares. Spectra are an average of the best 20 spectra from the FPA image. Bright field 15x images, before (left) and after (right) ATR crystal touch down, show the contact region for each.

6.5.3 Nano-FTIR spectroscopy of yeast strains

For the nano-FTIR, replicate spectra were recorded from 3 wild-type cells, 9 *kre6* mutant cells, and 10 *knr4* mutant cells. Representative topographic AFM images of three individual yeast cells, one from each strain, are shown in the left column of Figure 6.3; circles indicate where spectra were taken (15 spectra each for wild-type and *knr4Δ*, 22 spectra for *kre6Δ*). The total broadband scatter images (Figure 6.3, middle column) showed lower IR scatter across each cell; hence, they appear to be very dark. Scattering was high in the bright non-absorbing surrounding regions. We noted interesting patterns in the IR scattering images, particularly the bright spots around the cell locations. These are artifacts due to the illumination geometry and the curvature and dimension of the cells, which caused the cells to act as nano lenses for the incident IR light.

Nano-FTIR spectra (Figure 6.3, right column) were created by averaging single point spectra for each cell to improve the SNR. Band intensities in the carbohydrate region were much more prominent in wild-type and *kre6Δ* compared to the amide bands, evidence that only the carbohydrate-rich cell wall was probed by nano-FTIR (Nguyen et al., 1998).

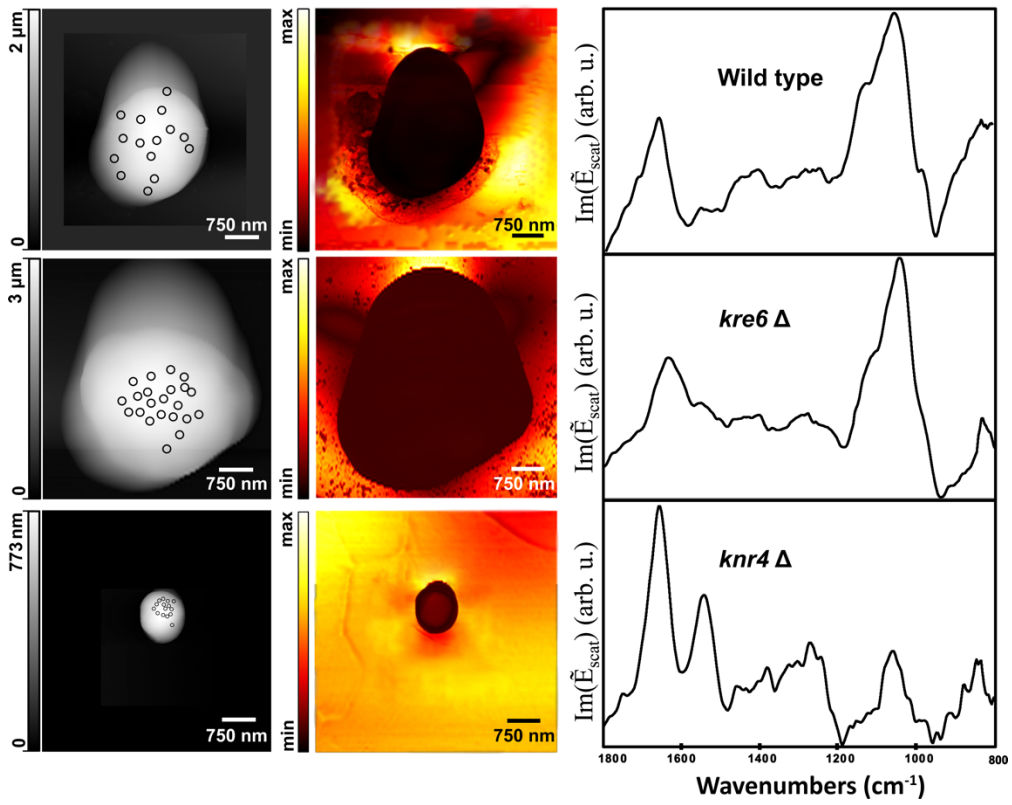

Figure 6.3 AFM and nano-FTIR images and spectra of cells mounted on AuSi squares, recorded in tapping mode. Left: AFM topography images of individual cells; circles show where spectra were collected. Centre: nano-FTIR heat map image, showing total broadband IR scattering. Right: Nano-FTIR spectra for each cell averaged from 15 spectra each for wild-type and *knr4Δ* and 22 spectra for *kre6Δ*.

Band assignments for the target compounds are summarized in Table 1, based on data recorded here and in other yeast cell studies. Two references noted traces of protein, 2-6%, in the isolated carbohydrate samples (Hromádková et al., 2003; Zechner-Krpan et al., 2010); another used whole cell ATR which necessarily probed cell interior (Galichet et al., 2001); while others were recorded in media (Burattini et al., 2008; Cavagna et al., 2010). Despite the useful information provided, the presence of other materials impeded clear assignments. Therefore, ATR spectra of isolated wall components were acquired as reference standards (Figure 6.4) to

corroborate band positions reported in the literature and to enable direct comparison with our nano-FTIR spectra. A weak band at 1645 cm^{-1} in the spectra of mannan and the glucans was evident in literature spectra (Zechner-Krpan et al., 2010); those samples were reported as having water content of up to 10.8 % by mass. The same band was observed here (Figure 6.4) and was assigned as the bending mode of residual water. Given the preponderance of OH bonds in carbohydrates, it was not possible to assess water from the OH stretch region of the reference spectra, nor was it useful as the near-field IR spectra did not extend to this region.

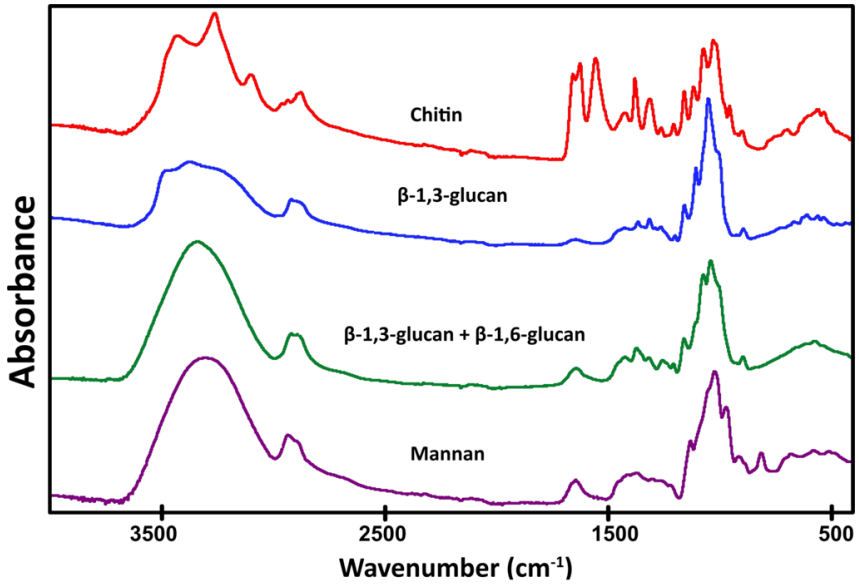

Figure 6.4 ATR spectra of isolated cell wall carbohydrate standards.

Table 6.1 Nano-FTIR band positions (cm^{-1}) and assignments for *S. cerevisiae* strains.

Wild-type	*kre6Δ*	*knr4Δ*	Assignment	References*
803, 829, 859, 880, 900	811, 830, 882, 916, 976	815, 834, 844, 879, 911, 975	Mannan	(Burattini et al., 2008; Cavagna et al., 2010)
988		992	β-1,6-glucans	(Burattini et al., 2008; Cavagna et al., 2010; Galichet et al., 2001)
1031	1042	1039	β -glucan	(Galichet et al., 2001)
1119-1135	1112-1136	1111	ν (CC), C-O-C chitin, β-glucan	(Mehranian et al., 2017; Šandula et al., 1999)
1150	1156	1151	C–O, C–OH, chitin, β-glucan	(Galichet et al., 2001)
		1375, 1309	chitin	This work (Figure 6.4)
1500-1190	1500-1190	1500-1190	carbohydrates	This work (Figure 6.4)
1548	1547	1542	Amide II	This work
1633	1634, 1612	1631	ν (C=O), chitin (acetamide)	(Mehranian et al., 2017; Šandula et al., 1999)
1663	1634 (broad)	1656	amide I (C=O), chitin (acetamide)	(Hromádková et al., 2003; Šandula et al., 1999; Zechner-Krpan et al., 2010)
		1748	Lipid carbonyl	This work

*All literature assignments were reconfirmed with our reference spectra (Figure 6.4).

6.6 Discussion

Wild-type and mutant *S. cerevisiae* have often been used as important models for understanding cell surface biology of yeasts. Towards this end, structure and composition have been studied with a wide variety of methods, many of which require chemical, mechanical or enzymatic extraction and isolation of cell wall components for subsequent chemical analyses, electrophoresis, chromatography, fluorescence, NMR, etc (Kapteyn et al., 1999; Klis et al., 2002; Michell & Scurfield, 1970; Roemer et al., 1993; Roemer & Bussey, 1991). The goal of the present study was to image wild-type and cell wall biogenesis mutants by IR spectroscopic methods from

the μm to nm scale, in order to interpret cell wall spectral signatures, detected *in situ*, in the context of changes in macromolecular composition.

Kre6 and Knr4 are proteins responsible for the biosynthesis of cell wall components, particularly for β-1,6-glucan and β-1,3-glucan, respectively. Their absence enforces reliance on different pathways or linkages to build and maintain the cell wall (Martin et al., 1999; Roemer & Bussey, 1991). The *S. cerevisiae* wild-type and *knr4Δ* strains have been studied by AFM and force spectroscopy to assess cell wall elasticity and its relationship to cell wall chemical composition as determined by standard isolation and chromatography (Dague et al., 2010). The authors found that cell wall elasticity was reduced by 50% in the *knr4Δ* strain in the stationary phase, along with increased surface roughness in the cell surface topology. Isolation of cell wall components showed that the relative amounts of β-glucan, mannan and chitin changed from 50%, 49% and 1% to ~30%, 67% and 3%, respectively. However, they could not correlate roughness or elasticity with cell wall composition for several different but similar mutants.

Romer & Bussey (1991) found reduced levels of both β-1,3- and β-1,6-glucan in isolates from the cell walls of *kre6Δ* strains (Roemer & Bussey, 1991). More recently, cell lysates from *kre6Δ* strains were investigated via Western blotting with enhanced chemiluminescence detection, and whole cells (fixed and stained) were imaged with immunofluorescence microscopy and immunoelectron microscopy (Kurita et al., 2011). A significant portion of Kre6 was found in the polarized plasma membrane buds required for β-1,6-glucan synthesis, though there was no direct chemical analysis of the cell wall composition. Han et al. (2019) observed C. *albicans kre6Δ/Δ* cells grown in media, by bright-field and TEM, showing that the kre6 gene was not essential for the viability, but its double mutation resulted in cell separation defects when *SKN1* was supressed (Han et al., 2019a). None of the techniques noted above allow direct, non-disruptive chemical

analysis of the cell wall. However, with label-free IR spectroscopic imaging of whole cells and cell wall components, direct chemical identification of cell wall composition can be achieved at the nanoscale level, without staining or cell wall isolation (Bakir et al., 2019).

FF-FTIR transmission mode imaging with normal magnification optics measures the chemical composition at voxel dimensions that are nominally 5×5×5 μm^3. These voxels are subject to the Rayleigh diffraction limit, where the IR wavelengths range from 2.5 to 12 μm in our spectra (Findlay et al., 2015). Mie scattering artifacts in FF-FTIR can further compromise spectral analysis of single cells, whether in transmission or transflection (Kaminskyj et al., 2008; Saulou et al., 2010; Szeghalmi et al., 2007). Here, spectra were collected from small clusters of cells to minimize such artifacts. The FF-FTIR spectra in **Figure 6.1**, selected to be artifact-free, contain information from the cell wall, membranes, cytoplasm, and internal organelles. Numerous vibrational bands characteristic of cell content were observed, including those from fatty acid esters (C=O stretch, ~1740 cm^{-1}), proteins (amide I or C=O, ~1650 and amide II or N-H bend with C-N stretch, ~1545 cm^{-1}), phosphate groups in nucleic acids and phospholipids (1300-1000 cm^{-1}), and carbohydrates (900-1200 cm^{-1}). In yeasts, amide I and II bands can also arise from the *N*-acetyl functional groups of chitin within the cell wall.

In the FF-FTIR transmission spectra of all strains, the amide peak intensities were much higher relative to the bands in the carbohydrate region (Figure 6.1, right column). The 1740 cm^{-1} band assigned to lipid membrane bilayers was also clearly evident. Given that membranes and the majority of proteins are located in the cell interior, we conclude that the spectra are, not surprisingly, dominated by total cell content at this voxel dimension. The FF-FTIR spectra provided a useful reference for whole cells, and a reliable contrast for spectra acquired with methods that would provide better spatial resolution (Szeghalmi et al., 2007).

Significant differences could be noted between transmission and ATR FF-FTIR spectra for the wild-type and *kre6Δ* spectra, the most obvious being an increase in the relative intensity of carbohydrate to amide bands in the ATR spectra (Figure 6.2). This result is consistent with the cell dimensions (1-5 μm diameter) (Dagkessamanskaia et al., 2010). With a probe depth of ~1.4 μm, the ATR spectra sample less of the cell interior and would therefore contain proportionally more information on the carbohydrate-rich cell walls. Spectral differences within the carbohydrate regions of wild-type and *kre6Δ* included a shoulder emerging at ~990 cm^{-1}, assigned to β-1,6-glucan, and weak bands below 950 cm^{-1} that could be associated with the presence of mannans. The *knr4Δ* ATR spectra were very similar to those from whole cell transmission; this was ascribed to their smaller size, <2 μm, close to that of the ATR probe depth. For all strains, the carbonyl stretching mode from fatty acid esters (~1740 cm^{-1}) remained apparent. Despite the increased cell wall carbohydrate contribution to the wild-type and *kre6Δ* spectra, we concluded that the yeast cell interior was still evident, underscoring that neither the FF-FTIR transmission nor ATR methods were sufficient to analyze changes in cell wall composition.

Given the nano FTIR probe depth of ~20-25 nm, SINS was anticipated to be ideal for directly probing the cell wall composition at the desired spatial resolution (Dupres et al., 2010; Lesage & Bussey, 2006; Stratford, 1994). The s-SNOM technique yields wavelength-independent spectra and images without MieS or RMieS artifacts; however, selection of data collection sites was still dependent on tip-sample interactions. The AFM images of wt and *kre6Δ* showed a strong edge effect (Dague et al., 2010), attributed to their height and steeply curving sides. The *knr4Δ* cells were much smaller, with dimensions on the order of 750 nm to 1 μm, but still showed some edge effects. For all cells, good tip contact was maintained across the central upper surface as evidenced by the clear bright centers (**Figure 6.3**, AFM, left column) and dark scattering (**Figure**

6.3, total IR broadband scatter, middle column). Therefore, spectra were acquired only in this region of each cell. Spectral features were assigned and interpreted according to reference standards (**Figure 6.4** and **Table 6.1**).

Wild-type: The carbonyl stretching mode from fatty acid esters (1740 cm^{-1}) was not apparent in the wild-type nano-FTIR spectrum (**Figure 6.3**, top right), evidence that signal arose only from cell wall components exterior to the cell's plasma membrane. Though a strong band with a maximum ~1663 cm^{-1} was observed where the amide I is expected, the amide II band was much weaker. Therefore, bands in the 1500-1700 region were assigned as a combination of a small amount of protein (1656 and 1554 cm^{-1}) and water associated with the cell wall carbohydrates. Bands between 1500-1190 cm^{-1} were assigned to glucans and mannans. The shoulder at 988 cm^{-1}, assigned to β-1,6-glucan, was more obvious in the wild-type nano-FTIR spectrum than the FF ATR spectrum (**Figure 6.2**). The intensity of the carbohydrate region (glucans 1100-900 cm^{-1} and mannan peaks below 900 cm^{-1}) was increased relative to the amide+water bands compared to all FF spectra. Notably, the many prominent chitin peaks (1654, 1622, 1375, 1309 cm^{-1}, **Figure 6.4**, top) were not apparent in wild-type nano-FTIR spectra, confirming that the volume probed did not extend to this innermost layer of the cell wall.

kre6Δ: The Kre6 protein localizes to the endoplasmic reticulum, plasma membrane, sites of polarized growth and secretory vesicles (Kurita et al., 2011; Roemer et al., 1993; Roemer & Bussey, 1991). Deletion of *KRE6* was reported to reduce the amount of β-1,6-glucan in the cell wall, as the gene product is directly responsible for the biosynthesis of β-1,6-glucan (Han et al., 2019a; Uchiyama et al., 2018). We have confirmed the effect of this mutation with the analysis of the *kre6Δ* nano-FTIR spectra (**Figure 6.3**, middle, right). The band at 1740 cm^{-1} is not apparent and chitin bands are absent, again showing that only the outer cell wall had been probed. The ratio

of band intensities for (amide+ water) and carbohydrate bands was similar to that of wild-type spectra. The amide II band was still discernible despite the presumed presence of water, leading to a poorly resolved pair of band maxima at 1634 and 1552 cm^{-1}. Numerous overlapping bands in the 1500-1190 cm^{-1} region could be assigned as mixed carbohydrates (Table 1). The lower energy shoulder (~990 cm^{-1}) in the carbohydrate region assigned to β-1,6-glucan was not evident in the *kre6Δ* spectra. The intensity of mannan bands (at 975-800 cm^{-1}) in *kre6Δ* spectra were slightly reduced relative to those in the same region in the wild-type. Thus, absence of specific bands and differences in the relative intensities are direct evidence that the β-1,6-glucan content is reduced in the *kre6Δ* wall.

knr4Δ: Knr4 is a cell-signaling protein involved in the control of cell wall biosynthesis (Hong et al., 1994). It is important for chitin deposition at bud sites and for cell wall assembly, and has been identified as a hub protein that interconnects numerous cell processes related to cell wall synthesis, cell cycle progression and morphogenesis (Martin-Yken et al., 2016). Kurita et al. analyzed cell wall carbohydrate composition by acid hydrolysis of cells followed by anionic exchange chromatography to quantify the glucose, mannose and chitin that were released (Dague et al., 2010). They reported that the glucan/mannan ratio changes from 50:50 to about 30:65 in the *knr4Δ* mutant whether in stationary or exponential growth phase. Though still small, they found that the chitin content increases from at ~0.6 to 1.2% in wild type to 3.3 and 2.9% in the *knr4Δ* mutant, in exponential and stationary growth phases, respectively.

The nano-FTIR spectrum of *knr4Δ* was significantly different from those of both wild-type and *kre6Δ.* The lipid band at 1740 cm^{-1} was visible, suggesting that the plasma membrane was within the voxel. If so, then the cell wall was on the order of 30 nm thick, which could be consistent with the small cell size and the malformed cell state. The strong amide I band at ~1654 and weaker

amide II at ~1550 cm^{-1} are more typical of protein than chitin, though the latter could easily be present in low amounts. Other chitin bands at 1375, 1309 cm^{-1} were observed in the *knr4Δ* spectra, and with greater intensity than in the wild-type strain. The amide band intensities were much greater than the carbohydrate bands in *knr4Δ*, further evidence of contributions from the interior, although amide bands could also arise from mannoproteins located in the outermost layer of the cell wall (Klis et al., 2002). The relatively weak intensity in the 1200-900 cm^{-1} region shows there is a significant reduction in β-1,3-glucan and β-1,6-glucan content. Unlike the wild-type and *kre6Δ* the intensities of mannan bands in *knr4Δ* spectra are almost equal to the entire carbohydrate region (1200-900 cm^{-1}). Taken together, the nano-FTIR spectra show that there is a significant reduction in glucans and a relatively greater amount of chitin and mannan in the *knr4Δ* wall than in either wild-type or *kre6Δ* (Dague et al., 2010; Hong et al., 1994; Martin et al., 1999; Martin-Yken et al., 2016).

6.7 Conclusions

Mutations affecting the CWI pathway of *S. cerevisiae* result in altered cell wall structure and composition, but these changes are challenging to detect directly as the multi-component cell wall is only ~100 nm thick. By probing to ~1 μm depth, FF-FTIR+ATR spectrochemical imaging provided a better window into the cell wall composition compared to that of FF-FTIR in transmission mode. Despite the high quality of the spectral signal to noise, the wavelength-dependent spatial resolution limited further analysis in both FF methods. Through comparison of nano-FTIR spectra from mutants and wild-type cells, we found that the β-1,6-glucan content is reduced in the cell wall of the *kre6Δ* mutant. Similar comparisons showed that the *knr4Δ* mutant had relatively less glucan overall, consistent with indirect evidence from previous studies.

Depletion of glucans may have resulted in a much thinner cell wall in the *knr4Δ* mutant than in wt or *kre6Δ*, given our observation of chitin and mannan bands, as well as stronger lipid membrane and protein signals in the nano-FTIR spectra of this mutant. Our results show, for the first time, that nano-FTIR spectroscopy is an excellent means to directly probe cell wall biochemical composition in intact, single yeast cells.

6.8 Supplemental information

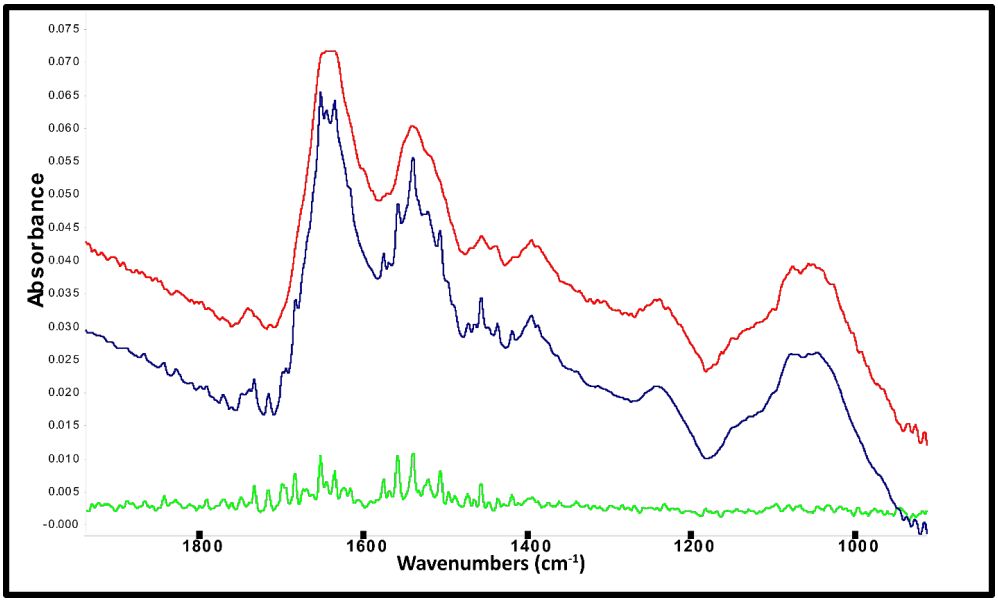

Supplemental Figure 6.1 Water vapour and Mie scatter in FF-FTIR transmission spectra. The spectra above illustrate the problems encountered with FF-FTIR transmission spectroscopy of yeast cells. The Red spectrum (Top) shows the average of 20 spectra selected from the original FF-FTIR transmission FPA image for wild-type yeast after water vapour correction. There is an obvious baseline slope from high to low energy that is attributed to Mie scatter from the small round cells. The scatter is not severe enough to be resonant (RMieS) in which the dispersion

spectrum (first derivative band shape) would be convoluted with the absorbance spectrum. RMieS artifacts were found in some spectra from the FPA hyperspectral image but those spectra were not used. Corrections for Mie scatter are difficult and not reliable. We did not attempt to correct for this, especially as the spectra were of the entire cell, not just the thin cell wall. The Blue spectrum shows original data from FF-FTIR transmission FPA image before removal of the water vapor bands. The Green spectrum is from a pixel with only a water vapour spectrum, selected from a cell-free part of the same FPA image. This sort of spectrum was used to subtract the water vapour, using the standard simple subtraction option in Agilent ResolutionsPro™ software (Ver. 5.3.01964, Agilent Technologies Inc., USA), where a scale factor is adjusted by the operator to remove the water vapour signature.

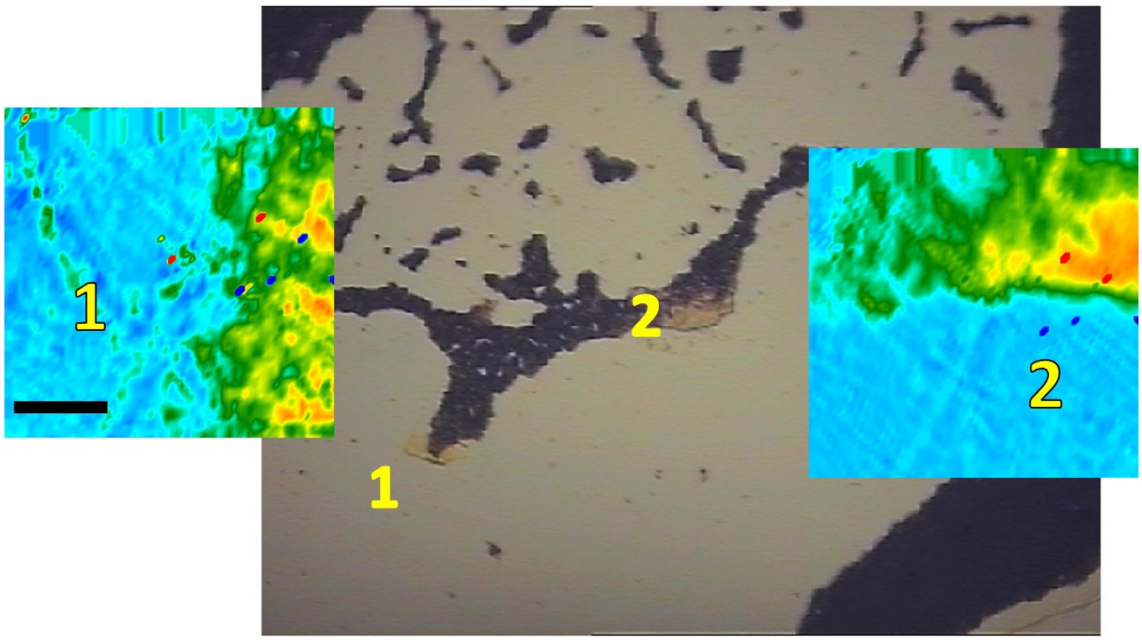

Supplemental Figure 6.2 ATR-FF-FTIR of wild-type BY4741, whole cells recorded with FPA. *Center*: Two touchdown points, labelled 1 and 1, can be seen in the brightfield FTIR microscope

photo, recorded at 10x. An expanded view of the second touch down region, before and after touchdown, appears in Figure 2 of the manuscript. *Left and right*: The corresponding false-colour 64×64 FPA images shown on the left and right of the photo have been processed on the integrated area of the amide I band at 1650 cm^{-1}. The maximum signal (red) corresponds to location of cell clusters. Spectra for the average, also shown in Figure 2 of the manuscript, were taken from points with the best contact between ATR accessory and the sample. The spectra used to create the averages are shown in Supplemental Figure Supplemental Figure 6.3. Scale bar = 100 μm.

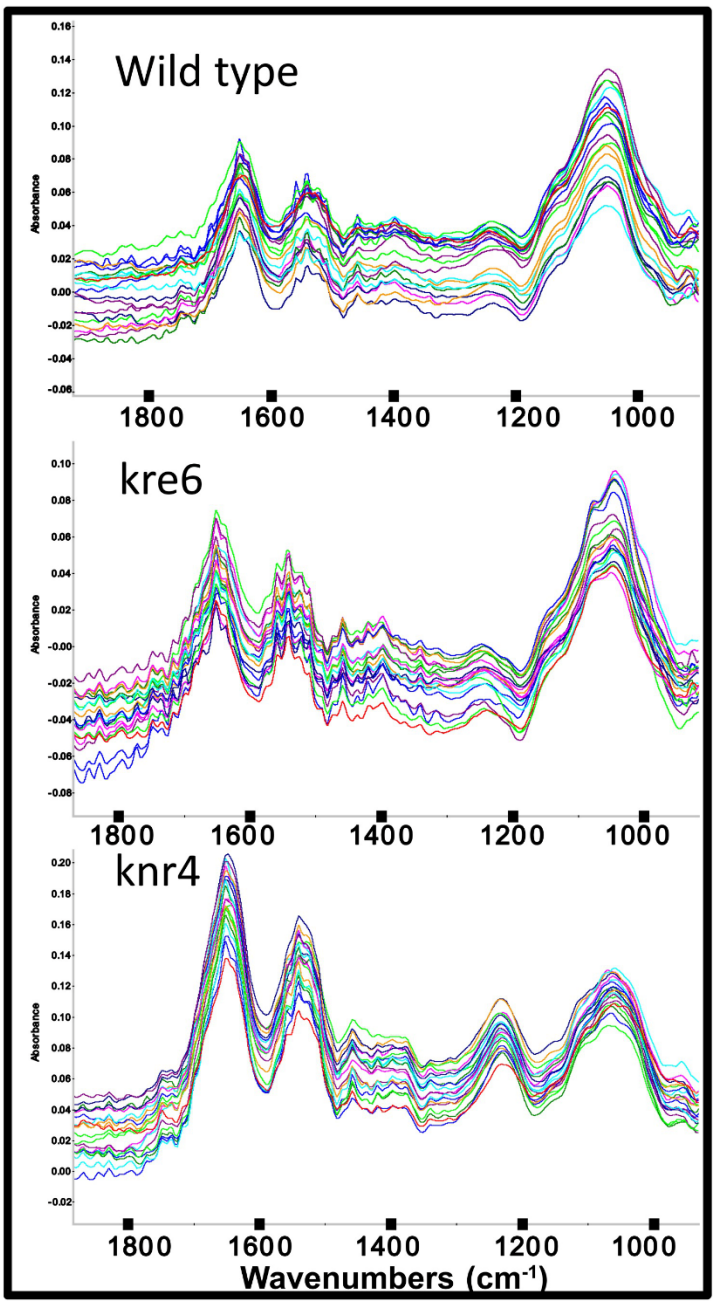

Supplemental Figure 6.3 Individual ATR-FF-FTIR spectra. These spectra were selected for averaging in Figure 2 of the manuscript, from wild-type BY4741, *kre6Δ* and *knr4Δ* yeast strains. These are the original spectra, prior to subtraction of water vapour and correction for wavelength dependent ATR depth penetration. The spectral profiles from any one ATR image were very similar. There are some differences between the strains, as noted in the manuscript. The differences

between these spectra and those from the other two techniques (FF-FTIR transmission, nano-FTIR) showed us that while the ATR spectra contained a greater contribution from the cell wall, there were still contributions from within the cell, as see from the lipid C=O band, noted in Figure 2 of the manuscript.

6.9 References

Bakir, G., Girouard, B. E., Johns, R. W., Findlay, C. R. J., Bechtel, H. A., Eisele, M., Kaminskyj, S. G. W., Dahms, T. E. S., & Gough, K. M. (2019). Ultrastructural and SINS analysis of the cell wall integrity response of: Aspergillus nidulans to the absence of galactofuranose. *Analyst*, *144*(3), 928–934. https://doi.org/10.1039/c8an01591k

Bassan, P., Kohler, A., Martens, H., Lee, J., Byrne, H. J., Dumas, P., Gazi, E., Brown, M., Clarke, N., & Gardner, P. (2010). Resonant Mie Scattering (RMieS) correction of infrared spectra from highly scattering biological samples. *Analyst*, *135*(2), 268–277. https://doi.org/10.1039/b921056c

Bechtel, H. A., Johnson, S. C., Khatib, O., Muller, E. A., & Raschke, M. B. (2020). Synchrotron infrared nano-spectroscopy and -imaging. *Surface Science Reports*, *75*(3), 100493. https://doi.org/10.1016/j.surfrep.2020.100493

Bechtel, H. A., Muller, E. A., Olmon, R. L., Martin, M. C., & Raschke, M. B. (2014). Ultrabroadband infrared nanospectroscopic imaging. *Proceedings of the National Academy of Sciences of the United States of America*, *111*(20), 7191–7196. https://doi.org/10.1073/pnas.1400502111

Burattini, E., Cavagna, M., Dell'Anna, R., Malvezzi Campeggi, F., Monti, F., Rossi, F., & Torriani, S. (2008). A FTIR microspectroscopy study of autolysis in cells of the wine yeast Saccharomyces cerevisiae. *Vibrational Spectroscopy*, *47*(2), 139–147. https://doi.org/10.1016/j.vibspec.2008.04.007

Cavagna, M., Dell'Anna, R., Monti, F., Rossi, F., & Torriani, S. (2010). Use of ATR-FTIR microspectroscopy to monitor autolysis of Saccharomyces cerevisiae cells in a base wine. *Journal of Agricultural and Food Chemistry*, *58*(1), 39–45. https://doi.org/10.1021/jf902369s

Dagkessamanskaia, A., Azzouzi, K. el, Kikuchi, Y., Timmers, T., Ohya, Y., François, J.-M., & Martin-Yken, H. (2010). Knr4 N-terminal domain controls its localization and function during sexual differentiation and vegetative growth. *Yeast*, *27*(8), 563–574. https://doi.org/10.1002/yea.1804

Dagkessamanskaia, A., Martin-Yken, H., Basmaji, F., Briza, P., & Francois, J. (2001). Interaction of Knr4 protein, a protein involved in cell wall synthesis, with tyrosine tRNA synthetase encoded by TYS1 in Saccharomyces cerevisiae. *FEMS Microbiology Letters*, *200*(1), 53–58. https://doi.org/10.1016/S0378-1097(01)00203-8

Dagley, M. J., Gentle, I. E., Beilharz, T. H., Pettolino, F. A., Djordjevic, J. T., Lo, T. L., Uwamahoro, N., Rupasinghe, T., Tull, D. L., McConville, M., Beaurepaire, C., Nantel, A., Lithgow, T., Mitchell, A. P., & Traven, A. (2011). Cell wall integrity is linked to mitochondria and phospholipid homeostasis in Candida albicans through the activity of the post-transcriptional regulator Ccr4-Pop2. *Molecular Microbiology*, *79*(4), 968–989. https://doi.org/10.1111/j.1365-2958.2010.07503.x

Dague, E., Bitar, R., Ranchon, H., Durand, F., Yken, H. M., & François, J. M. (2010). An atomic force microscopy analysis of yeast mutants defective in cell wall architecture. *Yeast*, *27*(8), 673–684. https://doi.org/10.1002/yea.1801

Dupres, V., Dufrêne, Y. F., & Heinisch, J. J. (2010). Measuring Cell Wall Thickness in Living Yeast Cells Using Single Molecular Rulers. *ACS Nano*, *4*(9), 5498–5504. https://doi.org/10.1021/nn101598v

Findlay, C. R., Wiens, R., Rak, M., Sedlmair, J., Hirschmugl, C. J., Morrison, J., Mundy, C. J., Kansiz, M., & Gough, K. M. (2015). Rapid biodiagnostic ex vivo imaging at 1 μm pixel resolution with thermal source FTIR FPA. *Analyst*, *140*(7), 2493–2503. https://doi.org/10.1039/c4an01982b

Galichet, A., Sockalingum, G. D., Belarbi, A., & Manfait, M. (2001). FTIR spectroscopic analysis of Saccharomyces cerevisiae cell walls: Study of an anomalous strain exhibiting a pink-colored cell phenotype. *FEMS Microbiology Letters*, *197*(2), 179–186. https://doi.org/10.1016/S0378-1097(01)00101-X

Han, Q., Wang, N., Yao, G., Mu, C., Wang, Y., & Sang, J. (2019). Blocking β-1,6-glucan synthesis by deleting KRE6 and SKN1 attenuates the virulence of Candida albicans. *Molecular Microbiology*, *111*(3), 604–620. https://doi.org/10.1111/mmi.14176

Hong, Z., Mann, P., Brown, N. H., Tran, L. E., Shaw, K. J., Hare, R. S., & DiDomenico, B. (1994). Cloning and characterization of KNR4, a yeast gene involved in (1,3)-beta-glucan synthesis. *Molecular and Cellular Biology*, *14*(2), 1017–1025. https://doi.org/10.1128/mcb.14.2.1017-1025.1994

Hromádková, Z., Ebringerová, A., Sasinková, V., Šandula, J., Hříbalová, V., & Omelková, J. (2003). Influence of the drying method on the physical properties and immunomodulatory

activity of the particulate (1 → 3)-β-D-glucan from Saccharomyces cerevisiae. *Carbohydrate Polymers*, *51*(1), 9–15. https://doi.org/10.1016/S0144-8617(02)00110-8

Huth, F., Govyadinov, A., Amarie, S., Nuansing, W., Keilmann, F., & Hillenbrand, R. (2012). Nano-FTIR absorption spectroscopy of molecular fingerprints at 20 nm spatial resolution. *Nano Letters*, *12*(8), 3973–3978. https://doi.org/10.1021/nl301159v

Kaminskyj, S., Jilkine, K., Szeghalmi, A., & Gough, K. (2008). High spatial resolution analysis of fungal cell biochemistry - Bridging the analytical gap using synchrotron FTIR spectromicroscopy. *FEMS Microbiology Letters*, *284*(1), 1–8. https://doi.org/10.1111/j.1574-6968.2008.01162.x

Kapteyn, J. C., van Egmond, P., Sievi, E., van den Ende, H., Makarow, M., & Klis, F. M. (1999). The contribution of the O-glycosylated protein Pir2p/Hsp150 to the construction of the yeast cell wall in wild-type cells and beta1,6-glucan-deficient mutants. *Molecular Microbiology*, *31*(6), 1835–1844. https://doi.org/10.1046/j.1365-2958.1999.01320.x

Klis, F. M., Boorsma, A., & de Groot, P. W. J. (2006). Cell wall construction in Saccharomyces cerevisiae. *Yeast*, *23*(3), 185–202. https://doi.org/10.1002/yea.1349

Klis, F. M., Mol, P., Hellingwerf, K., & Brul, S. (2002). Dynamics of cell wall structure in Saccharomyces cerevisiae. *FEMS Microbiology Reviews*, *26*(3), 239–256. https://doi.org/10.1016/S0168-6445(02)00087-6

Kurita, T., Noda, Y., Takagi, T., Osumi, M., & Yoda, K. (2011). Kre6 Protein Essential for Yeast Cell Wall β-1,6-Glucan Synthesis Accumulates at Sites of Polarized Growth. *Journal of Biological Chemistry*, *286*(9), 7429–7438. https://doi.org/10.1074/jbc.M110.174060

Latgé, J. P. (2007). The cell wall: A carbohydrate armour for the fungal cell. *Molecular Microbiology*, *66*(2), 279–290. https://doi.org/10.1111/j.1365-2958.2007.05872.x

Lesage, G., & Bussey, H. (2006). Cell Wall Assembly in Saccharomyces cerevisiae. *Microbiology and Molecular Biology Reviews*, *70*(2), 317–343. https://doi.org/10.1128/mmbr.00038-05

Levin, D. E. (2011). Regulation of Cell Wall Biogenesis in Saccharomyces cerevisiae : The Cell Wall Integrity Signaling Pathway. *Genetics*, *189*(4), 1145–1175. https://doi.org/10.1534/genetics.111.128264

Martin, H., Dagkessamanskaia, A., Satchanska, G., Dallies, N., & François, J. (1999). KNR4, a suppressor of Saccharomyces cerevisiae cwh mutants, is involved in the transcriptional control of chitin synthase genes. *Microbiology*, *145*(1), 249–258. https://doi.org/10.1099/13500872-145-1-249

Martin-Yken, H., Bedekovic, T., Brand, A. C., Richard, M. L., Znaidi, S., D'Enfert, C., & Dague, E. (2018). A conserved fungal hub protein involved in adhesion and drug resistance in the human pathogen Candida albicans. *The Cell Surface*, *4*(October), 10–19. https://doi.org/10.1016/j.tcsw.2018.10.002

Martin-Yken, H., François, J. M., & Zerbib, D. (2016). Knr4: a disordered hub protein at the heart of fungal cell wall signalling. *Cellular Microbiology*, *18*(9), 1217–1227. https://doi.org/10.1111/cmi.12618

Mastel, S., Govyadinov, A. A., de Oliveira, T. V. A. G., Amenabar, I., & Hillenbrand, R. (2015). Nanoscale-resolved chemical identification of thin organic films using infrared near-field spectroscopy and standard Fourier transform infrared references. *Applied Physics Letters*, *106*(2), 1–6. https://doi.org/10.1063/1.4905507

Mehranian, M., Pourabad, R. F., Bashir, N. S., & Taieban, S. (2017). Physicochemical characterization of chitin from the Mediterranean flour moth, Ephestia kuehniella Zeller

(Lepidoptera: Pyralidae). *Journal of Macromolecular Science, Part A: Pure and Applied Chemistry*, *54*(10), 720–726. https://doi.org/10.1080/10601325.2017.1332461

Michell, A. J., & Scurfield, G. (1970). An Assessment of Infrared Spectra as Indicators of Fungal Cell Wall Composition. *Australian Journal of Biological Sciences*, *23*(2), 345. https://doi.org/10.1071/BI9700345

Mie, G. (1908). Beiträge zur Optik trüber Medien, speziell kolloidaler Metallösungen. *Annalen Der Physik*, *330*(3), 377–445. https://doi.org/10.1002/andp.19083300302

Mohlenhoff, B., Romeo, M., Diem, M., & Wood, B. R. (2005). Mie-type scattering and non-Beer-Lambert absorption behavior of human cells in infrared microspectroscopy. *Biophysical Journal*, *88*(5), 3635–3640. https://doi.org/10.1529/biophysj.104.057950

Nečas, D., & Klapetek, P. (2012). Gwyddion: An open-source software for SPM data analysis. *Central European Journal of Physics*, *10*(1), 181–188. https://doi.org/10.2478/s11534-011-0096-2

Nett, J. E., Sanchez, H., Cain, M. T., Ross, K. M., & Andes, D. R. (2011). Interface of Candida albicans Biofilm Matrix-Associated Drug Resistance and Cell Wall Integrity Regulation. *Eukaryotic Cell*, *10*(12), 1660–1669. https://doi.org/10.1128/EC.05126-11

Nguyen, T. H., Fleet, G. H., & Rogers, P. L. (1998). Composition of the cell walls of several yeast species. *Applied Microbiology and Biotechnology*, *50*(2), 206–212. https://doi.org/10.1007/s002530051278

Orlean, P. (2012). Architecture and biosynthesis of the Saccharomyces cerevisiae cell wall. *Genetics*, *192*(3), 775–818. https://doi.org/10.1534/genetics.112.144485

Roemer, T., & Bussey, H. (1991). Yeast beta-glucan synthesis: KRE6 encodes a predicted type II membrane protein required for glucan synthesis in vivo and for glucan synthase activity in

vitro. *Proceedings of the National Academy of Sciences*, *88*(24), 11295–11299. https://doi.org/10.1073/pnas.88.24.11295

Roemer, T., Delaney, S., & Bussey, H. (1993). SKN1 and KRE6 define a pair of functional homologs encoding putative membrane proteins involved in beta-glucan synthesis. *Molecular and Cellular Biology*, *13*(7), 4039–4048. https://doi.org/10.1128/mcb.13.7.4039

Šandula, J., Kogan, G., Kačuráková, M., & MacHová, E. (1999). Microbial (1→3)-β-D-glucans, their preparation, physico-chemical characterization and immunomodulatory activity. *Carbohydrate Polymers*, *38*(3), 247–253. https://doi.org/10.1016/S0144-8617(98)00099-X

Saulou, C., Jamme, F., Maranges, C., Fourquaux, I., Despax, B., Raynaud, P., Dumas, P., & Mercier-Bonin, M. (2010). Synchrotron FTIR microspectroscopy of the yeast Saccharomyces cerevisiae after exposure to plasma-deposited nanosilver-containing coating. *Analytical and Bioanalytical Chemistry*, *396*(4), 1441–1450. https://doi.org/10.1007/s00216-009-3316-5

Stratford, M. (1994). Another brick in the wall? Recent developments concerning the yeast cell envelope. *Yeast*, *10*(13), 1741–1752. https://doi.org/10.1002/yea.320101307

Szeghalmi, A., Kaminskyj, S., & Gough, K. M. (2007). A synchrotron FTIR microspectroscopy investigation of fungal hyphae grown under optimal and stressed conditions. *Analytical and Bioanalytical Chemistry*, *387*(5), 1779–1789. https://doi.org/10.1007/s00216-006-0850-2

Uchiyama, H., Iwai, A., Dohra, H., Ohnishi, T., Kato, T., & Park, E. Y. (2018). The effects of gene disruption of Kre6-like proteins on the phenotype of β-glucan-producing Aureobasidium pullulans. *Applied Microbiology and Biotechnology*, *102*(10), 4467–4475. https://doi.org/10.1007/s00253-018-8947-z

Zechner-Krpan, V., Petravić-Tominac, V., Gospodarić, I., Sajli, L., Daković, S., & Filipović-Grčić, J. (2010). Characterization of β-glucans isolated from brewer's yeast and dried by different methods. *Food Technology and Biotechnology*, *48*(2), 189–197.

Chapter 7. Summary and future work

In this last chapter of the thesis, Chapter 7, a summary of the critical conclusions of the thesis and ideas for potential future FTIR spectroscopy studies on collagen and fungi-related samples are provided. In this thesis, different FTIR spectroscopic techniques (from macro to nano scale), including far-field FTIR with FPA, far-field FTIR with ATR, far-field O-PTIR and near-field FTIR, were developed and applied to characterize complex biological targets (fungi cell wall and collagen fibrils/tendons), which have different vital roles in their natural state. Each target presented vastly different challenges a along with inherent limitations associated with the techniques used for their analysis. Fungi: the individual cell diameter is about 1-4 μm whereas the layered cell wall thickness is about 100 nm. The components of the cell wall are difficult to characterize and separate from the whole cell due to their small diameters; Collagen: its hierarchical and oriented nature demands investigating them at various length scales, from the complete tendon tissue to the fibril and sub fibril level.

The techniques employed in our investigations are subject to certain known limitations. Other limitations were discovered during the course of this research. The far-field FTIR with FPA method is wavelength dependent, so the spatial resolution for CH stretch modes around 2900 cm^{-1} is about 3.5 μm while spatial resolution in the carbohydrate region around 1050 cm^{-1} is only about 9.5 μm. Given this spatial resolution, the far-field FTIR with FPA primarily probes the entire cell body and is not specifically focused on the cell wall. In the ATR approach, employing a live focal plane array (FPA) aids in visualizing contact instances, yet the inability to entirely regulate contact pressure may result in cell breakage and subsequent leakage of cellular content. The nano-FTIR technique is not exempt from limitations. It is important to note that the force applied during tapping was insufficient to rupture the cell wall. The persistence of a heterogeneous cell wall,

composed of various components, restricts our ability to observe changes in relative band intensities rather than facilitating quantitative analysis. To achieve a broader and more detailed perspective, complementary methods, such as conventional fluorescence staining of cells or by extraction and isolation of components for chemical analysis, as practiced by our collaborators, become indispensable. These techniques either involve the destruction of cells to extract and quantify materials, thus all spatial information is lost, or incorporate staining procedures that could unintentionally alter the cellular structure.

It was essential to develop several vibrational spectroscopic techniques at different length and biospectroscopic imaging protocols that could be applied to these functionally, physically, chemically distinct targets. By comparing the results obtained from different techniques, we gained improved information about the samples as we scaled down from the macro to the nanoscale. As the near-field IR technique is wavelength independent and provides higher spatial resolution compared to diffraction limited far-field techniques, it is the only technique suitable for IR spectroscopy of samples which are less than 100 nm.

Chapter 3 is one of the two chapters focused on collagen in intact tendon and as isolated fibrils. It consists of a peer-reviewed manuscript published in *Molecules* (2020). In this work, far-field and near-field FTIR techniques were used to exploit how polarized IR light affects the spectra of intact tendons and fibrils. IR light polarized perpendicular to the fibril enhances the carbonyl stretch modes such as the Amide I band, while light polarized parallel to the fibril enhances backbone vibrational modes such as amide II and III. Some of these tendons had been examined earlier, and the first near-field FTIR of a single intact fibril was shown (Wiens et al., 2016), this *Molecules* paper presented the first application of polarized O-PTIR to both intact tendon and fibrils enabling a full comparison of methods from macro to nano. In this chapter, *hypotheses 3-1*,

hypotheses 3-2, *hypotheses 3-3,* as stated in Chapter 1.2, were addressed. Far-field FTIR with FPA and O-PTIR data from intact tendons were comparable; both showed the same orientational changes under polarized IR light. O-PTIR spectra with perpendicular orientation from intact fibrils of about 500 nm were a perfect match to nano-FTIR spectra from <100 nm diameter fibrils. However, only the FF O-PTIR could deliver spectra of isolated nano scale fibrils with polarization parallel to the fibril orientation. Only the nano-FTIR could deliver spectra from fibrils less than 100 nm in diameter. The results obtained in Chapter 3 for the intact tendons provided the basis for the investigation reported on the next chapter, in which the different IR methods were applied to the study of damaged tendons. Additionally, this chapter provided a good overview of which techniques would be most suitable for the samples studied in Chapter 4.

Chapter 4 is the second chapter reporting on collagen fibrils; the results will be submitted to the peer-reviewed journal, Analyst. In this study, nano-FTIR spectroscopy was used to understand the relationship between structural, mechanical, and chemical properties of mechanically over-loaded collagen fibrils extracted from SDF (load-bearing) and CDE (positional) bovine forelimb tendons. To the best of our knowledge, this was the first study to report on such fibrils using nano-FTIR. I tested *hypotheses 4-1* and *hypotheses 4-2* stated in Chapter 1.2: The results showed the differences between positional and energy-storing tendons, when they are mechanically damaged, at the molecular level and confirmed the first hypothesis successfully. The heterogeneous nature of the positional tendons may allow them to undergo significant structural changes at the molecular level upon mechanical stress, making them more responsive to remodeling and repair. In contrast, load-bearing tendons may stiffen to bear more stress, leading to clean ruptures. The anticipated changes in nano-FTIR spectra for each type of fibrils were observed, as stated in *hypothesis 4-2* (Chapter 1.2). Those observed changes included differences

in band shapes (narrower Amide I and stronger low energy shoulder in the spectra from overloaded fibrils), shifting in Amide I band maxima when they are ruptured, increased backbone mode intensities in spectra from overloaded fibrils compared to control ones. The results together imply that that mechanical overload can result in changes in the structure and orientation of collagen fibrils in tendons, which may have effects on tendon damage and recovery. The combination of nano-FTIR spectroscopy with AFM is a potent technique for investigating these changes at the nanoscale. Analyzing normal performance and remodelling processes in tendons under mechanical overload/rupture, as well as the development of bioengineered materials, depends on the link between structural and mechanical characteristics.

After showing that IR spectroscopic imaging techniques are powerful tools to characterize structural differences between intact and damaged tendons at the molecular level in Chapters 3 and 4, the versatility of IR spectroscopy was used to investigate another biological sample, the fungal cell wall in Chapter 5 and Chapter 6. Chapter 5 is a peer-reviewed paper published in *Analyst*, in which the *Aspergillus nidulans* cell wall was characterized using nano-FTIR spectroscopy (SINS). In this chapter, *hypotheses 5-1*, *hypotheses 5-2 and hypotheses 5-3* were addressed as stated in Chapter 1.2. The purpose of the study was to investigate the role of galactofuranose (Gal*f*) in cell wall integrity (CWI). I showed that the absence of Gal*f* changes not only the structure of the cell wall components, but also their biochemical composition. The cell's CWI response likely involved compensatory upregulation and cell wall remodelling in Gal*f* deficient strains. According to AFM and TEM analysis, the architecture, composition, function, and integrity of the cell wall were drastically changed in these strains when Gal*f* was absent. The SINS spectra showed increases in the α-glucan wall content in the *ugmAΔ* and *ugtAΔ* gene deletion strains.

Proceeding with the aim of comprehending CWI responses due to mutations, spectral data were acquired with different FTIR techniques from mutant yeast cell strains of *Saccharomyces cerevisiae* (Chapter 6). This is the first study to provide direct spectrochemical information from yeast cell walls obtained with nano-FTIR spectroscopy. I used three scaled approaches, FFIR-FTIR in transmission mode, FFIR-FTIR+ATR and nano-FTIR, to demonstrate the ability of nano-FTIR on cell wall. With these methods working at different length scale, *hypotheses 6-1*, *hypotheses 6-2 and hypotheses 6-3* were tested as stated in Chapter 1.2. Compared to FFIR-FTIR in transmission mode that gives information of whole cell, FFIR-FTIR+ATR spectrochemical imaging offered a superior insight into the cell wall composition by probing cells to a depth of around 1 μm. The wavelength-dependent spatial resolution in both FF approaches prevented further investigation despite the high quality of the spectra. However, the 25 nm nano-FTIR voxel enabled a direct IR spectrochemical probe of cell wall (~100nm thick). According to the analysis of nano-FTIR spectra, yeast cell walls underwent remodelling and altered their compositions in the absence of cell wall proteins Knr4 and Kre6. Our findings revealed that the β-1,6-glucan content of the *kre6Δ* cell wall decreased, while the chitin content increased in the *knr4Δ* cell wall. The significance of nano-FTIR spectroscopy was highlighted in the findings of both Chapter 5 and Chapter 6. These chapters demonstrated its potential for exclusively probing the compositions of cell walls on a nanoscale level. Through this method, direct chemical information from the fungal cell walls was successfully obtained without the need for additional prerequisites that other methods demand. Unlike approaches involving cell fluorescence staining or cell wall extraction and isolation, this technique proved non-destructive and efficient.

By comparing the IR methods presented in Chapters 3, 4, 5 and 6, nano-FTIR showed the best results for both collagen fibrils (<100nm diameter) and fungi cell walls, thus, this technique

is the most appropriate for other biological samples whose dimensions of interest are less than 500 nm.

7.1 New directions for research

Further projects involving collagen fibrils are already underway in the Gough lab. We collaborate with Dr. Laurent Bozec (University of Toronto), who provides collagen scaffolds synthesized in his lab (Abou Neel et al., 2013) to test our joint hypotheses that (a) *glycation alters intra-fibrillar collagen assembly and* (b) *promotes interfibrillar registration in controlled synthetic in-vitro scaffolds*. These hypotheses can be confirmed if we can detect new bands and/or changes in band positions and intensities in nano-FTIR spectra. Part (a) of the hypotheses have already been confirmed and presented in a recent study with our collaborators in which the first Far-field FTIR data from sheets of self-assembled fibers prepared in vitro were reported along with other results (AFM, ELISA, FLIM) from the Bozec lab (Vaez et al., 2022). This study demonstrated how we might utilise a rapid-reacting reduced sugar to change both collagen scaffolds and fibrils, providing distinct biophysical and biochemical features. For the second part of this research with near-field IR spectroscopy, individual collagen fibrils will be teased apart from such sheets in the same manner as fibrils from the intact tendon (Bakir et al., 2020; Wiens et al., 2016). Another intriguing route of investigation would be to investigate mechanically damaged fibrils that undergo different levels of mechanical stress. Many replicates with additional overloads could be examined with nano-FTIR and O-PTIR, which can provide polarized IR data in both perpendicular and parallel orientations (Bakir et al., 2020). Acquiring IR spectrochemical information on different types of positional and load-bearing tendons from various sources could also be another perspective and direction for future investigation. It is important to acquire

knowledge on the collagen tendon types that could respond differently to mechanical stress to determine the degree of the structural disruption and to understand structure-function relationships in collagenous tissues. Collectively, these studies contribute to the development of novel bioengineered materials and provide a solid basis for further investigations on injured tendons. Nano-FTIR spectroscopy is a powerful technique that enables the analysis of collagen fibrils at the nanoscale, providing information into their structural properties. This method allows researchers to study collagen-related real-world issues, such as tissue engineering, wound healing, and diseases like osteoporosis. For instance, it may aid in investigating cardiac fibrosis through the study of collagen in heart tissue and bone health research by examining the effect of mineralization on collagen. In cartilage, it may be used to detect molecular changes linked to degeneration and help in tissue-engineered cartilage evaluation. By investigating the molecular characteristics of collagen fibrils, nano-FTIR spectroscopy contributes to advances in medicine, biomaterials, and tissue engineering, potentially leading to more effective diagnostics and therapies for various health conditions.

The studies of the fungi cell wall (Chapter 5 and Chapter 6) can be extended to include different types of fungi to characterize their cell wall and investigate the CWI responses to different mutations. The methods which have been developed and applied in this thesis can be successfully employed for future analysis of fungi. With near-field IR method, previously inaccessible regions of single cells can now be studied for the production of highly resolved structural and compositional analyses of biological specimens. These studies may also lead to the development of safer antifungal materials, as the cell walls and pathways have for a long time been the prime targets. Nano-FTIR spectroscopy offers practical applications in addressing real-world challenges. For instance, this technique plays a significant role in antifungal drug development by enabling

the identification of key cell wall components, thus facilitating the design of targeted treatments for fungal infections. In biotechnology, it can be used to improve processes related to enzyme production and biofuel generation through the investigation of fungal cell wall dynamics during biotechnological contexts. Nano-FTIR may be used to investigate the role of fungal cell walls in symbiotic or pathogenic relationships with plants, enhancing crop health. This technique may assist in medical mycology by uncovering cell wall changes in pathogenic fungi, thus enabling more effective diagnostic and treatment strategies for fungal infections.

Based on the techniques developed and applied here, it is evident that IR microspectroscopy continues to be a versatile tool that can be applied to the analysis of a wide range of biological samples at varied sizes. This thesis provides methods development and practical applications for future work in this field; it expands our knowledge about the versatility and key role that vibrational spectroscopy plays in the analysis of diverse biological materials.

7.2 References

Abou Neel, E. A., Bozec, L., Knowles, J. C., Syed, O., Mudera, V., Day, R., & Hyun, J. K. (2013). Collagen — Emerging collagen based therapies hit the patient. *Advanced Drug Delivery Reviews*, *65*(4), 429–456. https://doi.org/10.1016/j.addr.2012.08.010

Bakir, G., Girouard, B. E., Wiens, R., Mastel, S., Dillon, E., Kansiz, M., & Gough, K. M. (2020). Orientation Matters: Polarization Dependent IR Spectroscopy of Collagen from Intact Tendon Down to the Single Fibril Level. *Molecules*, *25*(18), 4295. https://doi.org/10.3390/molecules25184295

Vaez, M., Asgari, M., Hirvonen, L., Bakir, G., Khattignavong, E., Ezzo, M., Aguayo, S., Schuh, C. M., Gough, K., & Bozec, L. (2022). Modulation of the biophysical and biochemical

properties of collagen by glycation for tissue engineering applications. *Acta Biomaterialia*. https://doi.org/10.1016/j.actbio.2022.11.033

Wiens, R., Findlay, C. R., Baldwin, S. G., Kreplak, L., Lee, J. M., Veres, S. P., & Gough, K. M. (2016). High spatial resolution (1.1 μm and 20 nm) FTIR polarization contrast imaging reveals pre-rupture disorder in damaged tendon. *Faraday Discussions*, *187*, 555–573. https://doi.org/10.1039/c5fd00168d